

**Numerical Investigation of Spatial
Inhomogeneities in Gravity and Quantum Field
Theory**

by

Alexandre Vincart-Emard

B. Sc., Université de Montréal, 2011

M. Sc., University of Waterloo, 2012

A THESIS SUBMITTED IN PARTIAL FULFILLMENT
OF THE REQUIREMENTS FOR THE DEGREE OF

Doctor of Philosophy

in

THE FACULTY OF GRADUATE AND POSTDOCTORAL
STUDIES

(Physics)

The University of British Columbia
(Vancouver)

August 2017

© Alexandre Vincart-Emard, 2017

Abstract

Many interesting phenomena, such as high-temperature superconductivity and the quark-gluon plasma, still lack a satisfyingly predictive theoretical description. However, recent advances have revealed a curious connection between quantum field theories at strong coupling and classical gravity. This correspondence, known as the gauge/gravity duality or holographic correspondence, offers a promising perspective for investigating strongly correlated systems. In this thesis, we focus on using these new tools to examine the consequences of breaking translational invariance in such systems.

We first use this duality to study the holographic realization of a spatially inhomogeneous condensed matter device known as a Josephson junction. We do so by constructing the gravitational equivalent of two superconductors separated by a weak metallic link, from which we then extract various field-theoretic quantities of interest. These include the spontaneously generated Josephson current, the superconducting order parameter, as well as a novel quantity we refer to as edge currents, which are indicative of gapless chiral modes localized at the interfaces between phases.

We then investigate the more abstract construct of entanglement entropy in holographic theories. We model the fast local injection of energy in a 2+1 dimensional field theory and study the resulting thermalization of quantum entanglement. We achieve this objective by numerically evolving the geometry dual to a local quench from which we then compute the area of various minimal surfaces, the holographic proxy for entanglement entropy. We observe the appearance of a lightcone featuring two distinct regimes of entanglement propagation and provide a phenomenological explanation of the underlying mechanisms at play.

Finally, we turn our attention to spatial inhomogeneities in gravitational systems themselves. We use an approximation of general relativity in which the number of spacetime dimensions is infinite to investigate the Gregory-Laflamme instability of higher-dimensional charged black branes. We argue that charged branes are always unstable in this new language, and push the approximation to next-to-leading order to compute the critical dimension below which the instability results in horizon fragmentation. We also examine the stability properties of two-dimensional black membranes and find that the triangular lattice minimizes brane enthalpy.

Lay Summary

Black holes are mysterious gravitational objects that have long captivated the collective imaginary. The rules that govern them, however, are highly reminiscent of the mathematics describing the quantum dynamics of strongly-correlated electrons. This curious connection, dubbed the gauge/gravity duality, has allowed us to study unconventional materials such as high-temperature superconductors through a new lens with the hope of overcoming the stagnation currently impeding on theoretical progress.

In this thesis we use the gauge/gravity duality to study spatially inhomogeneous systems using the language of black holes. We examine the transport properties of arrays of superconductors and investigate the dynamics of entanglement propagation after a system is locally injected with energy. We also explore the spatial instabilities experienced by higher-dimensional black holes in a new framework where the number of spacetime dimensions is infinite. Our goal: understanding black holes better to harness their predictive power more effectively.

Preface

A version of chapter 2 has been published. Moshe Rozali & Alexandre Vincart-Emard, *Chiral edge currents in a holographic Josephson junction*, A. J. High Energ. Phys. (2014) 2014: 3. My responsibilities were to establish the notation used in the manuscript, to numerically investigate the model, and to communicate the technical results of sections 3 and 4 with the help of accompanying figures. Moshe Rozali fleshed out the physical interpretation of these results and contextualized them by writing the introduction and conclusion.

A version of chapter 3 has been published. Mukund Rangamani, Moshe Rozali & Alexandre Vincart-Emard, *Dynamics of holographic entanglement entropy following a local quench*, A. J. High Energ. Phys. (2016) 2016: 69. My main contributions were to conduct and summarize the numerical implementation of the local quench as described in sections 2 and 3, and to lead the exploration of the model that resulted in section 4, which was drafted by all three authors. I also wrote the material found in the appendices to outline the least obvious details of the implementation. Moshe Rozali provided efficient code for the computation of extremal surfaces as well as analytical and technical guidance throughout. Our collaborator Mukund Rangamani was responsible for providing context to our results by writing the introduction and conclusion.

A version of chapter 4 is currently undergoing peer-reviewing. I was responsible for the numerical exploration and optimization of the new model under consideration, and wrote sections 2 and 3 as well as the appendix, which has been merged with the one from chapter 2 in this thesis for conciseness. Moshe Rozali helped draft the results of section 3 and provided the manuscript's introduction.

A version of chapter 5 has been published. Moshe Rozali & Alexandre Vincart-Emard, *On brane instabilities in the large D limit*, A. J. High Energ. Phys. (2016) 2016: 166. I was in charge of overseeing all of the analytical and numerical implementation details of this article, guided by Moshe Rozali. I also drafted about 95% of the manuscript, whereas Moshe Rozali added final touches to improve the quality of the publication further.

Table of Contents

Abstract	ii
Lay Summary	iii
Preface	iv
Table of Contents	v
List of Figures	viii
Acknowledgements	x
1 Introduction	1
1.1 Motivation	1
1.2 Introducing the Gauge/Gravity Duality	5
1.2.1 Statement of the Duality	6
1.2.2 Holographic Dictionary	12
1.3 Literature Review	21
1.3.1 Holographic Superconductors	21
1.3.2 Entanglement Entropy	28
1.3.3 Large D Limit of General Relativity	35
1.3.4 Numerical Methods	41
2 Chiral Edge Currents in a Holographic Josephson Junction 54	
2.1 Introduction and Summary	54
2.2 Setup and Solutions	56
2.3 Chiral Edge Currents	60
2.4 Josephson Currents	63
2.5 Conclusions	67
3 Dynamics of Holographic Entanglement Entropy Following a Local Quench	68
3.1 Introduction	68
3.2 Preliminaries: Holographic Local Quench	73
3.2.1 Metric Ansatz	73
3.2.2 Asymptotic Geometry	74
3.2.3 Boundary Stress Tensor	76

3.2.4	Holographic Entanglement Entropy	77
3.3	The Quench Spacetime and Extremal Surfaces	78
3.3.1	Numerical Solutions	78
3.3.2	Extremal Surfaces	81
3.4	Propagation of Entanglement Entropy	83
3.4.1	An Emergent Light-cone	84
3.4.2	Entanglement Decay	90
3.5	Conclusions and Future Directions	91
4	Comments on Entanglement Propagation	93
4.1	Introduction	93
4.2	Holographic Local Quenches	95
4.2.1	Setup for Charged Quenches	95
4.2.2	Asymptotic Analysis	97
4.2.3	Integration Strategy	98
4.2.4	Holographic Entanglement Entropy	99
4.3	Results	100
4.3.1	Emergent Lightcone and Entanglement Velocity	101
4.3.2	Entanglement Maximum	105
4.3.3	Entanglement Decay	105
4.4	Summary	109
5	On Brane Instabilities in the Large D Limit	111
5.1	Introduction	111
5.2	Charged p -brane Solutions	113
5.2.1	Uniformly Charged p -Branes	113
5.2.2	Characteristic Formulation for a Charged Black String	114
5.2.3	Solutions and Effective Brane Equations at Leading Order	116
5.3	Phase Structure of the NUBS	117
5.3.1	Solutions and Effective Brane Equations at Subleading Order	118
5.3.2	Charged Black String Phase Diagram	121
5.3.3	Pinch-Off?	123
5.4	Two Dimensional Non-Uniform Phases	125
5.5	Conclusion	128
6	Conclusion	130
6.1	Summary and Future Directions	130
6.1.1	AdS/CMT	130

6.1.2	Holographic Entanglement Entropy	132
6.1.3	Large D Limit of General Relativity	134
6.2	Concluding Remarks	136
Bibliography		137
A	Apparent Horizons	151
B	Numerical Implementation of Characteristic Formulation .	153
C	Dimensional Reduction	156

List of Figures

Figure 1.1	Double-line propagator for $U(N)$ matrix gauge theories. . .	7
Figure 1.2	Illustration of power-counting for planar and non-planar diagrams.	8
Figure 1.3	Stack of N coincident D3-branes.	9
Figure 1.4	Diagram illustrating the commutativity of limits assumption in the initial derivation of the AdS/CFT correspondence.	11
Figure 1.5	The defining hyperboloid of AdS_{d+1}	14
Figure 1.6	Comparison between global AdS and the Poincaré patch.	14
Figure 1.7	The UV/IR relation, illustrated via geodesics and minimal surfaces.	17
Figure 1.8	Second-order phase transition of an holographic s -wave superconductor.	24
Figure 1.9	Conductivity of holographic superconductors as a function of frequency.	26
Figure 1.10	Depiction of a light-sheet.	31
Figure 1.11	Illustration of the entanglement-carrying wavefront observed in global quenches.	33
Figure 1.12	Free-streaming model in two dimensions.	35
Figure 1.13	Geometric construction of the Chebyshev grid.	43
Figure 1.14	Illustration of spectral accuracy for numerical differentiation.	44
Figure 1.15	Caustic formation and trapped surfaces in the bulk.	49
Figure 2.1	The gauge field $M_y^3(r, x)$ and its associated boundary current $J_y(x)$	61
Figure 2.2	Edge current as a function of the junction's depth.	62
Figure 2.3	Edge current as a function of the superconducting order parameter.	63
Figure 2.4	Temperature dependence of the edge current.	63
Figure 2.5	Josephson current.	64
Figure 2.6	Exponential decay of the Josephson current and of the order parameter as a function of the junction's width.	65
Figure 2.7	Temperature dependence of the coherence length.	66
Figure 3.1	Evolution profiles for the radial shift and the energy density.	80

Figure 3.2	Evolution of the total energy after a quench.	80
Figure 3.3	Growth of the apparent horizon following a quench, in boundary time.	82
Figure 3.4	Evolution of the geodesics' radial depth following a quench.	83
Figure 3.5	Dependence of the entanglement entropy's maximum on the entangling surface's width for different scalar amplitudes.	86
Figure 3.6	Dependence of the entanglement entropy's maximum on the entangling surface's width for different initial temperatures.	87
Figure 3.7	Lightcone at high temperature.	88
Figure 3.8	Lightcones and lightcone velocities for three different initial states parametrized by initial temperature.	89
Figure 3.9	Lightcones and lightcone velocities for larger scalar amplitudes.	90
Figure 3.10	Exponential decay of the entanglement entropy at late times.	91
Figure 4.1	Lightcone for all charged configurations.	104
Figure 4.2	Maximum of holographic entanglement entropy as a function of strip width.	106
Figure 4.3	Logarithmic decay of holographic entanglement entropy at late times.	107
Figure 4.4	Logarithmic decay of holographic entanglement entropy at late times for various strip widths.	108
Figure 4.5	Transition in the scaling behaviour of the logarithmic decay.	109
Figure 5.1	Entropy differences per unit length as a function of charge density.	123
Figure 5.2	Phase diagram for the black string instability.	124
Figure 5.3	Change of coordinates for an oblique lattice.	126
Figure 5.4	Black string enthalpy for different oblique lattice angles. .	128

Acknowledgements

First and foremost I would like to thank my supervisor Moshe Rozali, for without his continual guidance the projects presented in this dissertation would never have seen the light of day. I will be eternally grateful for his patience and optimism, and for always taking the time to discuss with me whenever I would show up at his door unannounced with endless questions. My experience in grad school was exempt of the crippling pressure too often felt by doctoral students thanks to his mentorship style, which had a profound impact on my capacity to learn and grow over the past five years.

I gratefully acknowledge the contributions of Mukund Rangamani, who helped shape up our collaboration with his deep insights and his phenomenal talent with words. My gratitude extends to the members of my supervisory committee — Gordon Semenoff, Joanna Karczmarek and Marcel Franz — for their helpful assistance throughout this process.

A heartfelt thank you is also in order for Daniel, who has witnessed the joys and frustrations of research firsthand despite not understanding a word I said. You have my enduring gratitude for always inspiring me to reach higher and do better. Thanks for sharing all of the important milestones of the past few years with me, and for all the wonderful times that made this journey memorable.

Last but not least, I am forever indebted to my parents for always believing in me and giving me the tools I needed to succeed. Venturing into the unknown always felt safer knowing I had their unwavering trust and support, and I am proud to share this accomplishment with them.

Chapter 1

Introduction

1.1 Motivation

Quantum field theory (QFT) is the perfect union between special relativity and quantum mechanics. Originating in the 1920s in an attempt to quantize the electromagnetic field, the resulting theory – quantum electrodynamics (QED) – quickly became the most accurate predictive framework that theoretical physics had ever produced. Besides its high-precision predictions (today’s best theoretical and experimental values for the fine structure constant agree to eight significant figures, an unprecedented achievement in all of science), QED also initiated a paradigm shift in our understanding of fundamental physics by introducing and formalizing important notions like that of particles/antiparticles, renormalizability and symmetry breaking, to name only a few. Work in condensed matter, particle and statistical physics all highly benefited from leveraging quantum field theory’s computational power, which helped establish it as the definite language of nature.

Quantum field theories are generally formulated in terms of their underlying symmetries. A particular type of symmetry, namely gauge symmetry, was found to have a profound impact in the way it dictates and limits the scope of possible physical theories. Unlike physical symmetries like those arising from Noether’s theorem, gauge symmetries do not describe the properties of physical systems. Rather they are indicative of a redundancy in the description of physics; two states related by a gauge transformation are to be understood as the same physical state. The consequence of requiring gauge invariance is a constraint on the form of the interactions between particles. In the case of a $U(1)$ gauge theory like QED, the electron and the photon may only interact in the way prescribed by

$$\mathcal{L}_{\text{QED}} = -\frac{1}{4}F_{\mu\nu}F^{\mu\nu} - \bar{\psi}\left(i\gamma^\mu(\partial_\mu - iA_\mu) - m\right)\psi \quad (1.1)$$

in order for the theory to be invariant under local $U(1)$ rotations $\psi \rightarrow e^{-i\alpha(x)}\psi$.

The new machinery of gauge invariance ultimately led to quantum chro-

modynamics (QCD), a theory of strong interactions used to model composite particles known as hadrons, which include the proton and the neutron. Conceptually QCD is simply a field theory with fermionic fields named quarks taken to be invariant under $SU(3)$ gauge transformations. These fundamental constituents interact via an octet of gauge bosons known as gluons subjected to the quarks' three gauge degrees of freedom (i.e. three types of charges) known as colours. However, QED and QCD are vastly different theories. Whereas QED is a weakly-coupled theory (the fine structure constant is small enough to allow a perturbative expansion of scattering amplitudes), the theory of QCD is one of strong interactions¹ where perturbative methods fail miserably. This property greatly hinders our ability to make predictions with traditional approaches, thus other techniques need to be used to expand our understanding of quantum dynamics in this new regime.

Quantum chromodynamics is not the only theory that suffers from limitations due to strong interactions. In the realm of condensed matter physics, many new metallic materials discovered since the 1980s were found to exhibit thermodynamic and transport properties not described accurately by Fermi liquid theory, which is widely used to model most interacting systems of fermions, including metals, insulators, conventional superconductors and superfluids. All Fermi liquids have two things in common: their ground states are characterized by a Fermi surface, and their low-energy excitations about that Fermi surface behave as weakly interacting quasiparticles and quasiholes of same electric charge and statistics. Non-Fermi liquids (NFL), in contrast, are strange metals made up of electrons so strongly correlated that they cannot propagate long enough to show their particle-like properties. In other words, the decay rate of excitations in a NFL is too large for a quasiparticle interpretation of its dynamics. Novel phases of matter that fall in that category, such as high- T_c cuprate superconductors and fermions near quantum critical points, have so far eluded a satisfactory theoretical description and remain largely misunderstood.

Alternative methods thus need to be developed. In practice Monte Carlo methods are often used to estimate the system's partition function and its derivatives. This is done by discretizing spacetime on a finite lattice, evaluating the (real) Euclidean action via random sampling, and then extrapolating the results to the infinite volume, vanishing lattice spacing limit. Unfortunately this approach has a few limitations. For one the lattice sizes

¹QCD is an asymptotically free theory, meaning that it becomes free at very high energies but remains strongly interacting for energies below $\Lambda_{\text{QCD}} \approx 220$ MeV.

that can be simulated are very small [1]: a $48^3 \times 64$ lattice in QCD corresponds approximately to a $(4 \text{ fm})^3$ volume, which precludes the study of long-wavelength physics. Such simulations also require prohibitively expensive computational resources. Another conceptual issue known as the fermion sign problem arises when considering theories at non-zero fermion density. Such systems are described by a chemical potential that induces a highly-oscillatory behaviour in the partition function (i.e. the Euclidean action becomes complex), which effectively invalidates the use of Monte Carlo methods. In addition, lattice methods are limited in scope since they are only applicable to compute quantities derived from the partition function, therefore prohibiting the study of transport coefficients and far-from-equilibrium dynamics.

In both cases, progress has been largely inhibited by the failure of the field theory framework to be predictive when the fundamental constituents interact strongly with one another. As such different tools need to be developed. In 1974, 't Hooft had an idea: What if we considered an $SU(N)$ gauge theory for some large value of N ? Could it be that an expansion in $1/N$ might yield satisfactory predictions for QCD when evaluated at $N = 3$? He showed that the gauge theory greatly simplified under the assumption $N \rightarrow \infty$, under which the relevant Feynman diagrams are sorted according to their degree of planarity [2]. Despite this simplification an analytical large N field-theoretic solution is still lacking, but progress was made on an entirely different front in 1997 when Maldacena used string theory to formulate the AdS/CFT correspondence [3]. Surprisingly, lingering questions about strongly coupled field theories would instead find their answers within classical general relativity.

Maldacena's conjecture, also known as the gauge/gravity duality, is a statement that relates the physics of conformal field theories (CFT) at large N with the gravitational dynamics of anti-de Sitter (AdS) spacetimes in one more dimension. The field theory is said to exist on the boundary of AdS, and the extra radial dimension which extends in the bulk is understood as its energy scale. Since both theories describe the same physics, they share the same fundamental degrees of freedom despite the field theory living in one fewer dimension. It is then said that the AdS/CFT correspondence is a realization of the holographic principle, which has warranted the use of the qualificative *holographic* in regards to the wealth of results obtained within this framework.

The correspondence's perhaps most important property is that it is a strong/weak duality that provides a computational bridge between the two theories: when the field theory is at strong coupling and calculations are

notoriously difficult, they can instead be carried out in the much friendlier setup of classical gravity. For instance, the computation of expectation values is instead mapped to the more approachable problem of solving the Einstein equations with appropriate boundary conditions, whereas quantities like entanglement entropy are assigned a geometrical interpretation as the area of a minimal surface. Put simply the two theories are two different faces of the same coin, and every physical phenomena on one side has a dual description on the other.

The scope of application of the gauge/gravity duality is also quite vast. Systems at zero temperature correspond to pure AdS spacetimes with no IR cutoff (so as not to introduce a temperature scale), whereas the presence of a black hole horizon in the gravitational bulk encodes the thermodynamics of the boundary theory. Similarly, theories at finite charge density possess gravitational duals in the form of charged black holes. The addition of matter fields in such backgrounds has led to the study of strongly-correlated systems, including but not limited to NFL as a dual description of Dirac fermions in AdS, quantum phase transitions via scalar condensation in the bulk, and holographic QCD.

The gauge/gravity framework has also succeeded in relating fluid flow in the boundary theory to the dynamics of inhomogeneous dynamical black holes in AdS, giving rise to what is now known as the fluid/gravity correspondence [4]. This holographic hydrodynamics point of view has proven particularly useful in shaping our physical intuition about matter interactions given the absence of quasiparticle concept at strong coupling. Moreover, it is possible to go beyond the long-wavelength approximation to study far-from-equilibrium dynamics directly by solving the time-dependent Einstein equations in all their glory. This regime is often inaccessible to current theoretical approaches (as in the case of lattice QCD), thus further adding to the duality's usefulness and predictive potential.

Finally the AdS/CFT correspondence has provided physicists with new tools to address fundamental questions about the nature of spacetime. Issues regarding the black hole information paradox and the properties of entanglement entropy, to name only a few, are readily framed and studied in this new language. The new geometric insights now possible thanks to the duality have stimulated creativity and productivity in these areas more than ever.

All in all, the gauge/gravity duality has been a proficient tool for improving our understanding of field theories in the strong coupling regime. Most of the early results were found for static, spatially homogeneous settings in which only the radial dynamics was relevant. The reason, beyond developing

our intuition with simple toy models, was mainly that the dual gravitational description amounted to solving ordinary differential equations that posed no significant computational challenge. However many interesting things start to happen once we consider spatially inhomogeneous setups and time-dependence. For instance, in quantum mechanics the finite well potential already leads to novel phenomena like scattering and quantum tunnelling. On account of the complexity of interactions in large N gauge theories, it follows that richer situations should arise when studying spatially inhomogeneous systems. On the gravity side, the trade-off is the need to solve systems of coupled non-linear partial differential equations numerically, a daunting task if one is not acquainted with effective techniques to do so.

In this dissertation we undertook a numerical study of spatial inhomogeneities in hopes of discovering the richer dynamics underlying strongly coupled field theories via the tools of the gauge/gravity duality. Our first foray led us to study the properties of chiral holographic Josephson junctions and the various currents that flow spontaneously as a consequence of broken translation invariance. We then took on the ambitious project of generalizing the physics of global quenches – rapid injections of energy in a system – by considering variations of finite spatial extent, as well as the resulting dynamics of holographic entanglement entropy that characterizes this non-equilibrium process. Finally, we veered away from the AdS/CFT framework to study gravity as an object of its own rather than as a proxy tool by investigating the stability properties of higher-dimensional black branes in asymptotically flat space.

We start by motivating the validity of the correspondence in Section 1.2 via a series of mostly qualitative arguments from string theory, the unifying framework from which it initially emerged. The literature review of Section 1.3 then serves to bring the reader up to speed in regards to the many topics present in this thesis. These topics include expositions to the physics of holographic superconductors, to the holographic formulation of entanglement entropy, to an approximation of general relativity where the number of spacetime dimensions is taken to be large, and to the many numerical methods we have used throughout our analysis of these various systems.

1.2 Introducing the Gauge/Gravity Duality

The gauge/gravity duality is a statement about the equivalence between certain classes of quantum fields theories and theories of quantum gravity with an additional spacetime dimension. The first realization of this equivalence

was found in 1997 by Maldacena, who used string theory to argue that

$$\mathcal{N} = 4 \text{ } SU(N) \text{ SYM in 4D} \longleftrightarrow \text{Type IIB SUGRA on AdS}_5 \times S^5.$$

A few comments are now in order before proceeding further. First, despite being initially formulated in four spacetime dimensions, the conjecture has since then been extended to unite d -dimensional QFTs and AdS gravity in $d + 1$ dimensions. Second, supersymmetry, which relates the $\mathcal{N} = 4$ multiplet of super-Yang-Mills to the compact manifold S^5 in the particular example above, is not an essential ingredient of the correspondence and may be relayed to the background without affecting its validity. Although supersymmetry is useful in constraining the scope of possible interactions and by providing various quantitative checks on both sides, in this dissertation we adopt a *bottom-up* approach to the gauge/gravity duality in which we only consider the universal subsector of supergravity, namely the one that determines the dynamics of Einstein gravity with a negative cosmological constant

$$S_{\text{universal}} = \frac{1}{16\pi G_N} \int d^{d+1}x \sqrt{-g} (R - 2\Lambda), \quad (1.2)$$

with possible inclusions of matter fields. Despite being exempt of supersymmetric fields, the action (1.2) is always a consistent supergravity truncation and its solutions may be uplifted to the full string theory if need be. As such we will restrict our attention to the study of this decoupled subsector, whose dynamics are understood to be universal across field theories with gravitational duals. Last, we seek not to prove the conjecture in what follows but merely to motivate and justify its validity so that the reader may feel confident in the predictions made with this novel theoretical approach, while still being aware of its limitations.

1.2.1 Statement of the Duality

In this section we lay out the necessary ingredients to understand the correspondence at a qualitative level via the unifying physics of D-branes. In particular, we clarify what it means for a gauge theory to be strongly coupled and review the conditions under which the stringy and quantum corrections of supergravity are suppressed.

Gauge theories at large N

Consider a Yang-Mills theory with gauge coupling g_{YM} and composed of matrix-valued fields Φ that transform in the adjoint representation of $U(N)$.

$$\langle \Phi_b^a \Phi_d^c \rangle = \delta_d^a \delta_b^c = \begin{array}{c} a \longrightarrow \\ \longleftarrow b \end{array} \begin{array}{c} \longrightarrow d \\ \longleftarrow c \end{array}$$

Figure 1.1: The propagator of a $U(N)$ matrix gauge theory in the double-line notation. Each Kronecker δ represents a flow of colour.

A schematic Lagrangian for this theory would be of the form

$$\mathcal{L} \sim \text{Tr} [(d\Phi)^2 + \Phi^2 + g_{\text{YM}} \Phi^3 + g_{\text{YM}}^2 \Phi^4 + \dots]. \quad (1.3)$$

The fields Φ , which may include scalars, fermions and/or gauge fields, are understood to be $N \times N$ matrices. Under these assumptions, the index structure of the propagator is found to be

$$\langle \Phi_b^a \Phi_d^c \rangle = \delta_d^a \delta_b^c, \quad (1.4)$$

which can be thought of as encoding colour flow between a fundamental-antifundamental pair², as shown in Figure 1.1.

Looking at vacuum-vacuum Feynman diagrams reveals something interesting about matrix-valued gauge theories: double-line graphs can have non-planar topologies [2]. In fact, every graph can be thought of as the triangulation of a two-dimensional surface with genus \mathfrak{g} , which intuitively corresponds to the number of “handles” a surface possesses. It can be shown that the coefficient of a vacuum-vacuum diagram with genus \mathfrak{g} and $2k$ vertices is $N^{2-2\mathfrak{g}} \lambda^k$, where we have introduced the 't Hooft coupling $\lambda \equiv g_{\text{YM}}^2 N$.

In the case where λ is kept fixed but N is taken to be large, diagrams with higher genus become suppressed, leaving only planar graphs at leading order $\mathcal{O}(N^2)$. In fact planarity affects the number of loops present in a diagram, with non-planar diagrams allowing for fewer colour loops, as illustrated in Figure 1.2. This observation suggests that the theory greatly simplifies when taking the *'t Hooft limit* (also called the planar limit)

$$N \rightarrow \infty \text{ and } g_{\text{YM}} \rightarrow 0 \text{ with } \lambda = g_{\text{YM}}^2 N \text{ kept fixed.} \quad (1.5)$$

We remark that the 't Hooft limit is neither classical nor free despite the gauge coupling g_{YM} going to 0; it can be seen that the diagrammatic ex-

²Note that for $SU(N)$ theories, the propagator instead reads $\langle \Phi_b^a \Phi_d^c \rangle = \delta_d^a \delta_b^c - \delta_b^a \delta_d^c / N$ to account for the tracelessness of the matrix fields ($\Phi_a^a = 0$). However in the large N limit the dynamics of $SU(N)$ is equivalent to that of $U(N)$.

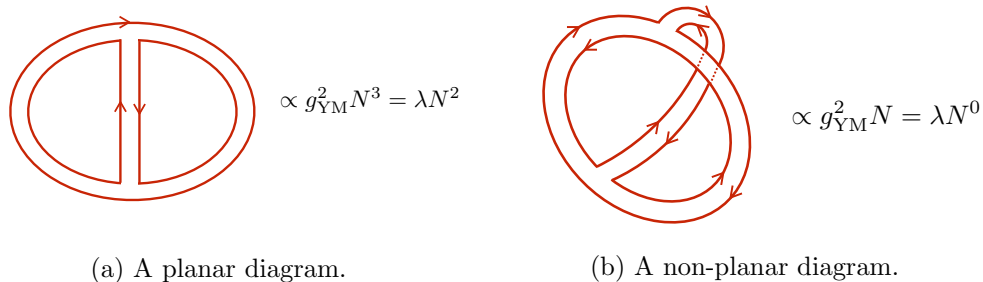


Figure 1.2: An illustration of power-counting for planar and non-planar diagrams. Figure (a) shows a planar diagram made with 2 three-point vertices each contributing g_{YM} , and 3 colour loops each contributing a factor of N . In contrast, figure (b) also has 2 three-point vertices but only 1 colour loop, which affects its power of N only.

pansion for the partition function includes an infinite number of modes. In theory one may use perturbation theory if λ is small enough, but the regime of interest of AdS/CFT is when the coupling is strong, $\lambda \gg 1$, and quantum loop corrections of all orders are included.

The low-energy limit of D-branes

Let us now move on to the topic of Dp-branes, which are topological defects extended in p spatial dimensions in string theory (with string coupling g_s) on which string endpoints can end [5]. D-branes also act as sources for closed strings, which in this context are best thought of as the excitations of the vacuum. In what follows we adopt two different but equivalent points of view regarding the low-energy limit of D-branes, meaning at energies lower than the one naturally set by the string length ℓ_s . For concreteness we consider the case where $p = 3$ on which Maldacena's conjecture was initially based, but note that the analysis can be extended to different brane configurations as well.

We first consider N coincident D3-branes in Type IIB string theory at weak coupling $g_s N \ll 1$. At low energies, where only massless string states can be excited, gravity in the bulk decouples entirely from the dynamics on the branes. This leaves us with massless closed strings, which are identified as the sources for Type IIB supergravity in flat space, as well as with open strings. As shown in Figure 1.3, the latter can end on any of the N coincident D3-branes. It is argued in [6] that the resulting effective action on the

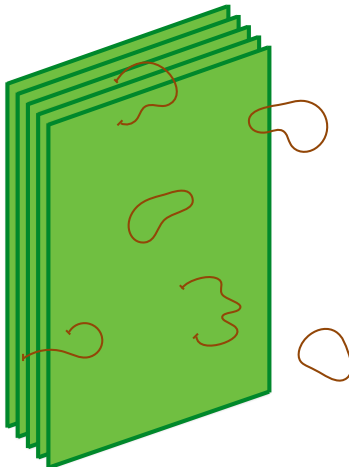


Figure 1.3: The low-energy limit of a theory of N coincident D3-branes is a theory of massless strings. The closed strings are responsible for flat space gravity, whereas the open strings give rise to an $SU(N)$ gauge theory.

branes is that of a ten-dimensional $SU(N)$ (supersymmetric) gauge theory dimensionally reduced to the $p + 1$ worldvolume of the Dp-branes. Equivalence between the couplings on the field theory side and in the D-brane description identify $g_{\text{YM}}^2 = 4\pi g_s$. We therefore conclude that when $g_s N \ll 1$

D3-branes = Free gravity + $\mathcal{N} = 4$ $SU(N)$ SYM in 3+1 dimensions.

On the other hand, we can also think of Dp-branes as black p -brane solutions of classical supergravity when the coupling is strong $g_s N \gg 1$ [7]. The geometry of the D3-branes is given by the metric

$$ds^2 = \frac{\eta_{\mu\nu} dx^\mu dx^\nu}{f(r)^{1/2}} + f(r)^{1/2} (dr^2 + r^2 d\Omega_5^2), \quad f(r) = 1 + \frac{4\pi g_s N \ell_s^4}{r^4}, \quad (1.6)$$

where x^μ denotes the 4 coordinates along the worldvolume of the branes and $d\Omega_5^2$ is the metric of a unit five-dimensional sphere S^5 . For this solution to be valid, a self-dual 5-form $F_5 = (1 + *) dt dx_1 dx_2 dx_3 df$ with flux on the S^5

$$\int_{S^5} *F_5 = N \quad (1.7)$$

is required. Again there are two types of low-energy excitations that decouple from each other. The first corresponds to long-wavelength excitations in the bulk, i.e. free gravity in flat space. The second corresponds to finite energy excitations that become increasingly red-shifted (as seen from an observer at infinity) as they approach the horizon $r = 0$. The latter are captured by the near-horizon geometry

$$ds^2 = \frac{r^2}{L^2} \eta_{\mu\nu} dx^\mu dx^\nu + \frac{L^2}{r^2} dr^2 + L^2 d\Omega_5^2, \quad L^4 = 4\pi g_s N \ell_s^4, \quad (1.8)$$

which corresponds to $\text{AdS}_5 \times S^5$, with L acting both as the AdS radius of curvature and the radius of the unit 5-sphere. Thus we conclude that when $g_s N \gg 1$

$$\text{D3-branes} = \text{Free gravity} + \text{Type IIB supergravity on } \text{AdS}_5 \times S^5.$$

We therefore have two descriptions of D-brane physics in two distinct regimes. The low-energy limit of the D3-brane system corresponds to an $SU(N)$ gauge theory when $g_s N \ll 1$, whereas it can be described by supergravity on $\text{AdS}_5 \times S^5$ when $g_s N \gg 1$. However we have seen that the gauge theory description is valid for all values of the 't Hooft coupling. It is not too big of a leap then to think of D-branes as the fundamental object that unifies supergravity and gauge theories, regardless of their defining regime. In other words, the two theories are equivalent representations of the same physics, valid for all values of g_s and N , as illustrated in Figure 1.4. This is embodied in the famous duality

$$\mathcal{N} = 4 \text{ } SU(N) \text{ SYM in 4D} \quad \longleftrightarrow \quad \text{Type IIB supergravity on } \text{AdS}_5 \times S^5$$

which is most useful when $g_s N \gg 1$ on both sides.

We have already reasoned that the gauge theory greatly simplifies when $N \gg \lambda \gg 1$, which also implies $g_{\text{YM}} \rightarrow 0$. On the gravity side, this is equivalent to

$$\frac{L^4}{\ell_s^4} = 4\pi g_s N = \lambda \gg 1, \quad (1.9)$$

which is a statement about stringy corrections to the geometry being suppressed since the string scale ℓ_s is much smaller than the AdS radius L . Similarly, to suppress quantum corrections one needs to look at the ratio L/ℓ_P , where ℓ_P is the Planck length, which can be related to the string length via $\ell_P^4 = g_s \ell_s^4$ in ten-dimensional string theory. We thus obtain the

condition

$$\frac{L^4}{\ell_P^4} = \frac{L^4}{g_s \ell_s^4} = \left(\frac{L^4}{\ell_s^4} \right) \frac{N}{g_s N} \sim N \gg 1, \quad (1.10)$$

which is saying that quantum corrections to the geometry are akin to $1/N$ corrections in gauge theory.

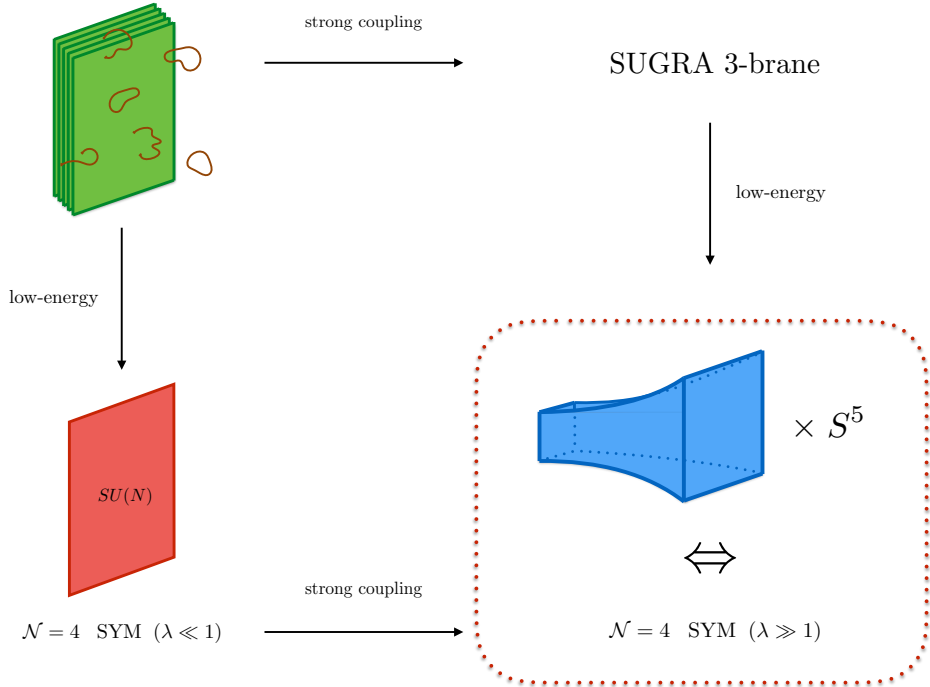


Figure 1.4: This diagram illustrates how the AdS/CFT correspondence was first derived. The starting point is a stack of N coincident D3-branes, in the upper-left corner. The low-energy limit of this fundamental object results in an $SU(N)$ super-Yang-Mills theory at weak coupling, which is assumed valid at any value of the coupling λ . The strong coupling limit of D3-branes instead yields a 3-brane solution of classical supergravity whose near-horizon/low-energy limit yields Type IIB string theory on $AdS_5 \times S^5$. Assuming that the low-energy and strong coupling limits commute, we identify the two theories in the lower-right corner, resulting in the first known example of a field theory with a gravitational dual.

In this section we have argued that $SU(N)$ super-Yang-Mills gauge theories at large N and strong coupling $\lambda \gg 1$ describe the exact same physics as supergravity on $\text{AdS}_5 \times S^5$ provided it is classical, i.e. provided both stringy and quantum corrections are suppressed. It is interesting to note that the duality can be broadened to include spacetimes that are *asymptotically* $\text{AdS}_{p+2} \times \chi^{8-p}$, where χ^{8-p} is an $8-p$ dimensional compact manifold subject to string theoretical constraints. The conjecture still stands even if the bulk contains a black hole, with the only difference being that the dual field theory becomes thermal. Moreover, we mentioned that the choice $p = 3$ in the argument above was for the sake of simplicity; similar analyses for other brane configurations reveal that, when applicable, strongly coupled gauge theories in d dimensions admit a dual gravitational description in $d+1$ dimensions. In other words, the gauge/gravity duality is at its heart a particular realization of the holographic principle, a notion we will define in more detail in the next section.

1.2.2 Holographic Dictionary

We now provide evidence supporting the validity of the AdS/CFT correspondence. By exploring the geometry of AdS, we show that its symmetries are in perfect agreement with those of a CFT. We then explore the idea that the correspondence is in fact a realization of the holographic principle by matching the degrees of freedom on both sides. We finish by formulating the field/operator correspondence to establish a direct relationship between dual quantities. All of these non-trivial checks that form the holographic dictionary give strong foundations to the conjecture.

Anti-de Sitter geometry

Symmetries play an important and central role in our understanding of quantum field theories. They constrain the form of interactions, impose the existence of force carriers as gauge bosons, give us a powerful tool to classify elementary particles, and so on. In fact, if two theories share the same symmetries, then there are good reasons to believe that their underlying mechanisms may well be the same. An early check of the gauge/gravity duality was to identify the symmetries of anti-de Sitter spacetimes with the conformal symmetries of the boundary theory.

Let us start by examining d -dimensional conformal field theories, which are invariant under coordinate transformations that preserve angles. Such

transformations effectively rescale the metric by an arbitrary positive factor

$$g_{\mu\nu}(x) \rightarrow \Omega^2(x)g_{\mu\nu}(x). \quad (1.11)$$

In the particular case of Minkowski space, conformal transformations include translations, Lorentz transformations, dilatations $x^\mu \rightarrow ax^\mu$, and inversions $x^\mu \rightarrow x^\mu/x^2$. It is a straightforward but tedious exercise to extract the conformal symmetry group from the generators of infinitesimal transformations. It can nonetheless be shown that the conformal algebra obeyed by these generators is isomorphic to the algebra of $SO(2, d)$ [8].

As it turns out, the conformal group $SO(2, d)$ is precisely the symmetry group of anti-de Sitter spacetimes, which is easy to verify. The variation of the Einstein-Hilbert action with a negative cosmological constant

$$S = \frac{1}{16\pi G_N} \int d^{d+1}x \sqrt{-g} (R - 2\Lambda), \quad \Lambda = -\frac{d(d-1)}{2L^2} \quad (1.12)$$

yields the Einstein equations for which pure $d+1$ dimensional anti-de Sitter space, AdS_{d+1} , is a solution. The most straightforward way to study the symmetries of this spacetime is by considering its defining hyperboloid with radius L

$$X_0^2 + X_{d+1}^2 - \sum_{i=1}^d X_i^2 = L^2, \quad (1.13)$$

embedded in a flat $d+2$ dimensional geometry with two timelike directions $\mathbb{R}^{2,d}$

$$ds^2 = -dX_0^2 - dX_{d+1}^2 + \sum_{i=1}^d dX_i^2. \quad (1.14)$$

Its symmetries are therefore described by the group $SO(2, d)$ by construction, which is what we sought in the first place. We however note that the hyperboloid contains closed timelike curves that need to be unwrapped for the space to be causal, as illustrated in Figure 1.5. Thus the equivalence applies only when we consider its universal cover, for which $X_0 \in \mathbb{R}$.

There are many coordinate patches that satisfy the defining equation (1.13) (see Figure 1.6). One such solution is known as global AdS, whose metric is given by

$$ds^2 = -\left(1 + \frac{r^2}{L^2}\right) dt^2 + \left(1 + \frac{r^2}{L^2}\right)^{-1} dr^2 + r^2 d\Omega_{d-1}^2 \quad (1.15)$$

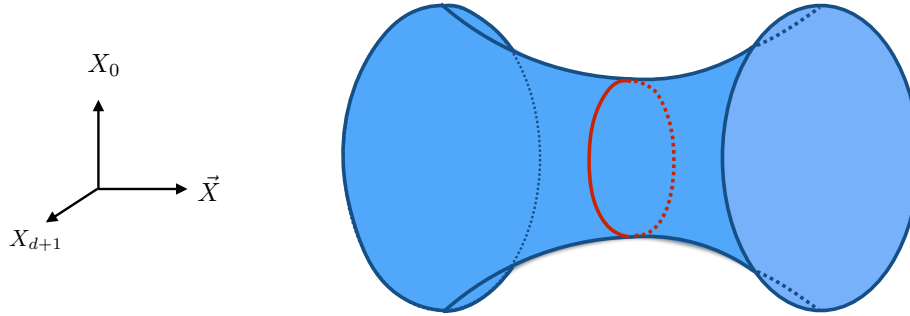


Figure 1.5: The defining hyperboloid of AdS_{d+1} . The red circle illustrates an acausal closed timelike curve.

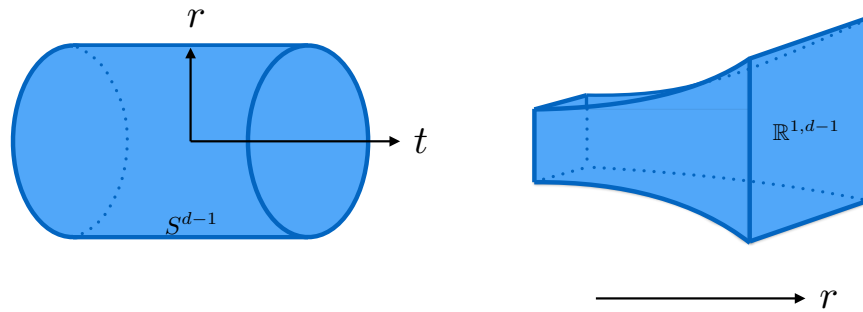


Figure 1.6: On the left is a representation of global AdS, which has a cylindrical boundary topology. On the right is a representation of the Poincaré patch, which can be viewed as a collection of warped Minkowski spacetimes connected along a radial direction.

and whose coordinates cover the entire hyperboloid. Its boundary, located at $r \rightarrow \infty$, is spatially compact and has topology $\mathbb{R} \times S^{d-1}$. Alternatively,

the Poincaré patch

$$ds^2 = \frac{L^2}{r^2} dr^2 + \frac{r^2}{L^2} \eta_{\mu\nu} dx^\mu dx^\nu \quad (1.16)$$

is the set of coordinates $\{(r, t, \vec{x}) \mid r > 0, x \in \mathbb{R}^{1,d-1}\}$ that cover only half of the defining hyperboloid (1.13). In contrast to the global chart, the boundary is simply a warped version of Minkowski spacetime $\mathbb{R}^{1,d-1}$. Both charts are equally valid, and the choice of which one to use depends solely on the topology that we require of the boundary theory. Without loss of generality, throughout this thesis we will focus on the non-compact Poincaré patch (1.16), whose metric makes manifest the decomposition of the isometry group $SO(2, d)$ of AdS into its subgroups $ISO(1, d - 1)$ (Poincaré transformations acting on (t, \vec{x})) and $SO(1, 1)$ (rescaling symmetry). These symmetries underlie many field theories of interest, whereas the compact nature of global AdS is mathematically attractive but feels physically artificial.

The rescaling symmetry of AdS actually provides us with an invaluable insight in how to think of the extra radial dimension from a field theory perspective. Indeed, notice how dilatations $x^\mu \rightarrow ax^\mu$ on the boundary are balanced with the bulk radial coordinate scaling as $r \rightarrow a^{-1}r$ for $a > 0$. Since energy is conjugate to time, a process with energy E on the boundary field theory would necessarily scale as $E \rightarrow a^{-1}E$ under this symmetry, i.e. exactly like the bulk radius r . This equivalence under rescaling tells us that r can be interpreted as an energy scale from the field theory point of view; high-energy/short-distance phenomena is mapped unto gravitational dynamics at large radius r , whereas low-energy/long-wavelength physics is described by the near-horizon ($r = 0$) geometry. We examine this general property of AdS spacetimes further in the next section.

Counting and matching the degrees of freedom

It is a straightforward exercise to show that the degrees of freedom on the field theory side of the duality match with the ones allowed in a theory of quantum gravity. Let us start investigating the latter situation with a simple thought experiment showing that a black hole is the most entropic configuration of space.

Without loss of generality [9], consider the smallest spherical region of spacetime with area A that completely encloses a matter system with mass m right below the threshold M required for it to become a black hole. Also assume that the system has entropy S_m . Let there be a thin shell located

outside the region of interest with total mass $\delta m = M - m$ such that a black hole with area A would form upon collapse. The total initial entropy of the matter system is $S_{\text{initial}} = S_m + S_{\delta m}$, whereas upon collapse the final entropy is that of a black hole, $S_{\text{final}} = A/4G_N$, where G_N is Newton's constant. In order for the second law of thermodynamics to hold, the initial entropy of the matter system cannot exceed that of the associated circumscribed black hole: $S_m + S_{\delta m} \leq A/4G_N$. We thus learn that the *maximal* entropy associated with a region \mathcal{R} of space is proportional to the area of its boundary $\partial\mathcal{R}$

$$S_{\text{max}}(\mathcal{R}) = \frac{\text{Area}(\partial\mathcal{R})}{4G_N}. \quad (1.17)$$

Equation (1.17) is known as the *Bekenstein bound* [10], and it is a fundamental property of gravitational systems in that we have not considered the microscopic properties of matter in deriving it. The Bekenstein bound is at the core of the holographic principle since it states that, counter to intuition, any stable region of spacetime can be described by the degrees of freedom on its boundary rather than the ones in its volume.

We can now make use of (1.17) to compute the degrees of freedom allowed in the $\text{AdS}_5 \times S^5$ geometry. Without loss of generality, let us work in the Poincaré patch

$$ds^2 = L^2 \frac{dz^2 + \eta_{\mu\nu} dx^\mu dx^\nu}{z^2} + L^2 d\Omega_5^2, \quad (1.18)$$

which has a boundary at $z = 0$. The area of this boundary formally diverges, but we can regularize it by introducing an IR cutoff³ at $z = \delta \ll 1$ which acts as a boundary-like surface with a well-defined area. We find

$$S = \frac{1}{4G_N} \int_{z=\delta} d\Omega_5 d^3x \sqrt{-g} \Big|_{t \text{ fixed}} = \frac{\text{Vol}(\mathbb{R}^3) \text{Vol}(S^5) L^8}{4G_N \delta^3} \sim \frac{\text{Vol}(\mathbb{R}^3) N^2}{\delta^3}, \quad (1.19)$$

where we have used the fact that the ten-dimensional Newton constant is related to the Planck length via $G_N = \ell_P^8$, by definition.

In contrast, the degrees of freedom in a general quantum field theory scale like the volume of the region of interest. Let's consider a discretized version of an $SU(N)$ matrix field theory by introducing an UV cutoff δ defining the length of the discretized volume cells. There are approximately $\text{Vol}(\mathbb{R}^3)/\delta^3$ such lattice sites, each with $N(N - 1)$ degrees of freedom that follow from the dimension of the adjoint representation of $SU(N)$. We can

³The new coordinate z is inversely proportional to the radial coordinate r of (1.8): $z = L^2/r$. As such $z = \delta$ corresponds to a large distance regularizer in the bulk.

therefore estimate the total number of degrees of freedom in the volume to be

$$S \sim \frac{\text{Vol}(\mathbb{R}^3)N^2}{\delta^3}, \quad (1.20)$$

in complete agreement with (1.19) up to numerical factors.

This matching of degrees of freedom in the two theories suggests that the gauge theory living on the boundary of AdS_5 is sufficient to describe the gravitational dynamics inside the bulk and vice-versa. The introduction of δ as a cutoff in the derivation above shows that the short-distance (UV) physics of the gauge theory is implemented near the boundary (IR) of AdS_5 , a phenomena known as the *UV/IR relation* [11]. Similarly, we may extend this argument by considering geodesics and minimal surfaces anchored on the boundary of AdS_5 (see Figure 1.7). Geodesics that have endpoints close to each other stay relatively close to the boundary and probe high-energy phenomena from the field theory point of view. Conversely, geodesics with endpoints distanced further apart and thus associated to long-wavelength physics on the boundary necessarily go deeper in the bulk, effectively mapping the UV of the gravity side to the IR of the field theory. In addition to our previous discussion regarding the rescaling symmetry, this mapping serves as an additional argument for interpreting the extra radial dimension as an energy scale.

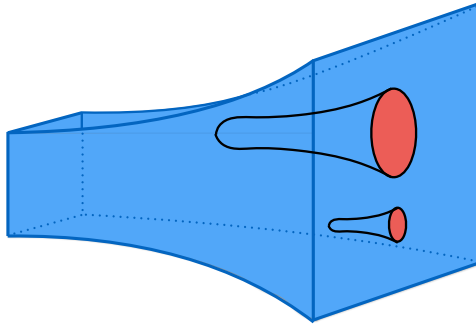


Figure 1.7: The gravitational dynamics deeper in the bulk influence the lengths and areas of geodesics and minimal surfaces with larger spatial support on the boundary. Larger regions are associated with coarse-grained long-wavelength physical phenomena, which leads to the interpretation of the AdS radius r as an energy scale for the dual boundary theory.

Observables and correlation functions

Perhaps the most remarkable aspect of the gauge/gravity duality is the natural prescription it provides for calculating gauge theory correlators. Correlation functions are notoriously difficult to compute without the help of perturbation theory, which fails in the strong coupling regime we are interested in. In the case of conformal field theories, conformal invariance is a valuable asset in determining the natural scaling of n -point functions, but the conformal toolbox also fails when new scales that deform the CFT are introduced. However, we have argued that the physical content of supergravity on asymptotically anti-de Sitter spacetimes can be described entirely by the gauge theory living on its boundary. As such, classical supergravity should — and does — offer an equivalent framework in which to compute gauge theory correlators at strong coupling. The prescription is implemented via

$$\mathcal{Z}_{\text{CFT}}[\phi_0(x)] = \mathcal{Z}_{\text{SUGRA}} \left[\lim_{r \rightarrow \infty} \phi(r, x) \sim \phi_0(x) \right], \quad (1.21)$$

which is a statement about the equivalence of the partition functions, and therefore of the physical content, on both sides of the duality. It asserts that every field in the bulk of the gravitational theory acts as a source for a local operator in the field theory. The sources themselves correspond to the leading, usually non-normalizable falloff in the asymptotic behaviour of the bulk fields, in agreement with the fact that local operators describe short-distance physics.

Further simplifications occur when we consider the limit $1 \ll \lambda \ll N$. The supergravity action is inversely proportional to the 10-dimensional Newton constant G_N and thus scales proportionally to N^2 . Ignoring quantum and stringy corrections therefore allows us to use the saddle-point approximation, yielding

$$\mathcal{Z}_{\text{SUGRA}} \simeq \text{extremum } e^{-I_{\text{SUGRA}}}, \quad (1.22)$$

where I_{SUGRA} is the on-shell supergravity action on $\text{AdS}_5 \times S^5$. As such only the classical equations of motion derived from the on-shell supergravity action are relevant in the description of field theory physics at leading order in N .

On the other hand, for a CFT governed by an action $S[\mathcal{O}]$, the partition function acts as the generating functional of correlation functions

$$\mathcal{Z}_{\text{CFT}}[\phi_0(x)] = \int D\mathcal{O} e^{-S[\mathcal{O}] + \int d^d x \phi_0(x) \mathcal{O}(x)} = \left\langle e^{\int d^d x \phi_0(x) \mathcal{O}(x)} \right\rangle_{\text{CFT}}.$$

Thus a theory with $\mathcal{Z}[\phi_0(x)]$ corresponds to a deformation of the pure CFT

$\mathcal{Z}[0]$ by a source $\phi_0(x)$. At strong coupling, where perturbation theory does not apply, one may instead compute expectation values, Green's functions and higher-order connected correlators in gauge theory by taking functional derivatives of the generating functional of connected correlation functions

$$W[\phi_0(x)] = -\log \left\langle e^{\int d^d x \phi_0(x) \mathcal{O}(x)} \right\rangle_{\text{CFT}} \simeq I_{\text{SUGRA}}, \quad (1.23)$$

subject to appropriate boundary conditions.

In particular, an important lesson one can learn from (1.23) is that expectation values of sourced operators in the field theory can be recovered easily by looking at the asymptotic falloff of the bulk fields themselves. For illustrative purposes, consider a scalar field $\phi = \phi(r)$ in AdS_{d+1} subject to the Klein-Gordon equation

$$-\frac{1}{\sqrt{-g}} \partial_\mu (\sqrt{-g} g^{\mu\nu} \partial_\nu \phi) + m^2 \phi = 0. \quad (1.24)$$

Near the boundary, the ansatz $\phi \sim r^{-\Delta}$ reveals that the above equation is satisfied only if the condition

$$\Delta(\Delta - d) = m^2 L^2 \iff \Delta_\pm = \frac{d \pm \sqrt{d^2 + 4m^2 L^2}}{2} \quad (1.25)$$

is met. Defining $\Delta = \Delta_+$ as the largest root, we learn that the scalar field has two independent falloffs near the boundary

$$\phi \sim \frac{\phi_0}{r^{d-\Delta}} + \frac{\phi_1}{r^\Delta}. \quad (1.26)$$

We thus identify the coefficient of the leading mode ϕ_0 as the source (on which we impose Dirichlet boundary conditions in AdS), whereas holographic renormalization [12, 13] informs us that ϕ_1 measures the response $\langle \mathcal{O}(x) \rangle$ to that source on the boundary. In terms of the dual field theory, Δ (and thus the mass m) corresponds to the conformal dimension of the operator \mathcal{O} . Moreover, nothing prohibits m^2 from taking negative values in AdS spacetimes since the normalizable mode proportional to ϕ_1 decays in the limit $z \rightarrow 0$ instead of becoming unstable. In fact, taking $m^2 L^2 < 0$ corresponds to taking $\Delta < d$, thereby making \mathcal{O} a relevant operator, and the only requirement is that the mass squared is above the *Breitenlohner-Freedman (BF) bound*, $m^2 \geq m_{BF}^2 = -(d/2L)^2$, otherwise the dimension Δ becomes unphysically complex [14]. Note that the above discussion is general in that non-normalizable modes correspond to sources, normaliz-

able ones are related to operator expectation values, and mass dictates the conformal dimension of the dual field theory operators⁴.

Equation (1.23) therefore arms us with a useful prescription to easily compute correlation functions of strongly interacting fields with geometric bulk constructs. It also provides a non-trivial check on the correspondence since both quantities can be calculated on both sides. The agreement between the CFT calculations, where conformal symmetry constrains the structure of n -point functions, and their counterpart in anti-de Sitter space was of great help in affirming the validity of the correspondence initially.

The above prescription also yields a way to identify which bulk fields act as sources for which boundary operators. Let's consider a charge density deformation for concreteness. The introduction of a vector field a_μ coupled to a current j^μ in the boundary theory amounts to inserting a term

$$\delta S = - \int d^d x a_\mu(x) j^\mu(x) \quad (1.27)$$

in the CFT action

$$\mathcal{Z}_{\text{CFT}} = \int D\mathcal{O} e^{-\int d^d x (\mathcal{L} - a_\mu j^\mu)}. \quad (1.28)$$

The vector field $a_\mu = (\mu, \vec{v}_s)$, whose components are the chemical potential μ and the superfluid velocity \vec{v}_s , is associated with the conserved Noether current j^μ due to the invariance of the theory under *global* $U(1)$ rotations $\mathcal{O} \rightarrow e^{-i\alpha} \mathcal{O}$. Thus we identify $j^0 = \rho(x)$ as being the charge density of the boundary theory with conserved charge $Q = \int d^{d-1} x \rho(x)$, and j^i as the electric currents. It can be shown that for matter fields \mathcal{O}

$$S[\mathcal{O}, \partial_\mu \mathcal{O}] - a_\mu j^\mu \sim S[\mathcal{O}, D_\mu \mathcal{O}] \quad (1.29)$$

with $D_\mu = \partial_\mu - i a_\mu$. In other words, the chemical potential and the superfluid velocities enter the CFT as the components of a $U(1)$ gauge field despite actually being related to a global symmetry. This can be mimicked on the gravity side by introducing a bulk gauge field having a_μ as its asymptotic value. The corresponding supergravity deformation

$$\delta I = -\frac{1}{4} \int d^{d+1} x \sqrt{-g} F_{\mu\nu} F^{\mu\nu}, \quad F_{\mu\nu} = \nabla_\mu A_\nu - \nabla_\nu A_\mu \quad (1.30)$$

⁴Note that both falloffs for the scalar field are normalizable for $-d^2/4 < m^2 L^2 < -d^2/4 + 1$, leading to two different CFTs with operators of dimensions Δ_\pm depending on our choice of boundary conditions [15].

with the boundary condition $A_\mu(r \rightarrow \infty) = a_\mu$ satisfies this condition naturally. In this case the $U(1)$ symmetry, previously associated to a conserved electric current on the boundary, now has the interpretation of a gauge symmetry in the bulk.

The identification between bulk gauge invariance and global symmetries on the boundary is in fact general and applies to all bulk gauge fields and their associated conserved currents, as long as both possess the same Lorentz structure and quantum numbers. A particularly interesting instance of this property is the natural coupling between the bulk metric and the boundary energy-momentum tensor, which effectively maps the diffeomorphism invariance of the metric to global symmetries arising from Lorentz invariance. This is a deep connection that we will revisit in more detail when we introduce the characteristic formulation of general relativity in AdS spacetimes.

1.3 Literature Review

Now that we have provided arguments that support the validity of the gauge/gravity, we turn our attention to specific applications. In particular we examine the holographic realization of unconventional superconductors and discuss entanglement propagation in strongly interacting many-body systems via the lens of gauge/gravity. We also introduce the perturbative framework of general relativity when the number of spacetime dimensions is large, and end with a short discussion on the numerical methods used throughout this thesis.

1.3.1 Holographic Superconductors

Chapter 2 initiates the study of holographic $p + ip$ Josephson junctions. Josephson junctions are quantum devices constructed by inserting a thin layer of normal metal or insulator between two superconducting electrodes and exhibit various interesting properties that arise as a consequence of broken gauge invariance in the superconducting phase. In this section we show how to use the gauge/gravity duality to build a superconductor and then discuss interesting properties of Josephson junctions and their holographic realization.

Conventional superconductors

Conventional superconductors, which undergo a phase transition between metallic and superconducting states at low temperatures, are best understood from the BCS theory point of view [16]. Consider a gas of electrons on a lattice made of positive ions. At high temperatures, the dominating force between electrons is their Coulomb repulsion, resulting in a metalling state. However, as the temperature is lowered the interaction between electrons close to the Fermi surface becomes attractive due to phonon interactions from the lattice, resulting in the binding of electrons in Cooper pairs. The key discovery of [16] was to show that these pairs, being composite bosons, are prone to condense, which in turn changes the electronic behaviour and opens up a band gap E_g in the energy spectrum. It is this gap which is responsible for superconductivity, effectively preventing electron scattering and other small energy excitations to ensure non-dissipative electronic flow.

At the level of symmetries, it is commonly said that the Cooper pair condensate acquires a vacuum expectation value and spontaneously breaks the local $U(1)$ electromagnetic gauge symmetry down to the \mathbb{Z}_2 of particle-hole symmetry, in accordance with the Anderson-Higgs mechanism [17, 18]. Put differently, the Higgs mechanism causes the electron phase to be absorbed inside a massive vector field a_μ whose gauge-invariant components are the chemical potential and superfluid velocities [19]. This situation is reminiscent of our earlier treatment of global $U(1)$ symmetries in AdS/CFT, which we summarized via the equivalence

$$S[\mathcal{O}, \partial_\mu \mathcal{O}] - a_\mu j^\mu \sim S[\mathcal{O}, D_\mu \mathcal{O}]. \quad (1.31)$$

This similarity strongly suggests that spontaneously breaking gauge invariance in the bulk could generate superconductivity on the boundary. and it was only a matter of time until all of the ingredients were assembled in the gauge/gravity duality to build a holographic superconductor.

Holographic superconductors

The model that we introduce in what follows provides a microscopic description of superconductivity at strong coupling via its dual gravitational interpretation. Indeed, holographic superconductivity arises without the need for quasiparticles; the onset of superconductivity below a critical temperature is diagnosed via the condensation of a charged scalar operator, and the theory is formulated entirely in terms of conserved charges, currents, and expectation values. The hope is that this first-principle model of supercon-

ductivity may help elucidate the more elusive properties of unconventional materials, such as the high- T_c cuprates.

A simple Abelian Higgs model in asymptotically anti-de Sitter space-time was first proposed in [20] to show that, under certain conditions, the necessary symmetry-breaking ingredients could be achieved in the bulk to reproduce superconductivity on the boundary theory [21, 22]. Consider the Lagrangian

$$\mathcal{L} = R - \frac{6}{L^2} - \frac{1}{4}F_{\mu\nu}F^{\mu\nu} - |\partial_\mu\psi - iqA_\mu\psi|^2 - m^2|\psi|^2. \quad (1.32)$$

The first two terms correspond to the Hilbert-Einstein action for asymptotically AdS₄ spacetimes, while the remaining terms correspond to the Higgs sector, composed of a charged scalar field $\psi = \psi(r)$ and an Abelian gauge field $A = \phi(r) dt$. Let's simplify things further by taking $m^2 = -2$ and considering the *probe limit*. Taking $q \rightarrow \infty$ while keeping both $\bar{\psi} = q\psi$ and $\bar{\phi} = q\phi$ fixed in the equations of motion resulting from (1.32) results in both of them dropping out of Einstein's equations, yielding the Schwarzschild-AdS₄ black hole solution

$$ds^2 = -f(r)dt^2 + \frac{dr^2}{f(r)} + r^2(dx^2 + dy^2), \quad f(r) = \frac{r^2}{L^2} \left(1 - \frac{r_0^3}{r^3}\right) \quad (1.33)$$

with Hawking temperature

$$T = \frac{3r_0}{4\pi L^2} \quad (1.34)$$

and effectively preventing matter fields from backreacting on the geometry. Note that we can use scaling symmetries to set $L = r_0 = 1$, which we do now. For their part, the Maxwell and Klein-Gordon equations

$$\phi'' + \frac{2}{r}\phi' - \frac{2\psi^2}{f}\phi = 0 \quad (1.35a)$$

$$\psi'' + \left(\frac{f'}{f} + \frac{2}{r}\right)\psi' + \left(\frac{\phi^2}{f^2} + \frac{2}{f}\right)\psi = 0 \quad (1.35b)$$

remain unchanged, and the asymptotic behaviour of ψ and ϕ reveals the properties of the boundary field theory. Asymptotic analysis shows that

$$\phi = \mu - \frac{\rho}{r} + \dots \quad (1.36)$$

$$\psi = \frac{\psi^{(1)}}{r} + \frac{\psi^{(2)}}{r^2} + \dots \quad (1.37)$$

as $r \rightarrow \infty$. We choose not to source the scalar field by setting $\psi^{(1)} = 0$; this ensures that solutions with $\langle \mathcal{O} \rangle \equiv \sqrt{2}\psi^{(2)} \neq 0$ (and thus $\psi \neq 0$) spontaneously break gauge invariance in the bulk and thus the $U(1)$ symmetry on the boundary, as is expected from Cooper pair condensation in conventional superconductors. Given the isotropy of the scalar operator in the boundary theory, such symmetry-breaking solutions correspond to s -wave holographic superconductors.

As it turns out, the solutions to equations (1.35) do depend on the *dimensionless* ratio T/μ of the black hole solution. Note that there are only two inequivalent temperatures in a conformal field theory: zero and non-zero. In our case the chemical potential deforms the dual field theory by introducing a new scale, and maintaining scale invariance requires that all equilibrium quantities depend uniquely on T/μ . Thus changing μ amounts to changing the temperature of the boundary theory, which we can do continuously. To identify the critical temperature T_c at which the phase transition occurs, it is possible to use either μ or ρ since $T_c \propto \mu \propto \sqrt{\rho}$.

At higher temperatures, which we control by keeping $T = 3/4\pi$ and taking μ small, the only solution to (1.35) is

$$\phi = \mu \left(1 - \frac{1}{r}\right), \quad \psi = 0, \quad (1.38)$$

which corresponds to a normal metal in the dual theory. However, lowering the temperature yields a second-order phase transition in the order parameter $\langle \mathcal{O} \rangle$, as shown in Figure 1.8.

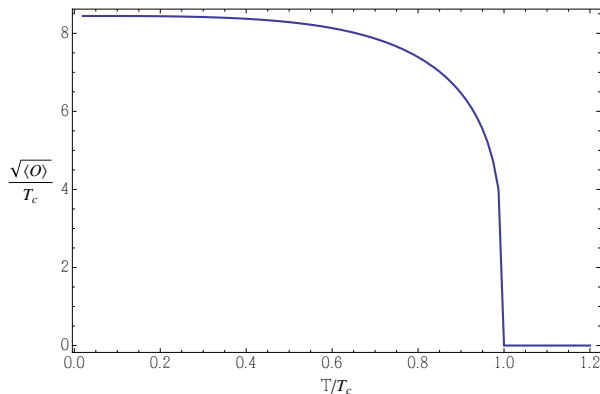


Figure 1.8: The normalizable falloff $\psi^{(2)} \sim \langle \mathcal{O} \rangle$ serves as an order parameter for the superconducting phase transition of an s -wave superconductor.

The underlying mechanism explaining why $\psi \neq 0$ involves the effective mass of the scalar due to its coupling to the gauge field via covariant derivatives

$$m_{\text{eff}}^2 = m^2 + g^{tt} q^2 \phi^2. \quad (1.39)$$

Very close to the horizon, there is a competition between $g^{tt} \rightarrow -\infty$ and $\phi \rightarrow 0$. A stability analysis of black hole perturbations showed that the effective mass (1.39) is driven below the BF bound at low enough temperatures due to the near-horizon profile of the gauge field, in such a way that the theory becomes unstable to scalar condensation. Thus not only does this gravitational solution provide a dual description of superconductivity at strong coupling, it also acts as one of the few counterexamples to the long-standing conjectures that black holes cannot have stable *hair*.

Indeed, it is worth mentioning that it is a remarkable discovery for solutions with $\psi \neq 0$ to exist in the bulk. In general relativity, such uncommon solutions are called *hairy* black holes, where hair is defined as the free parameters of a black hole not subject to a Gauss law [23]. In fact most black hole solutions with hair were known to be unstable, including neutral AdS black holes with neutral scalar hair [24], until [20] showed that Reissner-Nordstrom black holes in AdS are stable (i.e. are a minimum of the free energy) under condensation of highly charged scalars.

We now turn attention to the study of the electric conductivity of the dual field theory to show that the above setup is indeed a holographic realization of a superconductor. This is done by linearizing the Maxwell equations about a perturbation A_x , for which we allow a time dependence $e^{-i\omega t}$. The conductivity can then be calculated from Ohm's law (see Figure 1.9)

$$\sigma(\omega) = \frac{\langle J_x \rangle}{E_x} = -\frac{iA_x^{(1)}}{\omega A_x^{(0)}}, \quad \text{where } A_x = A_x^{(0)} + \frac{A_x^{(1)}}{r} + \dots \quad (1.40)$$

An interesting observation is the presence of an infinite DC conductivity ($\omega = 0$) for $T < T_c$, as is expected from a superconducting phase. A gap frequency ω_g can be extracted from the electric conductivity by looking at where $\text{Re}(\sigma)$ stops being exponentially suppressed. Note that the real part of the conductivity is related to dissipative processes, and the presence of a gap signals non-dissipative electric currents for $\omega \lesssim \omega_g$ and implies the presence of an energy gap in the band spectrum.

A surprising feature of holographic superconductivity is the regularity $\omega_g \approx 8T_c$ across all masses $m^2 > m_{\text{BF}}^2$ for both $d = 3$ and 4 [25]. Comparing to the BCS theory result $\omega_g \approx 3.5T_c$, we conclude that holographic supercon-

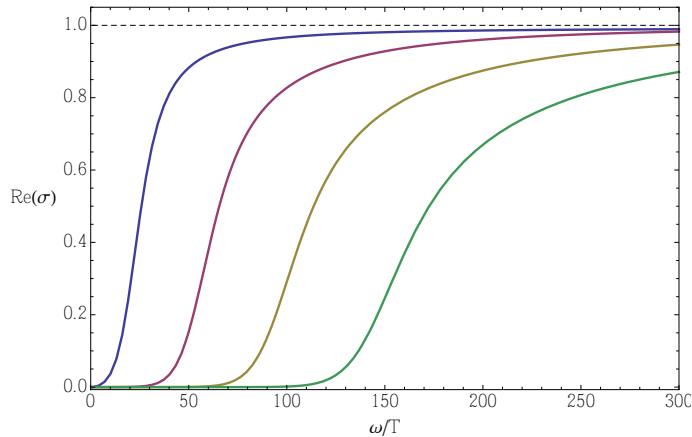


Figure 1.9: This image shows the formation of a conductivity gap in the dissipative part of the conductivity. This gap increases as the temperature is lowered; from left to right, these curves have $\mu = 5, 7, 9, 11$.

ductors are indeed strongly coupled as they require more energy to overcome the conductivity gap. We also note that the relation $\omega_g = 2E_g$ between the conductivity and band gaps is only applicable for weakly coupled systems in which there is a pairing mechanism at work. The band gap for holographic superconductors may be extracted via the relation $\text{Re}(\sigma) \approx e^{-E_g/T}$ at small frequencies, and we generally observe a non-integer proportionality between the two gaps, indicative of the absence of a quasiparticle interpretation [22].

In addition to the symmetry breaking condensate and the properties of the conductivity, this gravitational model shares other similarities with real superconductors, namely in its behaviour when exposed to magnetic fields (generation of screening currents, existence of a magnetic penetration depth, formation of superconducting droplets, etc.) [22].

Other symmetry-breaking solutions have also been found for which the order parameter exhibits different symmetries (for a review, see [26]). For instance, rather than introducing a scalar charged under a $U(1)$ gauge field, it was instead proposed to consider an $SU(2)$ Yang-Mills theory in the bulk where the $U(1)$ subgroup of $SU(2)$ is identified with the electromagnetic gauge symmetry [27, 28]. The generators of $SU(2)$ satisfy the relation $[\tau^b, \tau^c] = \epsilon^{abc} \tau^a$, where τ^a are related to the Pauli matrices and ϵ^{abc} is the antisymmetry tensor. Choosing τ^3 as the generator of the electromagnetic

$U(1)$, the gauge field ansatz $A = A_\mu^a \tau^a dx^\mu$ with

$$A = \phi(r)\tau^3 dt + w(r)\tau^1 dx \quad (1.41)$$

breaks rotational invariance by picking the x direction as special, thereby giving rise to a p_x -wave superconductor when the order parameter w condenses. Similarly, the ansatz

$$A = \phi(r)\tau^3 dt + w(r) (\tau^1 dx + \tau^2 dy) \quad (1.42)$$

preserves a combined gauge and spatial rotation such that the resulting holographic superconductor is of $p+ip$ -type symmetry. Both solutions break time-reversal invariance since the condensate w appears as a magnetic field in $F_{\mu\nu}^3$. These additional features allow us to make more precise statements about the connection between holographic models and real-life materials such as the cuprates, which exhibit similar properties [29, 30].

In light of all the above, attempts to study exotic theories with the tools of the gauge/gravity duality indeed look promising. Despite the deceptively simple nature of the models considered, one can hope that the underlying foundational principles may reveal generic features of strongly coupled field theories.

Josephson junctions and their holographic realizations

We now turn our attention to Josephson junctions [31], a quantum device made of two superconductors (S) separated by a weak link, typically an insulator (I) or a normal metal (N). SIS and SNS junctions exhibit a peculiar phenomenon called the *Josephson effect* in which a supercurrent may flow from one superconducting electrode to the other even in the absence of an externally applied voltage. This phenomena is due to the proximity effect, explained microscopically at weak coupling by a charge-transfer process known as Andreev reflection whereby the electrons in the weak link transfer the order of the superconducting condensate across the interface, giving rise to a supercurrent. The proximity effect can be thought of as a macroscopic quantum tunnelling of charge [32].

Josephson junctions thus provide a clear example that lowering the degree of symmetry in a system can lead to novel phenomena. The consequence of spontaneously breaking $U(1)$ gauge invariance is that superconductors “pick up” a particular phase, and it is precisely the gauge-invariant phase difference $\Delta\varphi$ between the two superconducting layers that is responsible

for the Josephson current, whose magnitude is

$$J = J_{\max} \sin(\Delta\varphi). \tag{1.43}$$

At the level of symmetries, the Josephson effect occurs as a consequence of spatial discontinuity of the superconducting material. Given that holographic duals are sensitive to the underlying symmetry structure, the holographic realization of such a junction should be possible.

As a matter of fact, a holographic Josephson junction was first constructed in [33] by letting the chemical potential of the Abelian Higgs model vary spatially in such a way that two superconducting regions would be separated by a normal metal. The resulting system of equations can be solved numerically; an asymptotic analysis of A_x , whose presence is required since translation invariance is broken, reveals that the behaviour (1.43) can be reproduced with remarkable precision. Moreover, it was found that the magnitude of the maximal current J_{\max} decayed exponentially with the size of the metallic link as the proximity effect weakens. Now then how does having an order parameter with different symmetry properties affect the physics of Josephson junctions? We answer this question in more detail in chapter 2.

1.3.2 Entanglement Entropy

We now steer away from the condensed matter applications of the holographic duality to take a deeper look at a quite remarkable entry in the AdS/CFT dictionary, which relates the entanglement entropy of a subregion in the dual field theory to the area of a bulk extremal surface anchored on its boundary. In what follows we define the notion of entanglement entropy, outline how to compute its value geometrically, and discuss constraints on entanglement propagation in the context of holography.

Holographic entanglement entropy

When investigating the properties of a quantum field theory, a physicist's first instinct is to look at the correlation functions of its local operators. The motivation is simple: all dynamical quantities describing the system, such as scattering cross sections and decay rates of particles, can be derived from these correlators. However, lessons from QFT at strong coupling teach us that some non-local quantities are crucial in characterizing a theory's phase structure. For instance, the confinement-deconfinement transition of QCD employs gauge-invariant Wilson loops as an order parameter.

Entanglement entropy is another example of a non-local physical quantity of great interest. As its name suggests, the entanglement entropy of a region gives a measure of how the degrees of freedom localized within are entangled with the rest of the system. Beyond determining the number of operative degrees of freedom in a QFT, entanglement entropy is also used as an order parameter for characterizing topological states of matter not readily described by the symmetry breaking paradigm. Understanding this quantity better may thus provide new perspectives in the methods we use to investigate field theories.

Consider a system described by a pure quantum state $|\Psi\rangle$, with density matrix $\rho = |\Psi\rangle\langle\Psi|$. The von Neumann entropy of the total system

$$S = -\text{Tr } \rho \log \rho \tag{1.44}$$

is necessarily zero, by virtue of $|\Psi\rangle$ being a pure state. We now divide the system into two regions, \mathcal{A} and its complement \mathcal{B} . This partitioning amounts to separating the total Hilbert space of the system as $\mathcal{H} = \mathcal{H}_{\mathcal{A}} \otimes \mathcal{H}_{\mathcal{B}}$. As a result, one may describe the state of the degrees of freedom within \mathcal{A} with total ignorance of what goes on in \mathcal{B} via the reduced density matrix $\rho_{\mathcal{A}} = \text{Tr}_{\mathcal{B}} \rho$, where the trace is taken over $\mathcal{H}_{\mathcal{B}}$. The bipartite entanglement entropy is thus defined as the von Neumann entropy of the reduced density matrix

$$S_{\mathcal{A}} = -\text{Tr}_{\mathcal{A}} \rho_{\mathcal{A}} \log \rho_{\mathcal{A}}. \tag{1.45}$$

For purely quantum system, $S_{\mathcal{A}} = S_{\mathcal{B}}$, whereas the above measure mixes both entanglement and thermal entropies at finite temperature and $S_{\mathcal{A}} \neq S_{\mathcal{B}}$. Entanglement entropy in d dimensional QFTs is also known to obey an area law⁵ [35, 36]

$$S_{\mathcal{A}} = \alpha \frac{\text{Area}(\partial\mathcal{A})}{\epsilon^{d-2}} + \text{finite terms}, \tag{1.46}$$

where α is a context-dependent constant and the UV cutoff ϵ is introduced to model the divergence of entanglement entropy in the continuum limit. This non-extensive property has an intuitive interpretation: the quantum entanglement between \mathcal{A} and its complement \mathcal{B} is strongest at their boundary $\partial\mathcal{A}$ and thus scales as the area of the boundary rather than with the volume within. It also evokes a curious connection with the Bekenstein-Hawking

⁵In the case of a 1+1 CFT at criticality, entanglement entropy scales logarithmically with the size of \mathcal{A} [34].

entropy for black holes

$$S_{\text{BH}} = \frac{\text{Area of horizon}}{4G_N}. \quad (1.47)$$

Indeed, a black hole can be thought of as the inaccessible region \mathcal{B} whose degrees of freedom are traced out when computing the reduced density matrix $\rho_{\mathcal{A}}$. However issues related to the microscopic origin of entanglement, namely the dependence of entanglement entropy on the number of matter fields and on an ultraviolet cutoff, prevent the full realization of this intriguing connection [37]. Despite these subtleties, the intuitive similarity between entanglement entropy and black hole entropy still served as a strong motivation for the holographic proposal of Ryu-Takayanagi (RT), which we now discuss.

For time-independent $d+1$ dimensional asymptotically AdS spacetimes, it was first proposed in [38, 39] that the entanglement entropy of a boundary region \mathcal{A} is proportional to the area of the *minimal surface* $\gamma_{\mathcal{A}}$ anchored on its boundary $\partial\mathcal{A}$

$$S_{\mathcal{A}} = \frac{\text{Area}(\gamma_{\mathcal{A}})}{4G_N^{(d+1)}}. \quad (1.48)$$

The minimal surface $\gamma_{\mathcal{A}}$ is a codimension-2 surface in the bulk that acts as the holographic screen⁶ with the most severe entropy bound on the lost information [40]. The Ryu-Takayanagi proposal has been very successful in reproducing the analytical results found for the entanglement entropy of 1+1 dimensional CFTs. As for higher dimensional CFTs, the computation of entropy is usually complicated and not amenable to analytic results, in which case the alternative method (1.48) is of great help in uncovering some of the more elusive properties typical of strongly coupled systems.

Calculating entanglement entropy from the area of minimal surfaces is a notion that makes sense in static spacetimes, but the generalization to time-dependent settings is not an immediate one. Minimal surfaces are an ill-defined concept in Lorentzian spacetimes since perturbations in the timelike direction can be made to decrease their area indefinitely. This difficulty can be avoided in the static case by either Wick-rotating time to obtain a Euclidean geometry, or by restricting our attention to slices of constant time. In other words, the notion of time on the boundary can be seen to extend naturally in the bulk for static spacetimes such that there exists a canonical foliation by codimension-1 spacelike surfaces containing the minimal surfaces

⁶By holographic screen we mean a bulk surface γ whose boundary $\partial\gamma = \partial\mathcal{A}$ isolates region \mathcal{A} from its complement, “shielding” it from the latter’s degrees of freedom.

of interest. The addition of time-dependence is trivial from the field theory point of view since there still exists a natural Hamiltonian notion of time for dynamical QFTs in fixed backgrounds. However, from a gravitational perspective we need to ensure that the geometric construction (1.48) can be generalized in a covariant way to account for diffeomorphism invariance in the bulk.

A covariant holographic entanglement entropy proposal was first outlined in [41]. In Lorentzian spacetimes, the concept of minimal surface is instead replaced by that of *extremal* surface, i.e. a saddle point of the area functional

$$\text{Area}(\mathcal{E}) = \int_{\mathcal{E}} d^{d-1}y \sqrt{\det \tilde{g}}, \quad (1.49)$$

where $\tilde{g}_{\alpha\beta}$ is the induced metric on \mathcal{E} described by coordinates y^α . The construction proposed in [41] involves light-sheets, which are trapped manifolds corresponding to congruences of null geodesics with non-positive expansions (expansions measure the fractional rate of change of a geodesic congruence's cross-sectional area [42]) (see Figure 1.10). The extremal surface \mathcal{E}_A is then simply the intersection of future- and past-directed light-sheets with van-

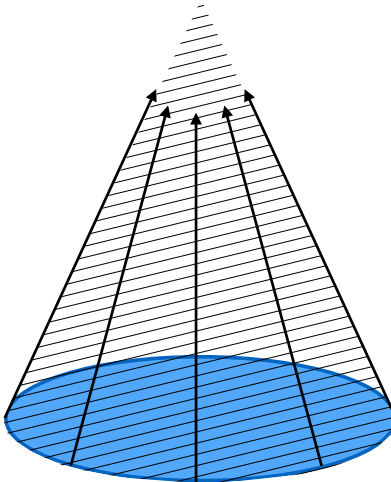


Figure 1.10: Depiction of a light-sheet. A codimension-2 spacelike surface on the boundary (in blue) necessarily has four congruences of null geodesics: future/past directed outgoing/ingoing geodesics. The converging (i.e. non-positive expansion) light rays shown above form a light-sheet in the bulk.

ishing expansions, a condition that results in a stationary point of (1.49). With $\mathcal{E}_{\mathcal{A}}$ constructed this way, we obtain the time-dependent covariant entanglement entropy

$$S_{\mathcal{A}}(t) = \frac{\text{Area}(\mathcal{E}_{\mathcal{A}})}{4G_N^{(d+1)}}. \quad (1.50)$$

Initially formulated as conjectures, the Ryu-Takayanagi proposal and its covariant analogue have since both been derived from AdS/CFT first principles [43, 44], thereby firmly cementing their presence in the holographic dictionary. Furthermore, holographic entanglement entropy satisfies many non-trivial properties, such as consistency with field theory causality [45] in the covariant case, positivity, continuity, sub-additivity ($S_{\mathcal{A}_1} + S_{\mathcal{A}_2} \geq S_{\mathcal{A}}$ for $\mathcal{A} = \mathcal{A}_1 \cup \mathcal{A}_2$) and many other inequalities that follow from the properties of density matrices [46]. All of these results reveal intriguing connections between quantum information and geometry, and further investigation on both sides of the duality are bound to reveal additional insights about the fundamental nature of entanglement.

Far-from-equilibrium physics and entanglement propagation

With a time-dependent prescription to compute entanglement entropy in hand, we now find ourselves in a position to ask interesting questions about the thermalization of entanglement for strongly coupled field theories in non-equilibrium settings. Methods for driving a system out of equilibrium that can be reproduced both in experimental setups and in holographic models include quantum *quenches*, which are deformations of the theory occurring over a relatively short timescale. In a field theory, one may quench a system by modifying the Hamiltonian and letting the former eigenstate evolve to its new equilibrium. Alternatively, one may excite the ground state of a system by turning on a collection of sources for a short period of time. The work done by the sources will drive the system into an excited state that will eventually return to equilibrium according to the initial Hamiltonian's dynamics.

Understanding the dynamics of quantum matter out of equilibrium is no easy task, yet holography provides a simple toy model that may offer a universal characterization of non-equilibrium processes. One of the most common type of holographic quench in the AdS/CFT literature is a global quench modelled after the time-dependent Vaidya metric written in

Eddington-Finkelstein coordinates

$$ds^2 = \frac{L^2}{z^2} (-f(v, z)dv^2 - 2dv dz + d\vec{x}^2), \quad f(v, z) = 1 - \Theta(v)g(z). \quad (1.51)$$

The $\Theta(v)$ function is such that spacetime is pure AdS for $v < 0$, whereas it is determined by the black hole geometry dictated by $g(z)$ for $v > 0$. The Vaidya-AdS metric models an infinitely thin shell of null dust collapsing into a black hole and is thus dual to a thermal quench where a field theory is uniformly and rapidly injected with energy from an external source.

This setup has been studied extensively [47–61] in a wide variety of contexts, including but not limited to the study of dynamical correlation functions and Wilson loops, observations of universal scaling laws of boundary observables, quenches with charged matter, thermalization of mutual and tripartite information, and generalizations to non-relativistic theories. In particular, [47, 61] thoroughly investigated the thermalization of entanglement entropy in the Vaidya-AdS geometry and found a universal characterization of entanglement growth. For a spatial region bounded by a surface Σ of size R , an analysis of entanglement entropy at macroscopic scales $R \gg \ell_{\text{eq}}$ reveals that

$$\Delta S_{\Sigma}(t) = s_{\text{eq}} (V_{\Sigma} - V_{\Sigma - v_E t}) + \dots, \quad (1.52)$$

which suggests that entanglement propagates locally, carried by a wave-front dubbed *entanglement tsunami* travelling at velocity v_E as in Figure 1.11.

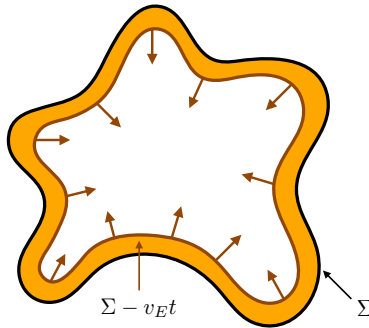


Figure 1.11: Illustration of entanglement growth via the entanglement-carrying wavefront $\Delta S_{\Sigma}(t) = s_{\text{eq}} (V_{\Sigma} - V_{\Sigma - v_E t})$, also dubbed entanglement tsunami. The yellow region is entangled with the exterior of Σ while the white region has not been affected yet. Figure adapted from [47].

In this scenario, $\ell_{\text{eq}} \sim z_h \sim s_{\text{eq}}^{-1/(d-1)}$ denotes the time scale after which production of thermal entropy ceases to occur locally post-perturbation at the microscopic level, and the condition $R \gg \ell_{\text{eq}}$ effectively precludes the study of narrow entangling regions, instead focusing on macroscopic regions whose extremal surfaces probe the deepest part of the IR geometry.

The tsunami velocity can be extracted from the metric (1.51); it is equal to

$$v_E = \left(\frac{z_h}{z_m} \right)^{d-1} \sqrt{-g(z_m)}, \quad (1.53)$$

where z_m minimizes $g(z)z^{-2(d-1)}$. Note that v_E is a property of the field theory at equilibrium since it is derived from the black hole geometry. As such, it is independent of the details of the initial state. Moreover, it is natural to expect that the addition of matter sources reduces the efficiency of equilibration processes. In the bulk, this translates into the statement that for general black hole geometries, $v_E \leq v_E^{(S)}$, where the latter is the tsunami velocity of a Schwarzschild black hole. Thus $v_E^{(S)}$ effectively acts as an upper bound of entanglement growth in strongly coupled systems, which intuitively makes sense since entanglement generation in a gapless field theory is most efficient in the limit of infinite coupling, which corresponds to the Schwarzschild geometry in the language of the correspondence.

Nonetheless, the tsunami picture does not provide a description of the underlying microscopic mechanisms responsible for the spread of entanglement in generic field theories. Consider for instance a 1+1 CFT, for which the entanglement entropy of an interval of length R grows linearly until it saturates after a time $t = R/2$. This behaviour can be understood by considering free-streaming quasiparticles carrying entanglement [62]; the saturation time is then understood to be the time required until all EPR pairs produced locally within the interval meet, thus inducing correlations between local observables (see Figure 1.12). Consequently, interactions may be disregarded since the long-range entanglement of the final state finds its origins from the spread of short-distance correlations.

The free-streaming model can be generalized to higher dimensions and compared to the entanglement tsunami picture [63], but fails to capture important aspects of entanglement growth for strongly interacting systems. Indeed, the tsunami wave-front is found to propagate faster than entanglement-carrying quasiparticles travelling at the speed of light

$$v_E^{(\text{streaming})} = \frac{\Gamma(\frac{d-1}{2})}{\sqrt{\pi}\Gamma(\frac{d}{2})} \leq v_E^{(S)} < 1. \quad (1.54)$$

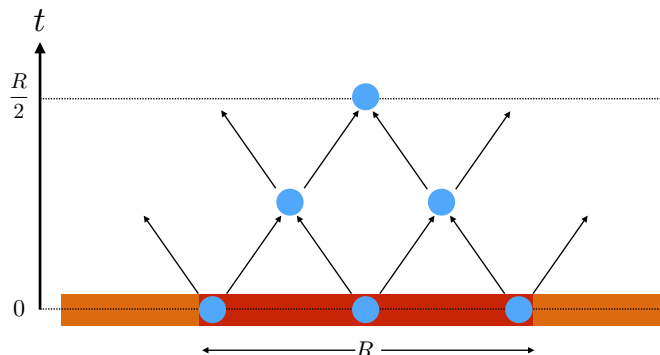


Figure 1.12: The free-streaming model asserts that entanglement is spread via quasiparticles (in blue) propagating at the speed of light. Saturation for a subregion of size R (in red) occurs at $t = R/2$, corresponding to the time it takes for all quasiparticles to correlate with one another.

This observation suggests that the simplified model of [63], despite reproducing many of the scaling behaviours of entanglement found in the Vaidya-AdS setup, is not an appropriate description of entanglement spread in the strong coupling regime because it neglects the crucial role played by interactions. This result is not very surprising considering that the field theories under consideration are not amenable to a quasiparticle description. On that account, the model of [47, 61] only provides predictions rather than explanations of the principles responsible for entanglement propagation, which calls for a closer inspection of entanglement thermalization in holographic setups, which we investigate in chapters 3 and 4.

1.3.3 Large D Limit of General Relativity

The theory of general relativity is, at its heart, a geometric description of gravitational dynamics. The Einstein equations

$$R_{\mu\nu} - \frac{R}{2}g_{\mu\nu} + \Lambda g_{\mu\nu} = \frac{8\pi G_N}{c^4}T_{\mu\nu} \quad (1.55)$$

relate the curvature of spacetime, captured by the Ricci tensor $R_{\mu\nu}$ and its trace R , to the presence of matter, embodied by the energy-momentum tensor $T_{\mu\nu}$. Despite their concise appearance, the Einstein equations are second-order coupled non-linear hyperbolic-elliptical partial differential equations – in other words, very hard to solve. Known analytical solutions usually boast

a high degree of symmetry, which in turn greatly simplifies the equations. However, a myriad of phenomena not prone to such simplifications are also encoded within (1.55), and analytical approaches are far and few between.

Additionally, we have so far used gravity as a tool to study strongly coupled field theories. Occasionally this programme led to novel discoveries about the physics of black holes, such as the possibility of supporting stable scalar hair in AdS spacetimes, but most of the insights were nonetheless gained the other way around. In this section we introduce a new formalism, the large D limit of general relativity, as an attempt at providing an analytical framework to study gravitational systems themselves. Gravity is interesting in its own right but its secrets are generally well-guarded, thus the hope is that this new approximation may yield universal predictions about the classical physics of black holes.

Large D formalism

The large D formalism, which gives a description of gravity when the number of spacetime dimensions tends to infinity, is an approximation that greatly simplifies gravitational dynamics by decoupling the near-horizon region from the rest of spacetime. As a result, large D black holes essentially behave like non-interacting particles of vanishing collision cross-section [64]. Although unrealistic, taking $D \rightarrow \infty$ allows us to make a simplifying expansion in $1/D$ about non-perturbative solutions of Einstein's equations (e.g. black brane solutions) with the expectation that sensible results may be obtained for intermediate values of D .

Let us now examine some of the consequences of taking D to be large. One of the main considerations of this formalism is the introduction of a hierarchy of scales. Take for instance the Schwarzschild-Tangherlini solution with a horizon radius r_0

$$ds^2 = -f(r)dt^2 + \frac{dr^2}{f(r)} + r^2 d\Omega_{D-2}^2, \quad f(r) = 1 - \left(\frac{r_0}{r}\right)^{D-3}. \quad (1.56)$$

Letting $D \rightarrow \infty$ results in a spacetime that is asymptotically flat everywhere outside the horizon. Expanding $f(r)$ in the neighbourhood of $r = r_0$ for D large, we obtain

$$\lim_{D \rightarrow \infty, r \rightarrow r_0} f(r) = \frac{D}{r_0}(r - r_0), \quad (1.57)$$

informing us that the gravitational field is strongly localized in the near-

horizon region

$$r - r_0 \lesssim \frac{r_0}{D} \equiv \ell_\kappa \quad (1.58)$$

and essentially non-existent outside. The new scale ℓ_κ is in fact related to the black hole's gravitational gradient

$$\left. \frac{\partial f}{\partial r} \right|_{r=r_0} \rightarrow \frac{D}{r_0} = \ell_\kappa^{-1} \quad (1.59)$$

as well as to its surface gravity.

This separation of scale is effectively responsible for the decoupling of the near-horizon dynamics from the far-region's; solving the Einstein equations in the overlap region $\ell_\kappa \ll r - r_0 \ll r_0$ simply involves the matching of asymptotic expansions. This is done by requiring regularity at the horizon, which in turn yields effective boundary conditions on large-distance fields from imposing continuity. In spirit, this matching procedure amounts to integrating out the degrees of freedom at scales $< \ell_\kappa$.

In addition to this curvature length ℓ_κ , black holes are also characterized by scales due to their geometry. The area of a unit S^{D-2} in the large D limit is

$$\Omega_{D-2} \sim \frac{D}{\sqrt{2\pi}} \left(\frac{2\pi e}{D} \right)^{D/2}, \quad (1.60)$$

which leads us to define an area/entropy length scale ℓ_A related to the event horizon's area

$$\ell_A \sim A_H^{1/(D-2)} \sim \frac{r_0}{\sqrt{D}}. \quad (1.61)$$

We thus find a hierarchy: $\ell_\kappa \ll \ell_A \ll r_0$. A surprising aspect of the large D formalism is that the notion of short distances arises from the parametric dependence of these length scales on D rather than from the usual comparison of distances with the horizon radius. This hierarchy is important since each scale, once fixed, defines what physical regime we home in as we take D to infinity. We can see this concretely by comparing the Gregory-Laflamme instability with black hole quasinormal modes. On one hand, when D is large black branes are unstable to perturbations with wavelengths larger than

$$\lambda_{\text{GL}} = \frac{2\pi}{k_{\text{GL}}} = \frac{2\pi r_0}{\sqrt{D}} (1 + \mathcal{O}(D^{-1})). \quad (1.62)$$

Consequently an appropriate rescaling of the spatial directions along the brane $d\vec{x} \rightarrow d\vec{x}/\sqrt{D}$ is necessary to capture the physics of interest since the degrees of freedom $< \lambda_{\text{GL}}$ are effectively irrelevant. On the other hand,

black hole quasinormal modes are characterized by very large frequencies

$$\text{Re } \Omega_{\text{QN}} \sim \frac{D}{r_0}, \quad (1.63)$$

which is an entirely different regime from the Gregory-Laflamme spectrum $\Omega_{\text{GL}} r_0 \sim \mathcal{O}(D^0)$. As such a study of quasinormal modes at large D will simply ignore black brane instabilities.

These geometric considerations need to be kept in mind when investigating gravitational dynamics of large D systems, or else we might miss effects we might be interested in. A similar argument applies in the presence of matter fields. For example, the addition of a $U(1)$ gauge field necessarily introduces a new length scale – in this case a “charge radius” – which measures the gravitational reach of electromagnetism away from the horizon. A corollary of this discussion is that non-geometric quantities like mass or angular momentum are not natural in the large D language; conversion constants such as Newton’s constant are needed to assign a conceptually clear meaning to them.

Finally, an important aspect of this formalism is that it makes no claim about the range of validity and the accuracy of this expansion for intermediate values of D . Such questions are best answered on a case-by-case basis. However, this approximation is surprisingly successful in capturing some robust features of higher-dimensional black holes, such as their quasinormal modes and the generic Gregory-Laflamme instability that afflicts them, even at low values of D . In fact the largest deviations in the unstable black string’s spectrum when $D = 7$ is about 4%, decreasing to 1% when $D = 8$ and much lower as D is increased [64, 65]. Such optimistic results are of course encouraging the pursuit of new knowledge in this direction.

Gregory-Laflamme instability

We now conclude this section with a short introduction to the Gregory-Laflamme instability [66, 67], a surprising phenomenon found in higher dimensional ($D > 4$) gravity.

As we have already discussed, four-dimensional static black holes in flat space are stable to linearized perturbations and uniquely determined by their mass, charge and angular momentum. Their topology is also fixed; only spherical event horizons are allowed. These constraints are easily relaxed when considering higher-dimensional black holes, as we can see from comparing two equally valid solutions when $D = 5$. The Schwarzschild

solution can be generalized to

$$ds^2 = -V_5(r)dt^2 + \frac{dr^2}{V_5(r)} + r^2 d\Omega_3^2, \quad V_5(r) = 1 - \frac{r_5^2}{r^2}. \quad (1.64)$$

This black hole has an event horizon located at radius

$$r_5^2 = \frac{8G_N^{(5)}M}{3\pi}. \quad (1.65)$$

We can alternatively consider the view where we add an extra linear dimension z to the four-dimensional Schwarzschild solution. Assuming that nothing depends on this new dimension, the $D = 4$ black hole solution is also a solution to $R_{5a} = 0$, by construction. This is the so-called black string

$$ds^2 = -V(r)dt^2 + \frac{dr^2}{V(r)} + r^2 d\Omega_2^2 + dz^2, \quad V(r) = 1 - \frac{r_0}{r}, \quad (1.66)$$

and $r_0 = 2G_N^{(4)}M$.

Already we see that the topology of black holes can be much richer when $D > 4$. Solution (1.64) features an hyperspherical horizon whose topology is S^3 , whereas the black string (1.66) is topologically $\mathbb{R} \times S^2$, i.e. cylindrical. Moreover, the black string solution formally has infinite mass. To remedy this, we take the direction z to be compactified over a circle of length L such that we have a string of finite length and mass, in accordance to the principles of Kaluza-Klein theory.

Still, it is possible for these two solutions to have the same energy (in contrast with the uniqueness theorem that prevent this in the four-dimensional case), which prevents us from using the principle of least energy to determine which configuration is the likeliest. Instead we look at states of highest entropy. The entropy of a black object is related to the area A of its event horizon in Planck units via $S = A/4G_N$. At this point, an important subtlety of Kaluza-Klein theory needs to be taken into consideration. Compactifying extra dimensions always results in an effective change in Newton's constant, which we need to account for if we are to make sensible comparisons between the black hole and black string. Indeed, dimensional analysis of the gravitational constant in D dimensions reveals that

$$\left[G_N^{(D)} \right] = \text{length}^{D-2}. \quad (1.67)$$

In particular, we have $G_N^{(5)} = LG_N^{(4)}$. Thus the black hole (1.64) has entropy

$$S_{\text{BH}} = \frac{2\pi^2 r_5^3}{4G_N^{(5)}} = \frac{\pi^2 r_5^3}{2LG_N^{(4)}} \quad (1.68)$$

whereas the black string's (1.66) is

$$S_{\text{BS}} = \frac{4\pi r_0^2 L}{4G_N^{(5)}} = \frac{\pi r_0^2}{G_N^{(4)}}. \quad (1.69)$$

Assuming both configurations have the same mass M and setting $G_N^{(4)} = 1$ without loss of generality, we find

$$S_{\text{BH}} = \sqrt{\frac{8L}{27\pi M}} S_{\text{BS}}. \quad (1.70)$$

This thermodynamic argument shows that the black hole's entropy surpasses that of the string for large enough L , which suggests that the latter is subject to a long-wavelength instability. This instability has been investigated in the seminal papers [66, 67] by Gregory and Laflamme in which they solved the linearized Einstein equations numerically and confirmed the existence of a spectrum of exponentially growing modes near the horizon.

The perturbative nature of this calculation reveals information about the onset of the instability, yet it remains unclear what its endpoint should be. Simply put, there are two possible scenarios: deformation into a non-uniform black string (NUBS), or fragmentation of the event horizon. Arguments proposed in [68] claim that an event horizon can never classically pinch-off and should settle the critical string into a NUBS. However, computer simulations showed evidence to the contrary: the authors of [69] discovered that the late-time numerical evolution of the five-dimensional black string instability tended towards a fractal-like distribution of spherical black holes along ever-thinning string regions. The singularity therefore becomes “naked”, thus providing the first counter-example of a classical process that violates the cosmic censorship conjecture.

Whether quantum mechanical processes take over and prevent the un-cloaking of the singularity as the black string pinches off remains unknown to this day. However it was later discovered that the fate of the black string is more complex than previously thought as it depends on the number of spacetime dimensions [70]. Perturbative NUBS solutions close to the critical point of the instability were found to be thermodynamically favoured over

the critical string for $D > 13$, having both lower energy and higher entropy. In contrast, perturbative NUBS with $D \leq 13$ are too massive and not entropic enough in comparison to be the final state of the evolution, and the fragmentation scenario is still the most likely candidate of the black string’s (classical) fate.

In the large D formalism of general relativity, we thus expect the final state of the Gregory-Laflamme instability to be a NUBS at leading order [71]. In fact, the procedure of matched asymptotic expansions described in the previous section succeeded in reproducing the critical dimension $D = 13.5$ of the instability for neutral strings [72] as well as its spectrum to surprising accuracy [64]. In light of these results, there is hope that we can learn much more about brane instabilities analytically by performing a perturbative expansion in $1/D$ at subleading order, which is the topic of chapter 5.

1.3.4 Numerical Methods

Throughout this thesis, we will encounter various non-linear boundary value problems and systems of initial value ODEs that do not admit an analytic solution and therefore require a numerical approach. In this section, we discuss spectral methods for solving boundary value problems when the domain is bounded by regular singular points; we outline the celebrated Newton-Raphson root-finding algorithm to deal with non-linear equations; we introduce the characteristic formulation of general relativity, a framework particularly well-suited for the time-evolution of Einstein’s equations in the presence of a negative cosmological constant; finally, we present the Runge-Kutta-Fehlberg time-stepping algorithm of order 5, ideal for solving non-stiff initial value problems.

Spectral Methods

Due to its nature as a “confining box”, the equations of motion for matter fields in asymptotically AdS static spacetimes are classified as *elliptic* partial differential equations, which require the imposition of boundary conditions on the edges of the domain of dependence. The two radial boundaries, namely the AdS boundary and the horizon, are typically regular singular points of the differential equations around which finite differences method usually perform badly. Spectral methods, on the other hand, have special convergence properties not affected as much by such singularities.

Spectral methods assume that the solution to a differential equation can be approximated as a sum of Chebyshev polynomials $T_n(x)$ (well-suited for

non-periodic domains)

$$u(x) \approx u_N(x) = \sum_{n=0}^N \alpha_n T_n(x), \quad (1.71)$$

where the coefficients α_n are chosen such that the error made by using this approximation is minimized. However, in practice it is much simpler to work with a collocation grid $\{x_i\}_{i=0}^N$ and to find the unknowns $\{u(x_i)\}_{i=0}^N$ directly instead of solving the system of equations for the α_n . The two concepts are equivalent and can be related with the help of Lagrange interpolation, which we denote symbolically as

$$\{\alpha_n\}_{n=0}^N \iff \{u(x_i)\}_{i=0}^N. \quad (1.72)$$

It can be proven that Lagrange interpolation is optimal, i.e. that its Cauchy error

$$u(x) - u_N(x) = \frac{1}{(N+1)!} u^{(N+1)}(\xi) \prod_{i=0}^N (x - x_i) \quad (1.73)$$

is minimized, when the collocation points are chosen to be the maxima of $T_{N+1}(x)$

$$x_i = \cos\left(\frac{i\pi}{N}\right), \quad i = 0, \dots, N. \quad (1.74)$$

Notice how these points are denser near the endpoints $x = \pm 1$ than at the center, as shown in Figure 1.13. This non-uniform choice of grid turns out to cure the Runge phenomenon afflicting Lagrange interpolation with equidistant interpolation points. In fact, many of the important properties of spectral methods are a consequence of this non-uniform density of points, although the related proofs are beyond the scope of this section. The lesson to bear in mind however is that uniform discretization is in fact the worst choice one can make when it comes to numerical accuracy, and spectral methods offer an optimal alternative.

Now that we are in possession of a collocation grid, it is a straightforward task to define differentiation matrices acting on discretized functions \vec{u} with components $\{u(x_i)\}_{i=0}^N$. Indeed, the same way a centered difference approximation for first derivatives

$$u'(x) \approx \frac{u(x+h) - u(x-h)}{2h} \quad (1.75)$$

may be written in matrix form as $D \cdot \vec{u}$, where the components of D are

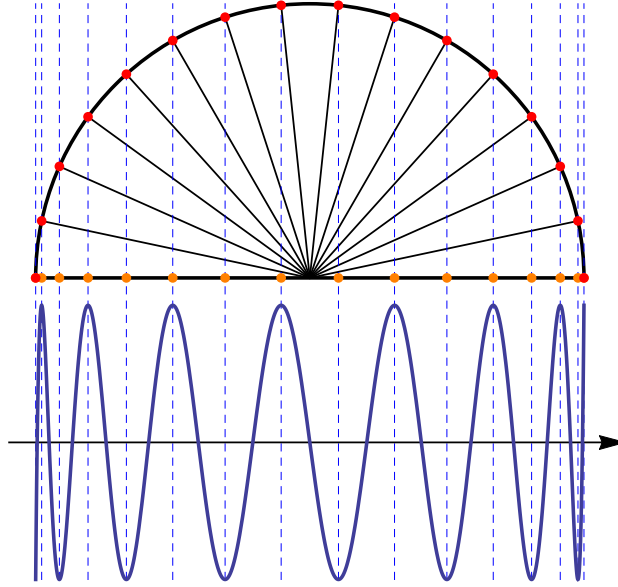


Figure 1.13: The maxima of $T_{N+1}(x)$ (shown at the bottom for $N = 15$) are uniformly distributed along the unit circle, which results in the boundary-dense grid $x_i = \cos(i\pi/N)$ when projected on the x -axis.

$D_{i,i\pm 1} = \pm 1/2h$ (with all other entries 0 if we assume periodicity), the spectral grid (1.74) leads to an $(N+1) \times (N+1)$ -dimensional differentiation matrix D_N whose components are

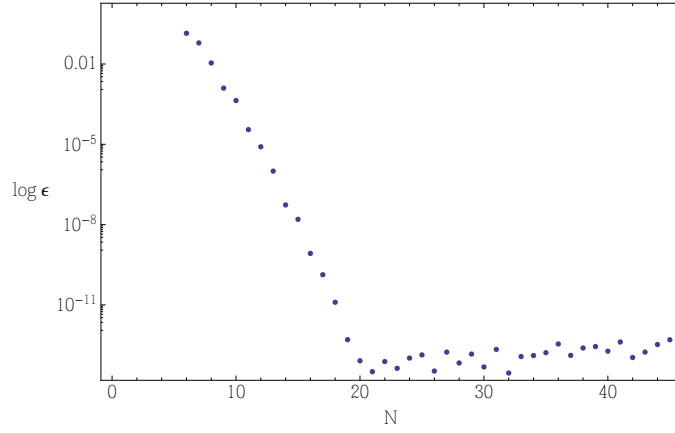
$$(D_N)_{00} = \frac{2N^2 + 1}{6}, \quad (D_N)_{NN} = -\frac{2N^2 + 1}{6} \quad (1.76)$$

$$(D_N)_{ii} = \frac{-x_i}{2(1 - x_i^2)}, \quad i = 1, \dots, N-1, \quad (1.77)$$

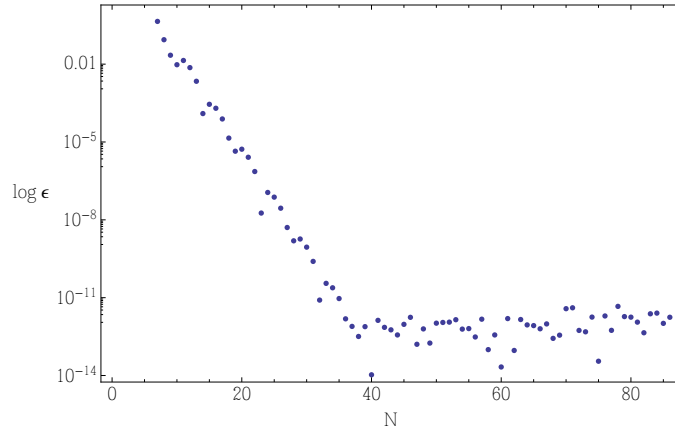
$$(D_N)_{ij} = \frac{c_i (-1)^{i-j}}{c_j x_i - x_j}, \quad i \neq j, \quad i, j = 1, \dots, N-1, \quad (1.78)$$

where $c_i = 2$ if $i = 0$ or N , and $c_i = 1$ otherwise.

D_N may be thought of as a global differentiation matrix in the sense that it uses the information at every grid point to compute each derivative $u'(x_i)$. This may result in poor accuracy when applied to non-analytic functions since local divergences may propagate and “infect” the derivative everywhere. However in practice spectral methods are most useful when smooth functions are involved. As a matter of fact, perhaps the most re-



(a) Numerical differentiation of $f(x) = e^{-x} \sin(\pi x)$.



(b) Numerical convergence of order parameter $\psi^{(2)}$ for $\mu = 9$.

Figure 1.14: The upper plot illustrates the spectral accuracy of numerical differentiation for a smooth function, with error measure $\epsilon_N = |f'(x) - D_N f|$. The lower plot shows the exponential convergence of the numerical solution of the holographic superconductor differential equation (1.35). The error measure in this case is $\epsilon_N = |\psi_N^{(2)} - \psi_{N-1}^{(2)}|$, the difference in the order parameter for successive values of N . In both cases machine precision prevents further improvements starting around $N = 20$ and $N = 40$ respectively.

markable property of these differentiation matrices is their *spectral accuracy*, the very rapid decrease of the error made from numerical differentiation as the grid size increases (illustrated in Figure 1.14). The convergence rate of spectral methods typically goes like $\mathcal{O}(N^{-m}) \forall m$ for smooth functions, and as fast as $\mathcal{O}(c^N)$ for $0 < c < 1$ for analytic functions. This is to be contrasted with the convergence rate of finite difference and finite element schemes, for which the error decreases like $\mathcal{O}(N^{-m})$ for a specific m depending on the order of approximation and smoothness of the function under consideration. As a result, spectral methods can reach an accuracy on the level of machine precision for moderate values of N , which make them very powerful when employed on modest desktop computers.

Newton-Raphson Method

The equations of general relativity are generally coupled and non-linear and often require a numerical approach. After discretizing differential equations on a collocation grid, they effectively become systems of algebraic equations for which many root-finding techniques already exist. The easiest and most widely used technique is the Newton-Raphson method, which we now proceed to describe.

Consider the algebraic system of equations

$$\mathbf{F}(\mathbf{u}) = \mathbf{0}, \tag{1.79}$$

which for our purposes includes both the discretized differential equation(s) and boundary conditions of interest. The Newton-Raphson method is an iterative process in which an initial guess is improved repeatedly until a convergence condition is met. For the sake of the argument, let's assume that $\mathbf{u} + \Delta\mathbf{u}$ is one of the solutions to (1.79), in which case

$$\mathbf{F}(\mathbf{u} + \Delta\mathbf{u}) = \mathbf{0} = \mathbf{F}(\mathbf{u}) + \mathbf{J}(\mathbf{u}) \cdot \Delta\mathbf{u} + \mathcal{O}(\Delta\mathbf{u})^2, \tag{1.80}$$

provided that the displacement $\Delta\mathbf{u}$ away from \mathbf{u} is small enough. Note that we have introduced the Jacobian matrix, whose components are given by

$$J_{ab} = \frac{\partial F_a}{\partial u_b}. \tag{1.81}$$

Equation (1.80) informs us about the optimal direction $\Delta\mathbf{u}$ towards a root. The Newton-Raphson algorithm simply turns the information contained in this displacement into an iterative process that works even if we are (mod-

erately) far away from a root, as each iteration takes us closer to a solution. Given an initial guess \mathbf{u}_0 , improved iterates are found according to

$$\mathbf{u}_{i+1} = \mathbf{u}_i - \mathbf{J}^{-1}(\mathbf{u}_i) \cdot \mathbf{F}(\mathbf{u}_i), \quad i \geq 0, \quad (1.82)$$

and progress is stopped when a root is found.

There are two ways to determine convergence. We may look at $|\mathbf{F}(\mathbf{u}_i)|$ directly, which should approach zero as the algorithm converge. It is also possible to monitor the norm of each individual displacement; if $|\mathbf{u}_{i+1} - \mathbf{u}_i| < \delta$ for a specified tolerance parameter δ , then successive iterates no longer change significantly and we conclude that convergence has been reached.

Convergence depends strongly on the guess provided initially; different initial guesses may converge towards different solutions. If so, we say that \mathbf{u}_0 is in the basin of convergence of a root. In practice, the choice of \mathbf{u}_0 is often informed by our physical intuition or our understanding of the problem at hand, with better choices resulting in a significant improvement in performance.

Despite its simplicity, this root-finding algorithm is very powerful. In the case of spectral methods, Newton-Raphson's quadratic convergence rate together with spectral accuracy add up to compensate for the cost of inverting a dense Jacobian, thus yielding an efficient way to solve coupled elliptic PDEs at high precision with modest computational resources.

Characteristic Formulation

Gauge theories with gravitational duals have been used in a wide array of applications so far, mostly in systems found in or near equilibrium. For instance, they have been most useful in extracting the transport coefficients of strongly interacting theories via linear response theory, and have also given rise to an hydrodynamic approach when studying their IR physics. The gauge/gravity duality also provides a framework making it possible to go beyond these limited regimes, enabling us to describe the far-from-equilibrium dynamics of quantum field theories by investigating gravitational infall in AdS. The most interesting problems usually involve the evolution of non-trivial inhomogeneous boundary conditions resulting in a non-static geometry, which in turn require the Einstein equations to be solved numerically in all their glory. As one would expect, this is no easy task; nevertheless framing the AdS initial value problem in a characteristic formulation allows for a systematic and stable approach to this problem, even in the absence of a high degree of symmetry.

The characteristic formulation of general relativity requires one to frame the gravitational infall problem in a coordinate system based on a null slicing of spacetime along infalling null geodesics. The resulting metric ansatz is a generalization of ingoing Eddington-Finkelstein coordinates

$$ds^2 = \frac{r^2}{L^2} g_{\mu\nu}(x, r) dx^\mu dx^\nu - 2 \omega_\mu(x) dx^\mu dr. \quad (1.83)$$

In the above r is a radial coordinate such that the AdS boundary is located at $r = \infty$, $\{x^\mu\}$ denote the d boundary coordinates where $t = x^0$ is a null time coordinate in the bulk which coincides with field theory time at $r = \infty$, and the vector ω^μ is assumed to be timelike and physically represents fluid flow on the boundary. This is indeed a null slicing of spacetime since keeping all coordinates but r fixed results in $ds^2 = 0$, and we say that ∂_r is a directional derivative along infalling null geodesics.

The metric (1.83) restricts diffeomorphism invariance by allowing only two types of residual diffeomorphisms, which are easily fixed. The metric is invariant under d -dimensional changes of coordinates as well as under radial shifts

$$x^\mu \rightarrow \bar{x}^\mu = f(x^\mu), \quad (1.84)$$

$$r \rightarrow \bar{r} = r + \lambda(x). \quad (1.85)$$

The former can be used to set $\omega_\mu(x) = -\delta_\mu^0$, whereas the latter can be used to gauge-fix the *apparent* horizon's location⁷. This is important because gravitational infall problems involve excitations falling into a black hole, thus creating ripples on the horizon such that its location varies in time and space: $r_h = r_h(t, \mathbf{x})$. The radial shift field $\lambda(x)$ encodes the dependence on x of these deformations, and gauge-fixing radial diffeomorphisms lets us lock the IR boundary of the radial domain in place throughout the time-evolution. Doing so not only eases numerical implementation since the computational domain of the Einstein equations remains fixed in size, but also lets us avoid stability issues by excising the unphysical region behind the horizon.

The ansatz (1.83) provides suitable coordinates throughout the domain as long as coordinate singularities do not develop in the bulk, and provided the apparent horizon remains planar. On one hand gravity's attractive nature may result in the focusing and intersection of infalling radial geodesics,

⁷The event horizon of a black hole depends on the full history – including both past and future – of the spacetime geometry and as such cannot be determined locally, but the apparent horizon can. See Appendix A for details.

a phenomenon called *caustic* formation. Caustics are coordinate singularities for which an event (x, r) is not uniquely determined anymore, and the null foliation of spacetime breaks down. As a result, the ansatz (1.83) in the presence of caustics requires different coordinate patches for different regions in order to preserve regularity. On the other hand apparent horizons are defined as the boundary of trapped outgoing null geodesic congruences. If such a compact trapped surface formed inside the bulk, it would invalidate the global regularity of our ansatz and potentially lead to caustic formation as well. As shown in Figure 1.15, it is possible to cure these singularities in both cases simply by increasing the IR cutoff in a way such that the caustics form behind it, at the cost of losing information on low-energy physics on the boundary. Thankfully such pathologies do not arise often, if at all, in practice.

Let us now turn our attention to the special structure of Einstein's equations under the metric ansatz (1.83), which we may rewrite as

$$ds^2 = G_{ij}(X)dx^i dx^j + 2dt [dr - E_\mu(X)dx^\mu], \quad E_\mu = (A, F_i), \quad (1.86)$$

where $X = (r, t, x^i)$ denotes all bulk coordinates. Under radial shifts (1.85), the components of E_μ transform as a gauge field

$$E_\mu(r, x) \rightarrow \bar{E}_\mu(x, \bar{r}) = E_\mu(x, \bar{r} - \lambda) + \partial_\mu \lambda(x). \quad (1.87)$$

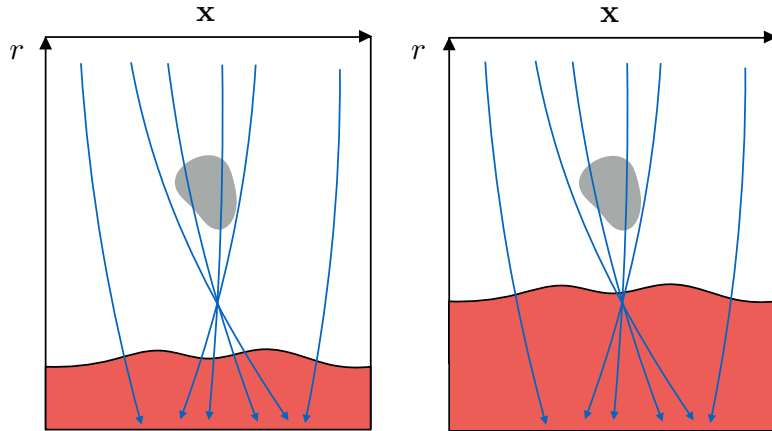
It is natural to implement this gauge invariance in the Einstein equations by defining the derivatives

$$d_+ = \partial_t + A(X)\partial_r, \quad (1.88a)$$

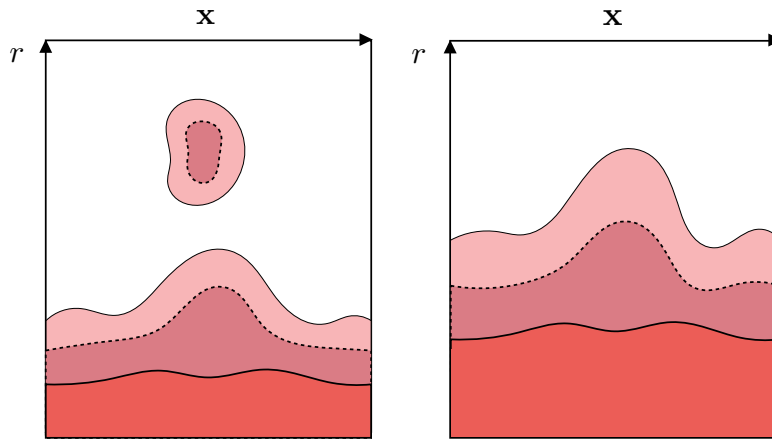
$$d_i = \partial_i + F_i(X)\partial_r, \quad (1.88b)$$

which transform covariantly under radial shifts and d -dimensional diffeomorphisms. The modified temporal derivative (1.88a) is a directional derivative along outgoing null geodesics, whereas (1.88b) has an analogous geometrical interpretation as a derivative along spacelike directions orthogonal to ingoing and outgoing radial null geodesics.

An extensive analysis reveals that rewriting the Einstein field equations in terms of the new time derivative d_+ effectively separates them into two classes. The first contains radial equations for auxiliary fields, which can be solved *sequentially* on each $t = \text{constant}$ slice, whereas the second contains the dynamical equations that let us evolve the geometry from one null time slice to the next. This distinction however is not unique and different choices



(a) On the left: the region of spacetime coloured in grey focuses infalling geodesics (in blue), leading to caustic formation in the bulk. On the right: the caustics form behind the apparent horizon (in red).



(b) On the left: a compact trapped surface discontinuously develops in the bulk. On the right: the apparent horizon maintains its planar topology. Note: lighter shades correspond to later times.

Figure 1.15: These figures, adapted from [73], illustrate the two types of pathologies leading to the breakdown of the characteristic formulation.

result in different schemes of variable stability. Nonetheless, the sequential nature of the different equations involved is what makes the characteristic formulation powerful. Expressing the field equations in terms of ingoing and outgoing null vectors, namely ∂_r and d_+ , allows the repackaging of their nonlinearities in a sorted sequence of radial ODEs easily handled by spectral methods.

All we need to complete our discussion is a set of initial conditions that encode the phenomenon of interest. Initial conditions for this type of gravitational infall problem in AdS_{d+1} are provided partly from the particular details of the modelization and partly from boundary data, namely from the boundary stress tensor. In particular, the asymptotic behaviour of the spatial part G_{ij} of the metric (1.86) ultimately determine the initial state of the system (e.g. anisotropy, shape of colliding shockwaves, etc.) whereas A and F_i fix the energy and momentum densities of the field theory and need to be specified on each time slice. To extract this information, we first rewrite the metric in Fefferman-Graham form

$$ds^2 = \frac{L^2}{\rho^2} (g_{\mu\nu}(x, \rho) dx^\mu dx^\nu + d\rho^2) \quad (1.89)$$

with

$$g_{\mu\nu}(x, \rho \rightarrow 0) \sim \eta_{\mu\nu} + \sum_{n=d}^{\infty} g_{\mu\nu}^{(n)}(x) \rho^n. \quad (1.90)$$

In these coordinates, holographic renormalization tells us that part of the metric at order d remains undetermined by the equations of motion and requires additional information from the CFT via the identification (up to a normalizing constant)

$$\langle T_{\mu\nu}(x) \rangle \sim g_{\mu\nu}^{(d)}(x), \quad (1.91)$$

plus possible additions depending on the matter content of the theory [12, 13]. With this information put in by hand, the evolution scheme can then be implemented straightforwardly due to its sequential nature. We have found that the Runge-Kutta-Fehlberg time-stepping algorithm of order 5 was particularly useful in evolving the geometry along null time. As such it is the topic of the following section.

Runge-Kutta-Fehlberg with Adaptive Step Size

The Runge-Kutta (RK) methods are powerful explicit time-stepping algorithms useful in solving initial value differential equations of the form

$$\frac{dy}{dt} = f(t, y); \quad y(t_0) = y_0. \quad (1.92)$$

The key idea behind RK-type algorithms is to express the solution $y(t)$ in terms of derivative terms $f(t, y)$ sampled at many intermediate values in a way that minimizes truncation error. The standard, most used method is by far the fourth-order method known as RK4, which uses the time-evolution scheme

$$y(t_0 + h) = y(t_0) + \frac{h}{6} (f_1 + 2f_2 + 2f_3 + f_4), \quad (1.93)$$

where

$$\begin{aligned} f_1 &= f(t_0, y_0); \\ f_2 &= f\left(t_0 + \frac{h}{2}, y_0 + \frac{h}{2}f_1\right); \\ f_3 &= f\left(t_0 + \frac{h}{2}, y_0 + \frac{h}{2}f_2\right); \\ f_4 &= f(t_0 + h, y_0 + hf_3). \end{aligned} \quad (1.94)$$

This algorithm performs wonderfully in many cases, but keeping the step size h fixed may be inefficient. Consider for instance a solution with both slow- and fast-changing regions. If one were to employ RK4 to solve the corresponding differential equation, one would have to set h equal to the smallest numerical resolution required in regions of most rapid variations to maintain accuracy throughout the domain. Doing so may prove wasteful in better-behaved regions, where a larger step size would yield an equally satisfying error.

The easiest way to resolve this issue would be to compute the solution twice with step sizes h and $h/2$, and then evaluate the difference as a measure of the error. However this comparison involves twice the amount of computational work and is thus an inefficient solution to our efficiency problem. The insight of Fehlberg was to realize that the fourth- and fifth-order RK methods both use the same intermediate function evaluations $f(t, y)$, but

weighted differently. They are given respectively by

$$y^{(4)}(t_0 + h) = y_0 + h \vec{b}_i^{(4)} \cdot \vec{f}, \quad \vec{b}^{(4)} = \left(\frac{25}{216}, 0, \frac{1408}{2565}, \frac{2197}{4104}, -\frac{1}{5}, 0 \right), \quad (1.95)$$

$$y^{(5)}(t_0 + h) = y_0 + h \vec{b}_i^{(5)} \cdot \vec{f}, \quad \vec{b}^{(5)} = \left(\frac{16}{135}, 0, \frac{6656}{12825}, \frac{28561}{56430}, -\frac{9}{50}, \frac{2}{55} \right), \quad (1.96)$$

in which the function samples are sequentially given via

$$f_i = f \left(t_0 + c_i h, y_0 + h \sum_{j=1}^6 a_{ij} f_j \right), \quad 1 \leq i \leq 6 \quad (1.97)$$

with

$$\vec{c} = \left(0, \frac{1}{4}, \frac{3}{8}, \frac{12}{13}, 1, \frac{1}{2} \right) \quad (1.98)$$

and

$$a = \begin{pmatrix} 0 & 0 & 0 & 0 & 0 & 0 \\ \frac{1}{4} & 0 & 0 & 0 & 0 & 0 \\ \frac{3}{8} & \frac{9}{32} & 0 & 0 & 0 & 0 \\ \frac{1932}{2197} & -\frac{7200}{2197} & \frac{7296}{2197} & 0 & 0 & 0 \\ \frac{439}{216} & -8 & \frac{3680}{513} & -\frac{845}{4104} & 0 & 0 \\ -\frac{8}{27} & 2 & -\frac{3544}{2565} & \frac{1859}{4104} & -\frac{11}{40} & 0 \end{pmatrix}. \quad (1.99)$$

The error can then be evaluated by taking the difference between the two approximations

$$\mathcal{E} = |y^{(5)} - y^{(4)}| = h |\vec{r} \cdot \vec{f}|, \quad \vec{r} = \left(\frac{1}{360}, 0, -\frac{128}{4275}, -\frac{2197}{75240}, \frac{1}{50}, \frac{2}{55} \right). \quad (1.100)$$

Our last task is to determine a condition for the step size to continuously adapt to our error tolerance. The truncation error of the difference between fourth- and fifth-order RK methods is

$$|y^{(5)} - y^{(4)}| \approx Mh^5 \quad (1.101)$$

for some constant M . If we denote ϵ as our tolerance in the derivative's error, then the function itself must have an error $\mathcal{E} \sim h\epsilon$. We can then find an optimal step size \bar{h} that sets the truncation error to be equal to the

prescribed tolerance by imposing the condition

$$\bar{h}\epsilon = M\bar{h}^5 = \frac{\bar{h}^5}{h^5}\mathcal{E} \quad (1.102)$$

and therefore obtain the improved step size

$$\bar{h} = h \sqrt[4]{\frac{\epsilon}{|\vec{r} \cdot \vec{f}|}}. \quad (1.103)$$

If the calculated error \mathcal{E} is higher than the tolerance, then we deduce that $h > \bar{h}$ and a smaller step size is required. The prior step then needs to be rejected and calculated anew with $h_{\text{new}} < h$. Conversely, if the calculated error is lower than the tolerance, then it is possible to take larger steps without any penalty. In that case \bar{h} offers a good estimate of the next iteration's step size. As a result, the time-stepping algorithm is always adjusting h in a way that optimizes both resources and errors.

Chapter 2

Chiral Edge Currents in a Holographic Josephson Junction

We discuss the Josephson effect and the appearance of dissipationless edge currents in a holographic Josephson junction configuration involving a chiral, time-reversal breaking superconductor in 2+1 dimensions. Such a superconductor is expected to be topological, thereby supporting topologically protected gapless Majorana-Weyl edge modes. Such modes can manifest themselves in chiral dissipationless edge currents, which we exhibit and investigate in the context of our construction. The physics of the Josephson current itself, though expected to be unconventional in some non-equilibrium settings, is shown to be conventional in our setup which takes place in thermal equilibrium. We comment on various ways in which the expected Majorana nature of the edge excitations, and relatedly the unconventional nature of topological Josephson junctions, can be verified in the holographic context.

2.1 Introduction and Summary

The physics of topological insulators and superconductors has become a central topic in modern condensed matter physics (for reviews see [74, 75]). Many of the interesting phenomena exhibited in such materials follow from the existence of topologically protected gapless edge modes. For topological superconductors, these are expected to be chiral Majorana modes. The search for such Majorana excitations in various condensed matter systems is currently an intense experimental effort (for a review see [76]).

Topological superconductivity is expected to arise in time-reversal breaking superconductors, with a “p+ip” order parameter symmetry, which we refer to here as chiral superconductors. Experimentally, such topological superconductivity might arise intrinsically, for example in the Strontium Ruthenate Sr_2RuO_4 (see e.g. [29, 30] for reviews), or by proximity effect (following the suggestion of Fu and Kane [77]). That system was analyzed by Green and Read [78], who demonstrated the existence of Majorana-Weyl fermions propagating on the edges of a two-dimensional chiral superconduc-

tor¹. A particularly clear construction of the edge modes as Andreev bound states can be found in [80].

In this note we use the tools of gauge-gravity duality to investigate the topological nature of the holographic superconductor. As we will see, the manifestation of topology comes in the form of chiral edge excitations which manifest themselves as chiral currents localized at edges of the superconductor. To this end, we construct a gravity solution that exhibits the basic phenomena associated with topological superconductivity, namely topologically protected edge modes and spontaneously generated edge currents. Indeed, after the observation of [20] that black holes can be unstable to scalar condensation, an s-wave superconductor was constructed in [22]. Holographic duals to p-wave superconductors were constructed in [27], and the model we are using here, an holographic dual to a chiral superconductor, was constructed in [81]. We review that construction in section 2 below².

Since much of the new interesting physics associated with topological superconductivity has to do with edges and interfaces, we construct a Josephson junction involving the holographic chiral superconductor. Holographic Josephson junctions were constructed first in [33] (see also [82–84] for other configurations). Our work will focus on building an S-N-S holographic Josephson junction for the holographic chiral superconductor (S) for which the weak link is a normal metal (N). The construction of the gravity solution involves the numerical solution of a set of partial differential equations, details of which are presented in section 2.

One of the dramatic manifestations of the topologically protected gapless modes are spontaneously generated dissipationless currents, localized at the edges of a topological superconductor. The relation between the edge currents, edge states and gauge invariance is explained in [80]. Since Josephson junctions involve two such interfaces between topological and non-topological materials, we expect to find counter-propagating currents, one on each interface. Such currents are clearly visible in our setting and we discuss their features in section 3 below. We find that up to small corrections, the strength of the edge currents is determined by the jump of the order parameter amplitude across the interface between the superconducting

¹See however [79] for a recent null experimental result in Sr_2RuO_4 .

²The model we discuss here supports competing orders, indeed the p-wave order parameter [27] is thermodynamically preferred in this model. Our Josephson junction is therefore an idealized configuration, but is nevertheless an interesting probe of the time-reversal breaking holographic superconductor. We expect that the features we uncover here, to do with topological structures, are insensitive to the phase structure of the full model.

material and the weak link.

The counter-propagating edge currents we observe are independent of each other (for wide enough junctions), and would exist for a single isolated interface as well. They are indicative of chiral gapless edge modes localized on such interfaces³. The full Josephson junction has a pair of these modes, a feature which is speculated to be responsible for some unusual properties of the topological Josephson junction. Therefore, in section 4 we turn to examine the Josephson current in our junction.

Anomalies in the current-phase relation in such “unconventional” Josephson junctions were reported in [85], but a more recent direct measurement reveals a conventional relation [86]. While the physics of such junction is expected to be unconventional, in that it is 4π periodic in the phase across the weak link [87], equilibrium configurations might still exhibit the conventional 2π periodicity. Other attempts to discover unconventional periodicity as a signature of the aforementioned pair of Majorana bound states include the AC Josephson effect [88], Josephson junctions in magnetic fields [89], current noise measurements [90] or unconventional Shapiro steps [91].

In section 4 we exhibit the details of the Josephson effect in our holographic construction. We find conventional results, fairly similar to the s-wave case reported in [33]. The current-phase relation is 2π periodic and the maximal current decays exponentially as the width of the junction increases (as opposed to the power law decay observed in [85]). Furthermore, the temperature dependence of the critical current and the coherence length are also found to be fairly conventional. We conclude that our setup, which takes place in thermal equilibrium, is thus insensitive to the unconventional features expected to arise from the presence of gapless Majorana modes.

We conclude in section 5 with outlook and directions for future work. In particular, we outline some calculations that would verify the existence of gapless Majorana modes and exhibit the expected doubled periodicity of the physics in the Josephson junction. We hope to report on such results in the near future.

2.2 Setup and Solutions

Our discussion of the time-reversal breaking holographic superconductor [81] follows the conventions of [28]. Let us consider the following action:

³For the existence of a charge current, at least two Majorana-Weyl fermions are required.

$$S = \int d^4x \sqrt{-g} \left[R + \frac{6}{L^2} - \frac{1}{4g^2} (F_{\mu\nu}^a)^2 \right] \quad (2.1)$$

where $F_{\mu\nu}^a = \partial_\mu A_\nu^a - \partial_\nu A_\mu^a + \epsilon^{abc} A_\mu^b A_\nu^c$ is the field strength tensor for an $SU(2)$ gauge field, and ϵ^{abc} is the totally antisymmetric tensor, with $\epsilon^{123} = 1$. The gauge field can be conveniently expressed as a matrix-valued one form: $A = A_\mu^a \tau^a dx^\mu$, where $\tau^a = \sigma^a/2i$, σ^a being the usual Pauli matrices. It follows that $[\tau^a, \tau^b] = \epsilon^{abc} \tau^c$.

We will be working in the probe approximation, thereby neglecting the backreaction of the gauge field on the metric. In the current model, the probe approximation, controlled by the ratio of the Newton's constant to the gauge coupling, breaks down at sufficiently low temperatures. However, though adding backreaction should be straightforward, this is unnecessary for the effects we are interested in, and we will restrict ourselves to working in a fixed gravitational background.

Specifically, we choose the metric to be the asymptotically AdS_4 planar Schwarzschild black hole: and L and r_0 are the AdS and horizon radii, respectively. Such a black hole has Hawking temperature

$$T = \frac{1}{4\pi} \left. \frac{dh}{dr} \right|_{r=r_0} = \frac{3r_0}{4\pi L^2} \quad (2.2)$$

Scaling symmetries further enable us to work in units in which $L = 1$ and set $r_0 = 1$. This corresponds to measuring all dimensional quantities in units of temperature.

To understand the symmetry structure of our ansatz, it is useful to define complex coordinates

$$\zeta = \frac{x + iy}{\sqrt{2}} \quad \text{and} \quad \tau^\pm = \frac{\tau^1 \pm i\tau^2}{\sqrt{2}} \quad (2.3)$$

The ansatz for the spatially homogeneous $p + ip$ superconductor is given by [28, 81]

$$A = \Phi \tau^3 dt + w \tau^- d\zeta + w^* \tau^+ d\bar{\zeta} \quad (2.4)$$

Here Φ breaks the $SU(2)$ symmetry explicitly to an Abelian subgroup at the short distance scale of the chemical potential μ , and w is the order parameter which breaks the $U(1)$ symmetry spontaneously at a much longer distance scale. Note that in these conventions a $U(1)$ gauge transformation is a phase rotation of the complex order parameter w . In the homogeneous case w can be chosen to be everywhere real, but with inhomogeneities this is no longer

the case. In particular the phase difference across the Josephson junction is an interesting gauge-invariant quantity directly responsible for driving the Josephson current.

The order parameter w is invariant under a combination of spatial rotations and gauge transformations, thus the superconductor is isotropic. Since w is complex, time-reversal is broken spontaneously. As we see below, this has interesting consequences for the physics probed by the Josephson junction in this system.

In order to build a holographic Josephson junction, the fields must have spatial dependence. We model a Josephson junction by choosing an appropriate profile for the chemical potential $\mu(x)$, as described below. The fields then all depend on the spatial coordinate x and the radial coordinate r . Our ansatz for a $p + ip$ Josephson junction is then

$$A = \Phi \tau^3 dt + w \tau^- d\zeta + w^* \tau^+ d\bar{\zeta} + A_x \tau^3 dx + M_y \tau^3 dy + A_r \tau^3 dr \quad (2.5)$$

We are using a somewhat mixed notation for the spatial directions, where the chiral nature of the order parameter is most clearly exhibited using the ζ coordinate defined in (2.3). Note the presence of the field M_y which, unlike other instances of holographic Josephson junctions, cannot be eliminated using symmetries. This field will encode the presence of dissipationless edge currents, which we discuss below.

Following [33] we choose to work in terms of gauge invariant combinations. If $w = |w|e^{i\theta}$, those are $w \equiv |w|$, M_y and $M_\mu = A_\mu - \partial_\mu \theta$ for $\mu = x, r$. Our ansatz yields the following system of 5 coupled non-linear elliptic PDEs,

$$\begin{aligned} \partial_r^2 \Phi + \frac{2}{r} \partial_r \Phi + \frac{\partial_x^2 \Phi}{r^2 h} - \frac{2w^2 \Phi}{r^2 h} &= 0 \\ \partial_r^2 w + \frac{h'}{h} \partial_r w + \frac{\partial_x^2 w}{2r^2 h} - \frac{3w \partial_x M_y}{2r^2 h} + \frac{w \Phi^2}{h^2} - \frac{w^3}{r^2 h} - \frac{(M_x^2 + M_y^2)w}{2r^2 h} - M_r^2 w &= 0 \\ \partial_r^2 M_x + \frac{h'}{h} (\partial_r M_x - \partial_x M_r) - \partial_r \partial_x M_r - \frac{M_x w^2}{r^2 h} &= 0 \\ \partial_r^2 M_y + \frac{h'}{h} \partial_r M_x + \frac{\partial_x^2 M_y}{r^2 h} + \frac{3 \partial_x (w^2)}{2r^2 h} - \frac{M_y w^2}{r^2 h} &= 0 \\ \partial_x^2 M_r - \partial_r \partial_x M_x - 2M_r w^2 &= 0 \end{aligned} \quad (2.6)$$

and an additional constraint:

$$\partial_r (hM_r w^2) + \frac{1}{2r^2} \partial_x (w^2 M_x) = 0 \quad (2.7)$$

We thus need to choose boundary conditions such that the constraint is satisfied at the boundaries of the integration domain.

Next we discuss the boundary conditions satisfied by our fields. The boundary conditions at the horizon are determined by requiring regularity and satisfying the constraint. That is, when expanding the equations of motion and constraint near the horizon, divergent terms arise which we require to cancel. At the spatial boundaries we impose Neumann boundary conditions on all fields. Near conformal infinity the fields behave asymptotically as

$$\begin{aligned} \Phi(r, x) &= \mu(x) - \frac{\rho(x)}{r} + \dots \\ w(r, x) &= w^{(1)}(x) + \frac{w^{(2)}(x)}{r} + \dots \\ M_x(r, x) &= v_x(x) + \frac{J_x}{r} + \dots \\ M_y(r, x) &= v_y(x) + \frac{J_y(x)}{r} + \dots \\ M_r(r, x) &= O\left(\frac{1}{r^3}\right) \end{aligned}$$

We will input $\mu(x)$ to model a Josephson junction, and choose the condensate w to be normalizable, $w^{(1)}(x) = 0$. The current in the x-direction J_x is constant by the continuity equation and we choose it to be one of the parameters of our solutions. The conjugate quantity $v_x(x)$ is then read from the solution and encodes the phase difference across the junction. Finally, we set $v_y(x) = 0$ as there is no applied voltage in the transverse direction y , and read off the spontaneously generated transverse current $J_y(x)$ from the solution.

To model a Josephson junction we need to choose the profile $\mu(x)$ appropriately. In the case of homogeneous superconductors, the scale invariant quantity to consider is T/μ , i.e. changing the temperature is equivalent to changing μ . This is no longer the case in the spatially inhomogeneous case: while our chemical potential is spatially varying, the temperature is still constant. Instead, to measure the temperature in a scale invariant way we use the scale invariant quantity T/T_c , where the critical temperature

T_c is proportional to $\mu_\infty \equiv \mu(\infty)$. Our simulations set the proportionality relation to be

$$T_c \approx 0.065 \mu_\infty \quad (2.8)$$

Since we now change the temperature by varying μ , there is a corresponding critical chemical potential μ_c below which the condensate vanishes. We thus need a profile with the following features:

$$\begin{cases} \mu(x) < \mu_c & \text{in the normal metal phase, } -\frac{\ell}{2} < x < \frac{\ell}{2}; \\ \mu(x) > \mu_c & \text{otherwise for the superconducting phases.} \end{cases}$$

As in [33], a profile that satisfies these conditions is

$$\mu(x) = \mu_\infty \left[1 - \frac{1 - \epsilon}{2 \tanh(\frac{\ell}{2\sigma})} \left\{ \tanh\left(\frac{x + \frac{\ell}{2}}{\sigma}\right) - \tanh\left(\frac{x - \frac{\ell}{2}}{\sigma}\right) \right\} \right] \quad (2.9)$$

where $\mu_\infty > \mu_c$ is the maximal height of the chemical potential. The parameter σ controls the steepness of the profile, whereas ϵ controls its depth – the chemical potential inside of the normal phase is typically $\mu_0 \equiv \epsilon\mu_\infty$. Moreover, it is convenient to work with compactified variables $z = 1/r$ and $\bar{x} = \tanh(\frac{x}{4\sigma}) / \tanh(\frac{p}{4\sigma})$, where p is the length of the x -direction.

Pseudo-spectral collocation methods on a Chebyshev grid were used to discretize the above equations. The resulting equations were solved using the Newton iterative method. One key characteristic of the pseudo-spectral methods is their exponential convergence in the size of the grid used, which we have confirmed explicitly for our solutions. The solutions used in this paper were produced using a grid of 41 points in both the radial and spatial direction, yielding an estimated maximal error of about 10^{-4} in the local value of all functions.

2.3 Chiral Edge Currents

We start by discussing the phenomenon unique to the time-reversal breaking chiral superconductor: the existence of edge currents. The existence of dissipationless chiral edge currents is indicative of gapless chiral modes living on an interface between the superconductor and the normal state. In a Josephson junction configuration there are two such interfaces and therefore two independent counter-propagating modes. In this section we focus on aspects of these modes that are localized at each interface separately, which would exist in a simpler domain wall geometry. In the next section we

turn to discuss aspects of the physics more specific to a Josephson junction configuration with two such interfaces.

To be more concrete, the introduction of a gauge field M_y^3 makes it possible to measure a current $J_y(x)$ propagating in the y-direction. We have specified $M_y^3(r = \infty, x) = 0$ so that the system has no applied voltage that would drive a current in the y-direction, thus this is a dissipationless current flowing without resistance. Under such conditions, the field M_y^3 would vanish everywhere for a p -wave order parameter, but has a non-trivial profile in the $p + ip$ case. As shown in figure 2.1, this current is localized at the interfaces of the superconducting and normal phases, travelling in opposite directions with equal magnitude. We have checked that the strength of the current is independent of the Josephson phase (or equivalently, the strength of the Josephson current) and the width of the junction (for sufficiently wide junctions). Therefore the currents on both interfaces are local effects independent of each other.

The quantity of interest is the total current per unit area, defined as follows:

$$J_{\text{edge}} \equiv \int_0^\infty J_y(x) dx \quad (2.10)$$

We focus on this quantity as it is independent of details of the interface profile such as the steepness, parametrized by σ above. Furthermore, we find that the edge current is essentially constant when the weak link is a normal metal, independent of the relative depth parameter ϵ . However, when the weak link becomes superconducting, the current decreases as we increase ϵ ,

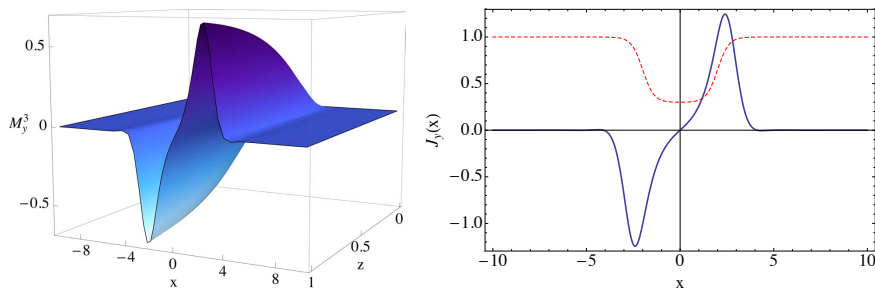


Figure 2.1: The left plot displays the solution for the gauge field M_y^3 . The right plot shows the resulting boundary current $J_y(x)$ (in blue), as well as the rescaled chemical potential profile $\mu(x)/\mu_\infty$ (in red). The solution corresponds to $\mu_\infty = 7$, $\ell = 4$, $\sigma = 0.6$ and $\epsilon = 0.3$.

eventually vanishing when the solution is perfectly homogeneous.

This dependence on the relative depth is shown in Figure 2.2. It indicates that the current is controlled by the jump in the amplitude of the order parameter across the interface between the superconducting material and the weak link. Indeed, in Figure 2.3 we plot the dependence on the edge current on the order parameter in the superconducting phase $\langle \mathcal{O}_S \rangle$ (choosing ϵ such that the weak link is always at the normal state, i.e. has approximately zero condensate). The edge current depends on the magnitude of the order parameter through a power law relationship $J_{\text{edge}} \sim \langle \mathcal{O}_S \rangle^\alpha$ with α ranging between 2.04 and 2.12 for different choices of parameters.

It is also natural to examine the temperature dependence of the edge current, which we plot in Figure 2.4. We see that the dominant change in the edge current as we change the temperature comes through the change in the amplitude of the order parameter. As expected the edge current vanishes at the critical temperature T_c .

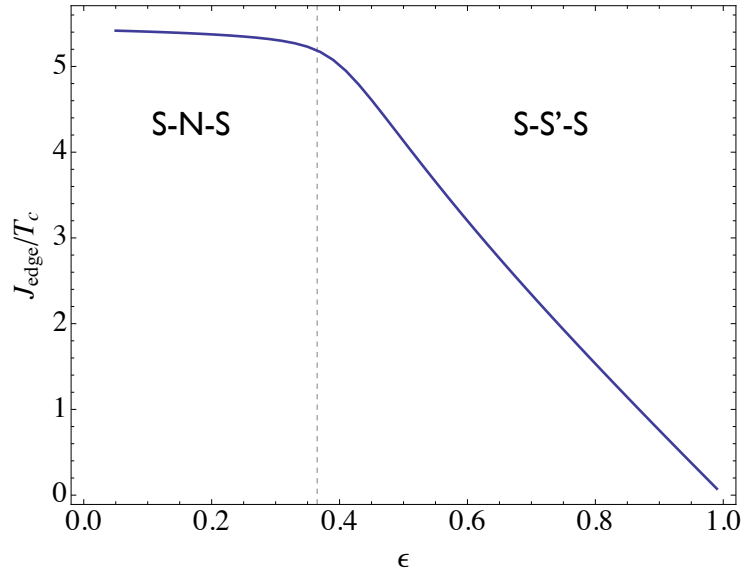


Figure 2.2: The data above corresponds to $\mu_\infty = 10$. As we increase the depth ϵ , we observe a linear decrease in the edge current value happening around the dashed line at $\epsilon_c = \mu_c/\mu$, which is the critical depth at which the weak link becomes superconducting. At $\epsilon = 1$, J_{edge} goes to 0 since $\mu(x)$ becomes homogeneous.

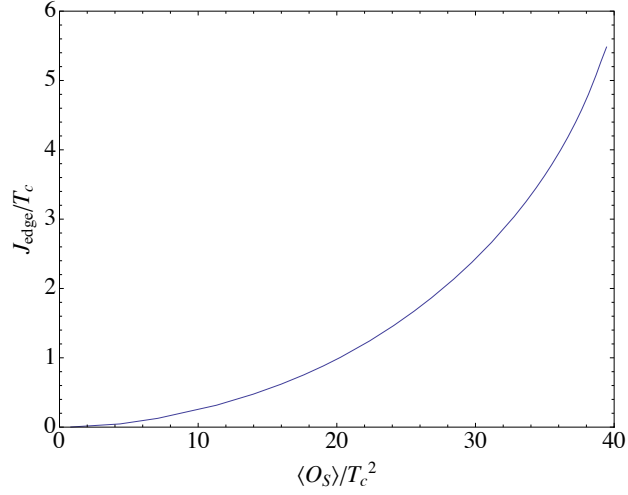


Figure 2.3: This plot illustrates the dependence of the edge current on the amplitude of the order parameter in the superconducting phase for $\ell = 4$, $\sigma = 0.6$ and $\epsilon = 0.3$. The curve fits $J_{\text{edge}} \sim \langle O_S \rangle^\alpha$ with $\alpha \simeq 2$.

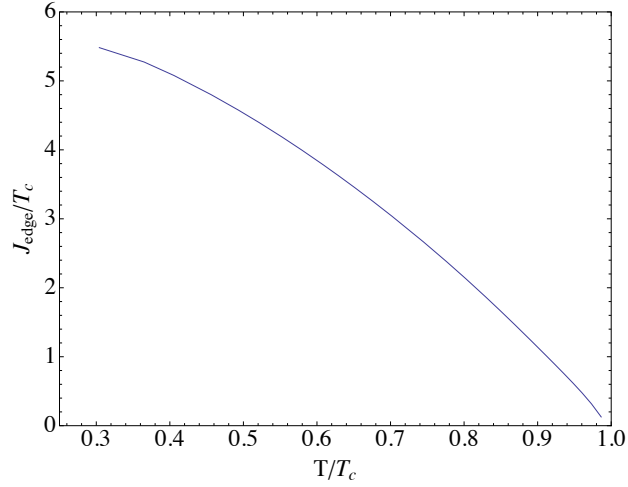


Figure 2.4: The temperature dependence of the edge current is pictured for $\ell = 4$, $\sigma = 0.6$ and $\epsilon = 0.3$.

2.4 Josephson Currents

The Josephson effect is a macroscopic quantum phenomenon in which a dissipationless current flows across a weak link between two superconducting

electrodes, in the absence of an external applied voltage. Rather, it is the gauge invariant phase difference across the junction that is responsible for the current. Following [33], we will consider S-N-S Josephson junctions, for which the weak link is a non-superconducting (“normal”) metal, as described above. We also make some comments on the S-S'-S case, in which the weak link is superconducting. For a discussion of an S-I-S weak link, see [84].

The Josephson current flowing across the junction has the expected form

$$J_x = J_{\max} \sin \gamma \quad (2.11)$$

where the gauge invariant phase difference across the junction is obtained from the solution as

$$\gamma = - \int_{-\infty}^{\infty} dx [v_x(x) - v_x(\pm\infty)] \quad (2.12)$$

Figure 2.5 has been obtained by computing γ for multiple solutions corresponding to different inputs J_x ; it clearly demonstrates the expected dependence of the Josephson current on the phase difference.

Another interesting feature of the critical current J_{\max} is that it decays

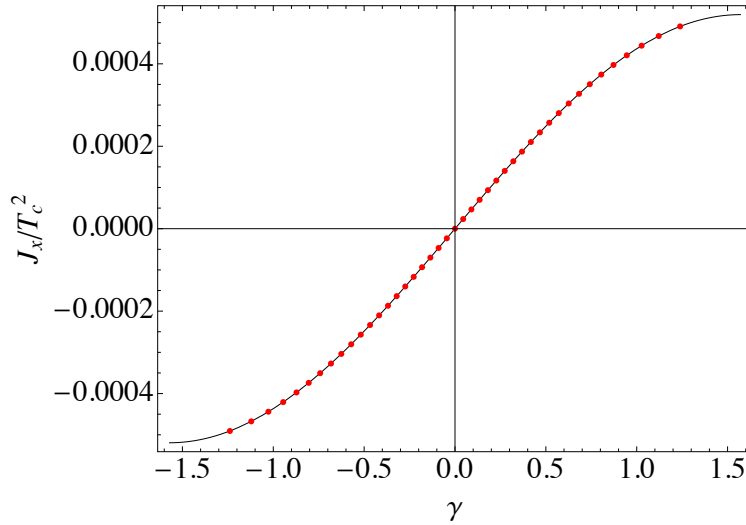


Figure 2.5: This graph, produced with $\mu_\infty = 10$, $\ell = 4$, $\sigma = 0.4$ and $\epsilon = 0.05$, shows the agreement of our data with the expectation (2.11). The solid line, describing the best fit curve to our data (in red), is the curve $J_x = 5.2 \times 10^{-4} \sin(0.9986\gamma)$.

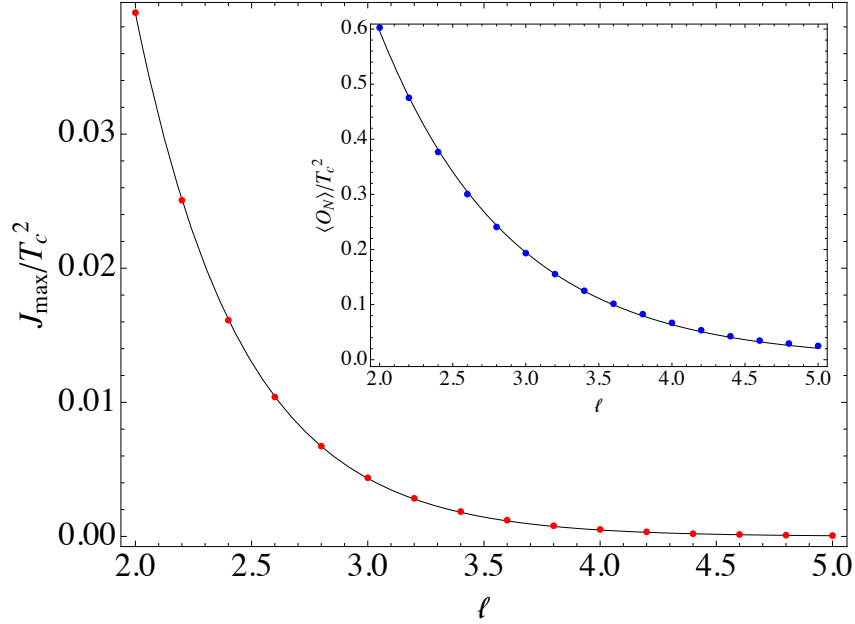


Figure 2.6: The relationship of the critical current and of the order parameter as the weak link length grows larger is illustrated in these two plots. Both sets of data are fitted to a decaying exponential and independently yield the same coherence length, up to a difference of 1.8%. We used $\mu_\infty = 10$, $\sigma = 0.4$ and $\epsilon = 0.05$ for both plots.

exponentially when the width ℓ of the weak link increases, i.e. it obeys a relation of the form⁴

$$\frac{J_{\max}}{T_c^2} = A_J e^{-\frac{\ell}{\xi}} \quad (2.13)$$

for $\xi \ll \ell$. Additionally, the order parameter at the center of the junction has a similar behaviour:

$$\frac{\langle \mathcal{O}_N \rangle}{T_c^2} = A_{\mathcal{O}} e^{-\frac{\ell}{2\xi}} \quad (2.14)$$

where $\langle \mathcal{O}_N \rangle$ is the magnitude of the order parameter in the normal phase

⁴Note that we have switched from the numerically convenient conventions of measuring dimensional quantities in units of the (varying) temperature T , to the more physical conventions of measuring those quantities in terms of the *fixed* temperature T_c .

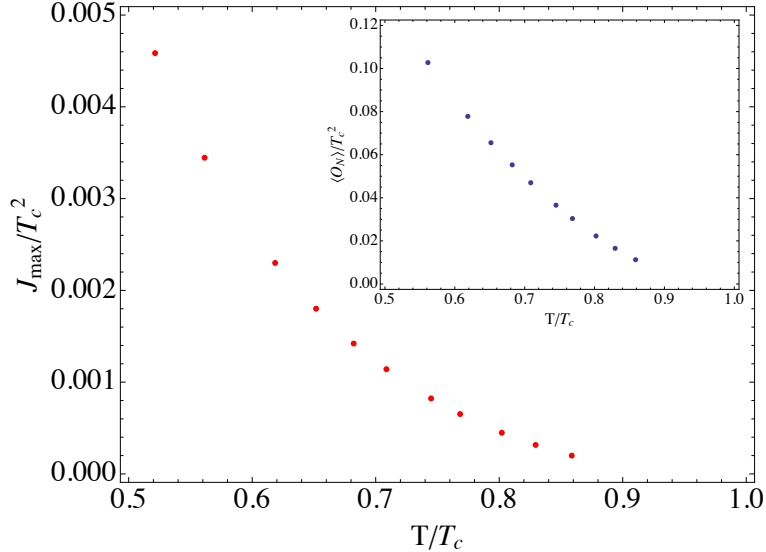


Figure 2.7: The dependence of the coherence length ξ , expressed through the critical current or order parameter $\langle \mathcal{O}_N \rangle$ (in the inset), on temperature. Near the critical point, the critical current follows a power law characteristic of the S-N-S junction, but with fairly large corrections. The parameters for the chemical potential used to produce these figures are $\ell = 4$, $\sigma = 0.6$ and $\epsilon = 0.3$.

($x = 0$), and the junction has no current. Both of these relations are due to the proximity effect, the leakage of the superconducting order into the normal state. Note then that the coherence length ξ should be the same in both cases. The results of our numerics show remarkable precision, yielding $\xi \approx 0.4547$ for the Josephson current, and $\xi \approx 0.4468$ for the order parameter: a difference of only 1.8%. See for instance Figure 2.6.

The coherence length has an interesting temperature dependence, plotted in Figure 2.7. While the plot does not have a simple fit, it has the expected behaviour at $T \rightarrow T_c$, where it vanishes due to the disappearance of superconductivity. Near the critical temperature the critical current is expected to vanish as [92]:

$$J_{\max}(T) \propto (T_c - T)^\beta \quad \text{near } T_c \quad (2.15)$$

For a conventional s-wave superconductor, and junctions wide compared

to the coherence length, a quadratic dependence ($\beta = 2$) is characteristic of the S-N-S junction, whereas different critical exponent are expected for other types of weak links (for example for the S-I-S junction $\beta = 1$). Interestingly, our results presented in Figure 2.7 indicate that $\beta \sim 2.52$; furthermore the exponent β also depends on the steepness and depth of the chemical potential profile. While β is closest to the critical exponent of the S-N-S junction, the corrections are fairly large. Those corrections are probably related to our setup having a varying chemical potential. It would be interesting to reproduce the expected scaling with a more conventional setup of a Josephson junction for which the chemical potential is spatially homogeneous.

2.5 Conclusions

In this paper we have started the investigation of Majorana bound states in the holographic context. We have discussed the dissipationless edge currents which are an indirect evidence for such modes. Additionally, we have constructed a Josephson junction involving a topological chiral superconductor, and probed the physics of the Josephson effect. The results we obtained are consistent with a conventional effect, with 2π periodic current-phase relation, and exponential decay of the current with the junction width.

These results support the expectation that though the physics is 4π periodic, an unconventional periodicity will not be visible in thermal equilibrium. The presence of Majorana modes corresponds to having two states which are exchanged upon a 2π phase rotation. However, in equilibrium the Josephson current receive contribution from both states, weighted according to their Boltzmann weight. This, thermal equilibrium results are expected to exhibits conventional periodicity, consistent with what we find,

It would be interesting to continue this investigation with the goal of displaying more direct signatures of the Majorana bound states. One such direct signature would be in the Andreev scattering off a superconducting interface – bound states can be then seen in analyzing the phase shift. Furthermore, one can construct holographically a non-equilibrium configuration which is expected to exhibit the unconventional periodicity associated with Majorana bound states. We hope to report on the result of such investigations in the near future.

Chapter 3

Dynamics of Holographic Entanglement Entropy Following a Local Quench

We discuss the behaviour of holographic entanglement entropy following a local quench in 2+1 dimensional strongly coupled CFTs. The entanglement generated by the quench propagates along an emergent light-cone, reminiscent of the Lieb-Robinson light-cone propagation of correlations in non-relativistic systems. We find the speed of propagation is bounded from below by the entanglement tsunami velocity obtained earlier for global quenches in holographic systems, and from above by the speed of light. The former is realized for sufficiently broad quenches, while the latter pertains for well localized quenches. The non-universal behaviour in the intermediate regime appears to stem from finite-size effects. We also note that the entanglement entropy of subsystems reverts to the equilibrium value exponentially fast, in contrast to a much slower equilibration seen in certain spin models.

3.1 Introduction

In recent years we have seen enormous progress in qualitative and quantitative understanding of out-of-equilibrium quantum dynamics. Theoretical and numerical methods have been very effective to unearth the generic behaviour of a variety of observables in such systems. Coupled with the rapid growth of experimental techniques in cold atom and many-body systems to probe such dynamics, one can furthermore ratify our theoretical understanding. Motivated by these considerations we continue our explorations of dynamics of strongly coupled non-equilibrium quantum systems using holographic methods.

One simple scenario of interest in many circumstances is a situation where we start with a QFT in global equilibrium and deform it by turning on external sources for relevant operators. The sources provide external dials which can serve to do work on the system and drive it out of equilibrium. We could consider sources that act homogeneously in space (but localized

in time), which is often referred to as *global quench*, or have it act locally in spacetime, which corresponds to a *local quench*. Both types of protocols are well studied in literature in the past decade or thereabouts. In either case we are considering deformations of the form

$$S_{\text{QFT}} \mapsto S_{\text{QFT}} + \int d^d x \mathcal{J}(x) \mathcal{O}(x), \quad (3.1)$$

where $\mathcal{O}(x)$ is a (composite) operator of the QFT and \mathcal{J} the classical source we dial. The distinction at this level between local and global quenches is simply in the spacetime support of the source $\mathcal{J}(x)$.

Much of the analytic progress in this front has been in 1+1 dimensional CFTs, where the quench protocols of the form (3.1) can be incorporated into a Euclidean path integral, and studied efficiently by computing correlation functions of the deforming operator $\mathcal{O}(x)$ in the unperturbed state of the CFT, cf., [62, 93] for the original discussion and [94] for a review.

Our primary interest is in exploring the dynamics of strongly coupled QFTs subject to such protocols in higher dimensions. A natural framework to explore this question is provided by the holographic AdS/CFT duality which maps the QFT problem onto the dynamics of a gravitational system in asymptotically AdS spacetime. For concreteness we will focus on 2+1 CFTs which are originally in global thermal equilibrium and subject them to a quench by a local scalar operator \mathcal{O} of dimension Δ . The gravitational problem then comprises of Einstein-Hilbert gravity coupled to a massive scalar, whose mass m is related to the conformal dimension by the standard formula, viz., $\Delta = \frac{3}{2} + \sqrt{\frac{9}{4} + m^2 \ell_{\text{AdS}}^2}$.¹ The initial global equilibrium state maps onto a planar Schwarzschild-AdS₄ black hole and the problem at hand involves analyzing the deformation of this said black hole consequent to turning on a boundary source for the scalar field. This then amounts to a gravitational infall problem. The pulse of scalar on the boundary propagates into the bulk and dissipates through the black hole horizon. Of interest to us are the observables in the interim process.

While there are many quantities that could be, and indeed have been [41, 47, 49–53, 55–59, 61, 95–121], studied in this context, we will for definiteness focus our attention on entanglement entropy. While strictly not an observable, the entanglement entropy for a particularly chosen spatial region of the QFT captures important aspects of the field theory dynamics. Not only does it provide a measure of how correlations in the system

¹ We will only consider deformations by operators which are well separated from the unitarity bound – our focus will be on conformally coupled scalars with $\Delta = 2$.

evolve following the quench, but it furthermore is also a simple quantity to compute in the holographic context. The holographic entanglement entropy proposals of [38, 39] and their covariant generalization [41] provide an extremely simple route to its computation. All we are required to do is solve a classical problem of finding areas of extremal surfaces anchored on the said region of interest.

In what follows we will explore how holographic entanglement entropy evolves following a local quench. We will restrict our attention to a very specific scenario, wherein we quench a CFT_3 with a $\Delta = 2$ operator. The disturbance will be taken to be localized in space and time – we pick exponential damping in space and an inverse Pöschl-Teller switch on/off in time, cf., (4.26). We retain translational invariance in one spatial direction, breaking homogeneity in the other. We study entanglement entropy for strip-like spatial regions that are aligned with the symmetry we retain, so that the problem of finding extremal surfaces can be mapped to effectively finding geodesics in an auxiliary three dimensional spacetime. Of interest to us are how the entanglement entropy growth is correlated with the position and size of the strip relative to the quench location.

To appreciate the question, let us recall some well known facts. The classic analysis of [62] of entanglement entropy growth following a global quench in CFT_2 has spurred lots of activity on the subject. While the two dimensional case can effectively be described by a quasiparticle picture, since the entanglement growth is linear due to left and right movers decoupling (following an initial quadratic ramp up [47, 61, 103]), the holographic models present a much different picture in higher dimensions.²

The results of various analyses of global quenches have been beautifully encapsulated in the ‘entanglement tsunami’ picture developed by Liu-Suh in [47, 61] and further explored recently in [63]. Following an initial quadratic growth in time, the entanglement entropy for any region grows linearly at a rate dictated by the tsunami velocity v_E . To define this quantity unambiguously the authors chose to normalize the local value of entanglement entropy relative to the final thermal entropy expected for the same region once equilibration is complete. This does leave a single parameter which

² We note here that oftentimes global quenches are holographically modeled by considering a Vaidya-AdS geometry (see [41, 122] for early discussions) that corresponds to infalling null matter in the bulk, which does not accord a clean CFT interpretation. A cleaner perspective is offered by either solving the non-linear dynamics of gravity coupled to realistic matter like a scalar field, or more simply by implementing an end of the world brane boundary state [106] explicitly in holography. The results for the growth of entanglement entropy are however independent of the particularities of the modeling.

is the aforementioned velocity. It was found not only $v_E \leq 1$ as required by causality with equality in $d = 2$ consistent with the CFT_2 analysis, but one could further bound it by a universal dimensional dependent constant $v_E^*(d)$.³ This upper bound on velocity was attained holographically for matter that collapsed into a Schwarzschild- AdS_d black hole at late times.

Given this rather clear situation for global quenches, we are interested in ascertaining the behaviour when we localize the quench protocol to a finite spatial domain. We in principle could focus on deformations by sources delta-function supported at point. This is natural when studying this problem in QFT as one can map the computation to that of computing correlation functions on some background, however for our purposes of carrying out numerical investigations we choose to smear out the source. We expect firstly that the underlying locality of the QFT forces entanglement entropy to behave causally; as explained in [45, 123] this means that the source makes its presence felt only when it acts in the causal past of the entangling surface (the boundary of the region of interest). This is indeed what one sees in explicit computations in CFT_2 . The entanglement entropy only starts changing after a time lag set by the time it takes for the quench disturbance to propagate between the region of interest and its complement. As long as the quench front is localized either in the region or in the complement, we only have the initial state entanglement.

Previous analyses of holographic local quenches by [104] involved modeling the system by the infall of a massive particle – this is effectively an eikonal approximation wherein one is assuming that the wavepackets of the quench are tightly collimated. Moreover, the authors chose to work with very heavy operators $\Delta \gg 1$ which could then be approximated in terms of worldlines of a small black holes. The relevant geometry can be obtained by applying a suitable symmetry transformation to the global Schwarzschild- AdS black hole and with it in hand properties of holographic entanglement entropy were explored. This picture was further supported by field theory analysis of such deformations at large central charge [124, 125]. Our aim to tackle this problem from a different perspective by studying the entanglement evolution in a quenched gravitational background as explained above. We will recover most of the results mentioned above in our analysis.

We can moreover explore quantitative features of the entanglement evo-

³ This statement as far as we are aware is robust for QFTs whose holographic duals are given in terms of two derivative Einstein-Hilbert gravity coupled to sensible matter. There is a-priori no reason for them to hold when the gravitational dynamics includes higher derivative corrections and we in particular are not aware of any statement of this kind.

lution. We see that the propagation of entanglement is confined to an effective light-cone. We extract an entanglement velocity v_E from this emergent causal structure. Unlike the case of the global quench, the velocity depends on the details of the quench. It appears to grow monotonically with increase in the amplitude of the quench source as well as with the increase of the initial temperature. For a certain range of parameters it appears to track the tsunami velocity bound $v_E^*(3)$ of [47], while for others it reaches close to the speed of light.

There is a somewhat annoying fact that the tsunami velocity $v_E^*(3) = 0.687$ in three spacetime dimensions is marginally lower than the speed of sound $v_s = 0.707$, making it somewhat hard to convincingly point to precise origin of the effect. We also see contamination from edge effects both from finite size of \mathcal{A} and the finite width of the quench source. We have not examined the detailed non-linear effects that cause the velocity to grow from the tsunami bound towards the speed of light, but display some examples which illustrate the pattern.

While our numerical results are constrained to probing small spatial regions relative to thermal scale,⁴ we nevertheless are able to extract both this entanglement velocity as well as examine the return to the equilibrium. In contrast to studies in lattice models in low dimensions which display a logarithmic return of entanglement entropy to its equilibrium value after the quench, we find that the holographic systems prefer to equilibrate exponentially.

The outline of the paper is as follows. In §4.2 we describe the basic set-up for holographic local quenches, describing the general methodology and the determination of entanglement entropy from the gravitational background. In §3.3 we give the basic numerical results for the quench spacetime and extremal surfaces therein. The key statements regarding the behaviour of entanglement entropy in a locally quenched CFT are then extracted in §3.4, where we describe the growth velocity v_E and the return to equilibrium. We end with some open questions in §3.5. Some details of the numerical methods are collected in Appendices A and B.

⁴This constraint arises because our numerical solutions only determine the geometry to the exterior of the apparent horizon. For small regions \mathcal{A} the extremal surfaces stay in this domain, but for larger regions, they do penetrate the apparent horizon – see [50, 126].

3.2 Preliminaries: Holographic Local Quench

We are interested in the behaviour of entanglement entropy in a $2 + 1$ dimensional field theory that has been driven out of equilibrium locally by an inhomogeneous relevant scalar operator. Holographically, this amounts to solving the gravitational dynamics of a $3+1$ dimensional asymptotically AdS spacetime and its consequences for the area of extremal surfaces anchored on the boundary.

3.2.1 Metric Ansatz

In order to dynamically evolve a spacetime geometry following a local quench, it is convenient to choose our metric ansatz to be a generalization of the infalling Eddington-Finkelstein coordinates for black holes. We choose to work in an asymptotically AdS₄ spacetime, dual to a $2 + 1$ dimensional CFT,

$$ds^2 = -2 A e^{2\chi} dt^2 + 2 e^{2\chi} dt dr - 2 F_x dt dx + \Sigma^2 (e^B dx^2 + e^{-B} dy^2), \quad (3.2)$$

where r denotes the radial bulk coordinate, with the boundary lying at $r = \infty$, and t is a null coordinate that coincides with time on the boundary. We have chosen our quench to be localized in the x -direction and translationally invariant in the y direction. Hence all the fields appearing above $\{A, \chi, F_x, \Sigma, B\}$ depend only on the coordinates $\{r, t, x\}$ with ∂_y being an isometry.

This choice for the metric has many advantages: it provides us with coordinates that remain regular throughout the entire domain as the spacetime equilibrates, it leads to a characteristic formulation of our gravitational infall problem, and it comes with a residual radial diffeomorphism that is of great computational help [73]. Indeed, the metric (3.2) remains invariant under radial shifts,⁵

$$r \rightarrow \bar{r} = r + \lambda(x^\mu). \quad (3.3)$$

On physical grounds, we anticipate that the black hole's horizon will grow locally as the effects of matter from the boundary are felt in the interior of the bulk. Hence a sensible gauge choice is to dynamically determine λ so that the coordinate location of the black hole's apparent horizon⁶ remains

⁵ For notational clarity, we use upper case Latin indices $\{M, N, \dots\}$ to represent bulk coordinates, and lower case Greek indices $\{\mu, \nu, \dots\}$ to refer to boundary coordinates.

⁶ See Appendix A for further details about our numerical scheme

fixed. This keeps the calculational domain simple.

Einstein's equations in the presence of a scalar field are given by

$$\begin{aligned}
 R_{MN} - \frac{R}{2}G_{MN} - \frac{d(d-1)}{2\ell_{\text{AdS}}^2}G_{MN} &= T_{MN} \\
 T_{MN} = \nabla_M\Phi\nabla_N\Phi + G_{MN}\mathcal{L}_\Phi, \quad \mathcal{L}_\Phi &= -\frac{1}{2}(G^{MN}\nabla_M\Phi\nabla_N\Phi + m^2\Phi^2).
 \end{aligned}
 \tag{3.4}$$

For simplicity, we restrict our attention to $m^2\ell_{\text{AdS}}^2 = -2$ so that the asymptotic expansion of the scalar field near the boundary is analytic in powers of $1/r$:

$$\Phi(r, t, x) = \frac{\phi_0(t, x)}{r} + \frac{\phi_1(t, x)}{r^2} + \dots
 \tag{3.5}$$

We note that since t is a null coordinate, $\phi_1(t, x)$ will have contributions coming from both the source and the response of the scalar field, as will be explained below.

3.2.2 Asymptotic Geometry

In a theory of gravity on asymptotically AdS spacetimes, asymptotic analysis alone is not sufficient to determine the bulk metric [13]. Indeed, the missing piece in the asymptotic analysis is the boundary stress tensor, determined by solving the full bulk equations:

$$T_{\mu\nu} \sim g_{\mu\nu}^{(3)},
 \tag{3.6}$$

where $g_{\mu\nu}^{(3)}$ is the part of the metric undetermined by the equations of motion for $d = 3$.

While our infalling coordinate chart (3.2) differs from the standard Fefferman-Graham chart typically used for asymptotic expansions, it is a straightforward exercise to carry out an asymptotic analysis. Demanding that the field equations are obeyed in the near-boundary $r \rightarrow \infty$ domain we

find

$$A(r, t, x) = \frac{(r + \lambda(t, x))^2}{2} - \partial_t \lambda(t, x) - \frac{1}{4} \phi_0(t, x)^2 + \frac{a^{(3)}(t, x)}{r} + \dots \quad (3.7)$$

$$\chi(r, t, x) = \frac{c^{(3)}(t, x)}{r^3} + \dots \quad (3.8)$$

$$F_x(r, t, x) = -\partial_x \lambda(t, x) + \frac{f^{(3)}(t, x)}{r} + \dots \quad (3.9)$$

$$\Sigma(r, t, x) = r + \lambda(t, x) - \frac{1}{4} \phi_0(t, x)^2 + \dots \quad (3.10)$$

$$B(r, t, x) = \frac{b^{(3)}(t, x)}{r^3} + \dots \quad (3.11)$$

One may also show that the explicit map to the Fefferman-Graham coordinates $\{\tau, \rho, \xi\}$ takes the asymptotic form

$$\tau(r, t, x) = t + \frac{1}{r} - \frac{\lambda(t, x)}{r^2} + \dots, \quad (3.12)$$

$$\rho(r, t, x) = r + \lambda(t, x) - \frac{1}{4} \frac{\phi_0(t, x)^2}{r} + \dots, \quad (3.13)$$

$$\xi(r, t, x) = x + \mathcal{O}(r^{-3}). \quad (3.14)$$

Additional care needs to be taken when dealing with scalar fields in a theory of gravity formulated in terms of null coordinates. Indeed, the falloff of scalar fields with $m^2 \ell_{\text{AdS}}^2 = -2$ is known to behave in Fefferman-Graham coordinates as:

$$\Phi(\rho, \tau, \xi) = \frac{\phi_{\text{source}}(\tau, \xi)}{\rho} + \frac{\phi_{\text{response}}(\tau, \xi)}{\rho^2} + \dots \quad (3.15)$$

as we approach $\rho \rightarrow \infty$. By using the coordinate expansion above, we obtain

$$\begin{aligned} \Phi(r, t, x) &= \frac{\phi_{\text{source}}(t, x)}{r} \\ &+ \frac{\phi_{\text{response}}(t, x) + \partial_t \phi_{\text{source}}(t, x) - \lambda(t, x) \phi_{\text{source}}(t, x)}{r^2} + \dots, \end{aligned} \quad (3.16)$$

thus confirming our earlier claim that $\phi_1 = \phi_{\text{response}} + \partial_t \phi_0 - \lambda \phi_0$ mixes the source and the expectation value of the scalar.

3.2.3 Boundary Stress Tensor

In order to solve Einstein's equations as efficiently as possible, we found it useful to use the boundary stress tensor and its conservation equations to find and propagate the undetermined fields $a^{(3)}$ and $f^{(3)}$ accurately in time (in our scheme, $b^{(3)}$ and $c^{(3)}$ need to be read off from the solutions directly). For asymptotically AdS₄ spacetimes, the boundary stress tensor in the presence of a scalar field of mass squared $m^2 \ell_{\text{AdS}}^2 = -2$ can be expressed in the Brown-York form as

$$T_{\mu\nu} = K_{\mu\nu} - K\gamma_{\mu\nu} + 2\gamma_{\mu\nu} - \left(\gamma R_{\mu\nu} - \frac{1}{2} \gamma R \gamma_{\mu\nu} \right) + \frac{1}{2} \gamma_{\mu\nu} \phi^2, \quad (3.17)$$

where we have introduced some boundary data: $\gamma_{\mu\nu}$ is the induced metric on the boundary, $K_{\mu\nu}$, $K \equiv \gamma^{\mu\nu} K_{\mu\nu}$ its extrinsic curvatures, and ${}^\gamma R_{\mu\nu}$, ${}^\gamma R$ its intrinsic curvatures. Explicitly in terms of the asymptotic expansion coefficients we find that the energy-momentum tensor takes the form

$$T_{00} = 2a^{(3)} + 4c^{(3)} + \phi_0 \phi_{\text{response}}, \quad (3.18)$$

$$T_{tx} = \frac{3}{2} f^{(3)} - \frac{1}{2} \phi_0 \partial_x \phi_0, \quad (3.19)$$

while the conservation equations in the presence of the scalar source $\phi_0(x, t)$ read

$$\partial_t T_{00} = \partial_x T_{tx} + \partial_t \phi_0 \phi_{\text{response}}, \quad (3.20)$$

$$\partial_t T_{tx} = \frac{1}{2} \left(\partial_x T_{00} - 3 \partial_x b^{(3)} + \partial_x \phi_0 \phi_{\text{response}} - \phi_0 \partial_x \phi_{\text{response}} \right). \quad (3.21)$$

We take our initial state to be in thermal equilibrium, which translates to an initial condition on the bulk metric, which is then the planar static Schwarzschild-AdS₄ black hole spacetime with temperature

$$T = \frac{3M^{\frac{1}{3}}}{4\pi}. \quad (3.22)$$

The initial boundary stress tensor is then simply $T^\mu_\nu = \text{diag}\{1, \frac{1}{2}, \frac{1}{2}\}$. To model our local quench, we simply need to specify a source function $\phi_0(t, x)$ and let the system evolve according to the Einstein equations, all while making sure that λ is gauge-chosen to fix the location of the apparent horizon.

3.2.4 Holographic Entanglement Entropy

Once we have obtained solutions for the local quench, we can study the subsequent dynamics of the entanglement entropy of a region \mathcal{A} on the boundary using the covariant holographic entanglement entropy prescription [41]. The latter requires us to determine extremal surfaces anchored on the entangling surface on the boundary.

For simplicity, we exploit the translational invariance, and restrict our attention to a strip-region

$$\mathcal{A} = \{(x, y) \mid x \in (-L, L), y \in \mathbb{R}\}, \quad \partial\mathcal{A} = \{(x, y) \mid x = \pm L, y \in \mathbb{R}\}. \quad (3.23)$$

The extremal surfaces $\mathcal{E}_{\mathcal{A}}$ anchored on $\partial\mathcal{A}$ are straightforwardly determined by solving a set of ODEs. Using coordinates adapted to the ∂_y isometry, we parameterize the surface by coordinates y, τ . Consequentially, $\mathcal{E}_{\mathcal{A}}$ is then obtained by solving the geodesic equations in an auxiliary three dimensional spacetime with metric $\tilde{g}_{MN} dX^N dX^M = g_{yy} g_{MN} dX^N dX^M$, with the restriction to $y = \text{constant}$ understood, i.e., $X^M(\tau) = \{t(\tau), r(\tau), x(\tau)\}$. Equivalently we solve the Euler-Lagrange equations obtained from the Lagrangian $\mathcal{L} = g_{yy} g_{MN} \dot{X}^M \dot{X}^N$.

While we have phrased the determination of $\mathcal{E}_{\mathcal{A}}$ as a boundary value problem, it is practical to switch to an initial value formulation. We parameterize the solutions by specifying the turning point, or tip, of the geodesic in the bulk, $X_*^M(\tau) = \{t_*, r_*, x = 0\}$, and evolve towards the boundary using an ODE solver (for instance the Matlab solver *ode45*) until both $\partial\mathcal{A}$ and a specified UV cutoff are reached.

To this end, we have chosen to transform our system of 3 second order ODEs into a system of 6 first order ODEs in the variables

$$\{t, P_t \equiv \Sigma^2 \dot{t}, r, P_+ \equiv e^{2\chi} (\dot{r} - A \dot{t}), x, P_x \equiv \Sigma^2 \dot{x} - e^{-B} F_x \dot{t}\}. \quad (3.24)$$

With these new variables,⁷ $\mathcal{L} = 2P_+ P_t + P_x^2$. The boundary conditions at the turning point are

$$\{t = t^*, P_t = 0, r = r^*, P_+ = 0, x = 0, P_x = \pm 1\}. \quad (3.25)$$

The conditions on P_t and P_+ are a consequence that, because of symmetry,

⁷ These definitions for the momenta ensure that all quantities are of order $\mathcal{O}(1)$ for numerical stability.

we expect $\dot{t} = \dot{r} = 0$ at X^* , whereas the condition for P_x has been chosen to normalize the action by setting $\mathcal{L} = 1$. The sign determines whether the geodesic will go towards the positive or negative x -axis.

To translate from the length of the geodesic to the actual entanglement entropy $S_{\mathcal{A}}$ we pick an IR regulator L_y along the translationally invariant direction and a UV cutoff ϵ . We choose to present the results for the regulated entanglement entropy by subtracting off the corresponding answer in the unperturbed theory. There are two natural regularizations we can use: Regulator 1: We subtract the entanglement in the ‘instantaneous thermal state’ obtained by taking the Schwarzschild-AdS₄ metric with a horizon located at $r_+(x, t) = M^{\frac{1}{3}} + \lambda(t, x)$. This choice allows clean matching of the asymptotic coordinate chart.

Regulator 2: We alternately can choose to subtract of the vacuum entanglement entropy for the same region, with a dynamical UV cut-off $\epsilon_{\text{vac}}(x, t)$. This gives

$$\Delta S_{\mathcal{A}} = L_y \left[\int d\tau - \frac{2}{\epsilon} - 2\lambda(t, x) + \frac{4\pi}{L} \left(\frac{\Gamma(\frac{3}{4})}{\Gamma(\frac{1}{4})} \right)^2 \right]. \quad (3.26)$$

The two regulators differ by a finite amount that is invariant temporally, allowing us to cross-check our numerical results. In what follows we will simply quote $\Delta S_{\mathcal{A}}$ normalized by L_y .

3.3 The Quench Spacetime and Extremal Surfaces

We now turn to describing the results of solving Einstein’s equations sources by the scalar field boundary condition. We then describe properties of the extremal surfaces of interest in these geometries.

3.3.1 Numerical Solutions

We use the characteristic formulation of Einstein’s equations resulting from the null slicing of spacetime outlined in [73] to numerically find the geometry. Even though we start with a complicated set of PDEs, the characteristic formulation simplifies the equations of motion into two categories: the equations for the auxiliary fields that are local in time and reduce to a nested set of radial ODEs, and the equations for dynamical quantities that encode the evolution of the geometry.

To numerically integrate the Einstein and Klein-Gordon equations, we discretize the radial direction using a Chebyshev collocation grid. This choice of discretization for the extra dimension is particularly well suited to find smooth solutions to boundary value problems while ensuring their exponential convergence as the grid size is increased. We opted to choose a rational Chebyshev basis to deal with the non-compact spatial direction. The main advantage of working with a rational Chebyshev grid is that the boundary conditions at $x = \pm\infty$ are already implemented *behaviourally*; as long as the solution decays at least algebraically fast or asymptotes to a constant, we can avoid specifying the boundary conditions explicitly [127]. We use a grid of 41 points in both directions. To propagate in time, we use an explicit fifth-order Runge-Kutta-Fehlberg method with adaptive step size. We also avoid aliasing in both the radial and spatial directions by applying a low-pass filter at each time step that gets rid of the top third of the Fourier modes.

We chose the source function to be $\phi_0(t, x) = f(x)g(t)$ with

$$f(x) = \frac{\alpha}{2} \left[\tanh\left(\frac{x+\sigma}{4s}\right) - \tanh\left(\frac{x-\sigma}{4s}\right) \right], \quad g(t) = \operatorname{sech}^2\left(\frac{t-t_q\Delta}{t_q}\right). \quad (3.27)$$

With it, we can ramp up the scalar field to reach its maximum value α at time $t = t_q\Delta$ before it vanishes again. The parameters $\{s, t_q, \Delta\}$ are chosen to facilitate the numerics, whereas σ determines the width of the perturbation. In practice, we found $s = 0.15$, $t_q = 0.25$ and $\Delta = 8$ to give us satisfying accuracy for the late-time behaviour of the scalar field while preserving a nicely localized shape for the pulse. So we therefore study the quench protocols parametrized by two parameters: an amplitude α and a width σ . Along with the initial temperature of the system which we take to be parametrized by M , we have three parameters at our disposal.

$$\phi_0(x, t) = \frac{\alpha}{2} \left[\tanh\left(\frac{5}{3}(x+\sigma)\right) - \tanh\left(\frac{5}{3}(x-\sigma)\right) \right] \operatorname{sech}^2(4t-8),$$

Protocol parameters: $\{\alpha, \sigma, M\}$

(3.28)

The evolution of the spacetime following our quench is fairly simple. The injection of local excitation results in hydrodynamical evolution almost from the very beginning (cf., [95, 96] for analogous statements with spatial homogeneity). Since our perturbation excites the sound mode of the system,

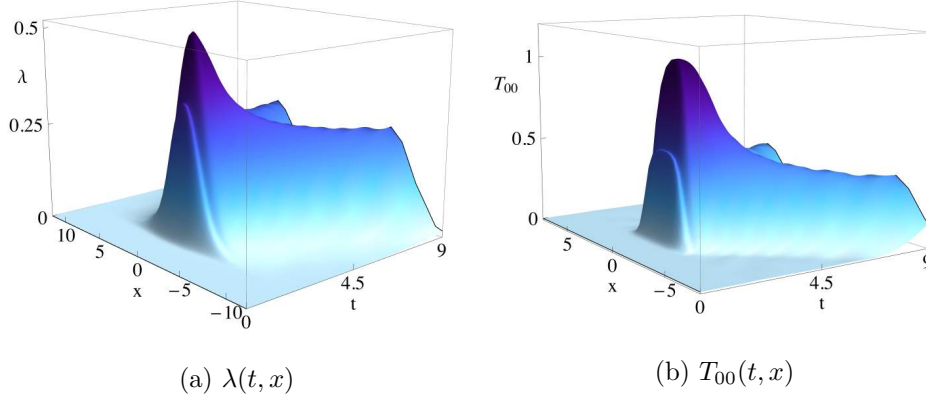


Figure 3.1: Evolution profile of the (a) radial shift $\lambda(x, t)$, and (b) $T_{00}(x, t)$ component of the stress tensor, for $\alpha = 0.5$, $M = 0.1$, $\sigma = 2$. The field λ determines the evolution of the entropy in our solution.

we have the initial energy-momentum perturbation dispersing at the speed of sound. The presence of shear viscosity results in entropy production, manifested in the solution by the local growth of the horizon area element.

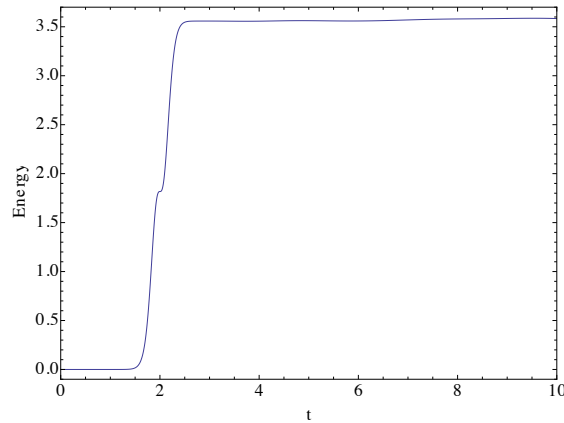


Figure 3.2: Evolution of the total energy on the boundary $E = \int T_{00} dx$ after a quench described by parameters $\alpha = 0.5$, $M = 0.1$, $\sigma = 2$.

In Figure 3.1a we display the spatial and temporal profile of the function $\lambda(x, t)$, related to the area element of the horizon. We see that the initial

perturbation indeed results in entropy production, as expected. Curiously, the initial perturbation splits to two localized perturbations after some time; those follow the expected hydrodynamic evolution. Figure 3.1b shows the equivalent evolution of the energy density for the same set of parameters. Finally, Figure 3.2 shows that following the conclusion of the quench the total energy is conserved. These features verify the intuitive picture of hydrodynamical evolution following a local excitation of the system.

To quantify the entropy production, we can monitor the growth of the area of the apparent horizon as a function of time. In order to express the result in physical units, we need to convert from the natural time scale on the horizon to the time measured in the boundary. Recall that our solutions for the metric components are obtained on a slice of constant ingoing time coordinate t . We could, following [128], map the horizon data along ingoing null geodesics to the boundary. We will refrain from doing so explicitly and instead work directly in the chosen coordinates leaving implicit this translation.⁸

Using the induced metric h_{ab} on a constant t slice we obtain the area element on the horizon which can be integrated directly. Since the naive answer is infinite, we regulate it by removing the contribution from the initial equilibrium state (i.e. subtract off the static Schwarzschild-AdS answer) to obtain:

$$\Delta\text{Area}_h = L_y \int_{r=r_h} \left(\Sigma^2 \sqrt{1 + 2\lambda' e^{-2\chi-B}} - r_h^2 \right) dx \quad (3.29)$$

The numerical results are expressed in Figure 3.3, where we also show the total energy for comparison. Notice the striking resemblance of the horizon's area evolution with that of the total energy injected into the system by the quenching scalar field. This seems to indicate that the growth of the horizon is dictated by processes governed by the speed of sound, such as energy and momentum transport. This is indeed the intuition we would have from the hydrodynamic regime of slow variations and it is a reassuring check of the set-up that this indeed is upheld.

3.3.2 Extremal Surfaces

Having the solution at hand we can compute the extremal surfaces as described in §3.2.4. In Figure 3.4 we display the radial depth of the turning point for the extremal surfaces, as function of (boundary) time. Different

⁸ We also note that $\lambda(t, x)$ is defined on a constant ingoing time slice, and as such the radial shifts affect the horizon “instantaneously” rather than causally.

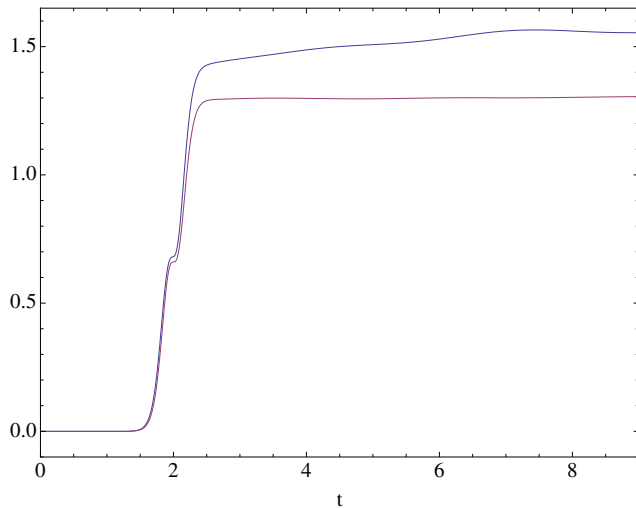


Figure 3.3: I The growth of the apparent horizon (in blue) as a function of boundary time, for $\alpha = 0.3$ and $M = 0.1$. We also overlay the plot for the total energy $\int T_{00} dx$ produced by quenching the system in red for direct comparison.

points correspond to different extremal surfaces, which contribute to entanglement entropy of surfaces of varying lengths. We have plotted the radial depth both in the computational coordinate (in which the horizon is at fixed radial distance) and in coordinates in which the horizon grows.

Since our computational domain ends at the apparent horizon, we cannot probe extremal surfaces that extend past into the trapped region. These are known to exist in various explicit simulations (cf., [126] for a comprehensive survey in Vaidya-AdS spacetimes). Pragmatically, this restricts our attention to small regions \mathcal{A} . We will nevertheless see that despite this restriction we can still extract interesting physical features of $S_{\mathcal{A}}$ using surfaces that lie outside the apparent horizon.

One of the interesting features to notice from Figure 3.4 is that the geodesics never go beyond their initial depth in the bulk when we consider their position in the *ungauged* radial coordinate, i.e., where the radial depth

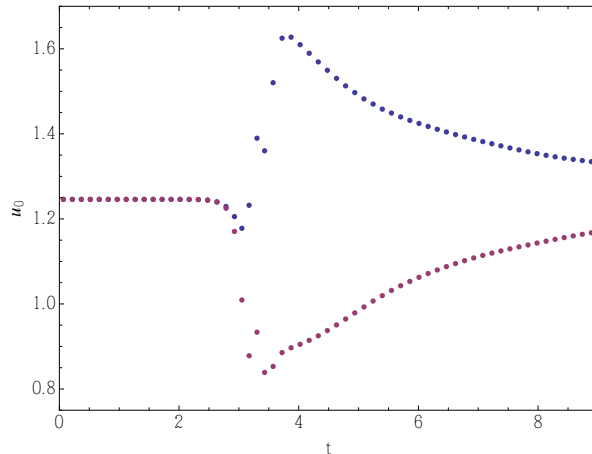


Figure 3.4: Evolution of the geodesics' radial depth for a quench; $\alpha = 0.5$, $M = 0.1$, $L = 0.8$, $\sigma = 2$. The blue data points represent the radial depth u^* in the fixed, gauged coordinate system, whereas the red data points represent the ungauged radial depth U^* .

is

$$U^* \equiv \frac{u^*}{1 + \lambda(t^*, x=0)u^*}, \quad (3.30)$$

with $u^* = 1/r^*$ being the radial position of the tip in the coordinate system where the apparent horizon is at a fixed coordinate locus.

3.4 Propagation of Entanglement Entropy

Armed with the numerical results for the spacetime geometry and the extremal surfaces therein, we are now in a position to extract some physical lessons for the evolution of entanglement entropy following a local quench. We restrict our attention to regions \mathcal{A} centered around the source of the initial excitation which is taken to be w.l.o.g. at $x = 0$. We will examine the behaviour of $\Delta S_{\mathcal{A}}$ as a function of the width L of the strip and time t after the quench.

We note that the region of parameter space that we can explore numerically is limited. The amplitude α of the scalar field cannot be too large,

otherwise the time-evolution of the quench solution does not converge. Similarly, the evolution code becomes unstable if the spatial discretization falls below a critical grid size, which has for consequence that we cannot resolve quenches with width σ below a certain threshold. The width L of the entangling surface is in turn constrained by the initial values we can pick for M , which determines the position of the event horizon of the initial configuration: if M is taken to be large, then we cannot find extremal surfaces that go deep enough in the bulk to probe larger regions \mathcal{A} , whereas if M is taken too small, then it becomes increasingly harder to quench the spacetime with a scalar source. We found that using quenches with width $\sigma = 2$, together with M ranging from 0.005 and 0.2 and α between 0.1 and 0.5, yielded interesting results that remained mostly the same, albeit delayed in time, as those with σ chosen larger.

Before proceeding we remind the reader that for regions \mathcal{A} which are much wider than the width of the quench source profile, there is a time delay before the entanglement entropy starts to change. This is consistent with the causal properties one would require of entanglement. Only when the quench can affect both the region and its complement (by being in the past of the entangling surface) would we expect a change in the entanglement for \mathcal{A} . This is clearly borne out in our simulations and is used to benchmark that we are on the right track.

3.4.1 An Emergent Light-cone

We first note that the entanglement generated by the local quench is linearly dispersing, i.e., it traces an effective light-cone. This is quite reminiscent of the Lieb-Robinson bound [129] in non-relativistic theories, where correlations follow an effective information light-cone. The speed of entanglement propagation is then denoted by v_E below.

The velocity v_E we find is bounded from below. A-priori one might guess whether the lower bound is given by the speed of sound, which is the speed in which the initial pulse spreads, thereby further exciting the system and generating additional entanglement on larger scales. The true speed is however a bit lower, as we shall see, suggesting that the mechanism of entanglement propagation differs from that which drives physical transport of energy and other conserved charges in the system.⁹

⁹ A-priori this statement appears reasonable, since the propagation of energy in the system is governed by the ability of the system to homogenize, which per se is not the same as becoming quantum entangled. There is thus far no clear mechanism for intuiting entanglement transport in quantum field theories, though the attempts of [63]

We therefore interpret the velocity v_E as the speed in which the initial entanglement, generated locally by the quench, propagates in time. The entanglement velocity can be extracted from the emergent light-cone defined along the curve where $\Delta S_{\mathcal{A}}(t)$ reaches a maximum for every L in the $L - t$ plane. We remark that unlike the results of [104], the height of this peak does not remain constant in our setup. Instead, we find that the maximum value of $S_{\mathcal{A}}(t)$ increases as we increase L .

This behaviour of the entanglement entropy can be quantified rather explicitly. We find that dependence is strongest when the amplitude of the scalar field is varied. For small sizes L , the maximum of $S_{\mathcal{A}}$ increases linearly with L . If we denote the slope of these curves by \mathfrak{s} , then we find the interesting relation

$$\frac{\partial}{\partial L} S_{\mathcal{A}}(L, t_{\max}, \alpha) = \mathfrak{s}(\alpha) \sim \alpha^2 \quad \text{for small/intermediate regions.} \quad (3.31)$$

The actual scaling for the slopes obtained from our numerical data are:

- $\mathfrak{s}(\alpha) \sim \alpha^{1.92}$ for $\alpha = \{0.1, 0.2, 0.3, 0.4, 0.5\}$ and $M = 0.1$
- $\mathfrak{s}(\alpha) \sim \alpha^{2.0043}$ for $\alpha = \{0.05, 0.1, 0.15, 0.2\}$ and $M = 0.01$

In the first case, the linear behaviour is shown in Figure 3.5. In the second instance (not pictured), while the linear nature breaks down when L is large, the slopes for small to intermediate regions still depend quadratically on the amplitudes. The dependence on temperature is less interesting. When the temperature M changes, the maximum of the entanglement entropy shifts slightly, as can be seen in Figure 3.6.

For general values of parameters, the entanglement velocity v_E changes with parameters, always bounded from below by the tsunami velocity (4.31), and above by the speed of light. We do however find two universal results which we now turn to.

Universal Behaviour at High Temperature

In the limit of an approximate global quench where the region \mathcal{A} is contained within the local quench, i.e., $L \lesssim \sigma$, and at high temperatures, we find a universal light-cone velocity $v_E = 1$ (to very high accuracy), regardless of the amplitude of driving scalar field (including values well within the non-linear regime)¹⁰. This is depicted in Figure 3.7. We note that for some values of

suggest potentially interesting mechanisms for the same.

¹⁰ It is worth noting that previous results for global quenches could not have seen this feature since the entanglement entropy saturates for strip geometries.

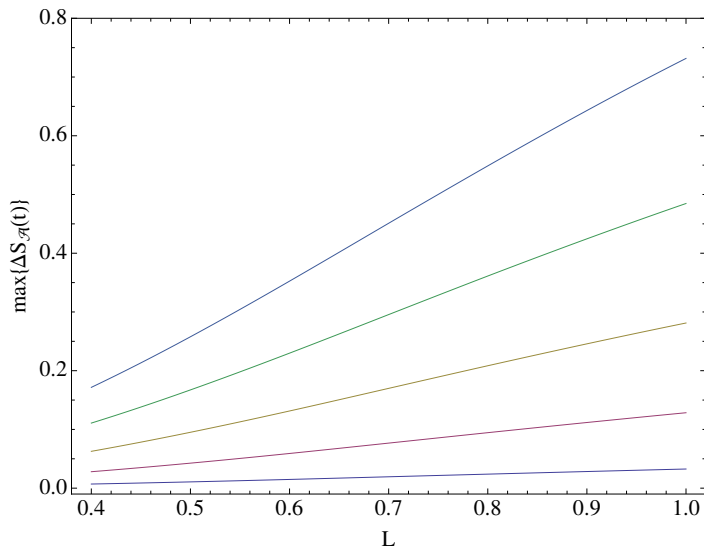


Figure 3.5: Maximum of the entanglement entropy $S_{\mathcal{A}}(t)$ as a function of L , for $\alpha = \{0.1, 0.2, 0.3, 0.4, 0.5\}$ starting from the bottom, and $M = 0.1$. The slopes of these curves depend quadratically on the amplitude α of the scalar field.

parameters, this universal behaviour can be affected by edge effects of the local quench, and is seen for small enough surfaces only.

As we decrease the black hole temperature, the velocity at the small surfaces becomes lower than 1. This confirms that $v_E = 1$ is a high temperature effect only.

Wide Quench Profiles

An interesting feature of the emergent light-cone is the abrupt change of velocity as the width of the region \mathcal{A} , L , is increased. When the size of the region \mathcal{A} becomes of the same order as the width of the local quench, the curve traced by the peak of the entanglement entropy goes from one linear regime to another, as shown in Figs. 3.8a, 3.8b, and 3.8c.

Interestingly, for the first two data sets (for which $\alpha = 0.1$, $M = \{0.005, 0.01, 0.02\}$, $\sigma = 2$), the light-cone velocities $v_E = \{0.678, 0.688, 0.706\}$ are very close to the tsunami velocity of a Schwarzschild-AdS₄ black hole

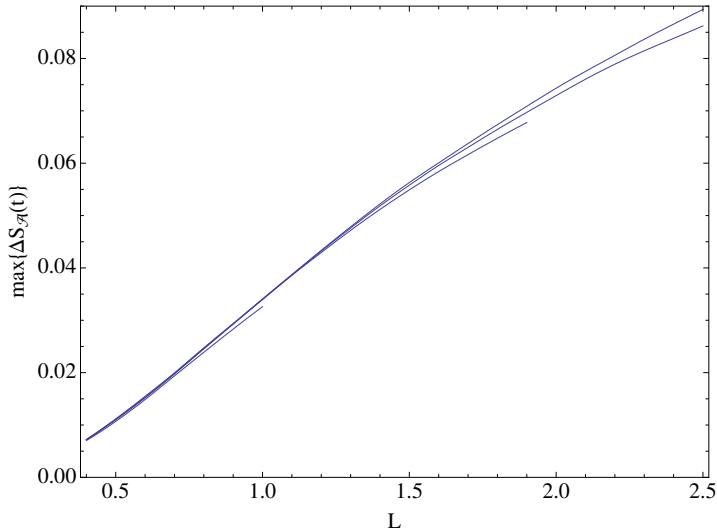


Figure 3.6: Maximum of the entanglement entropy $S_{\mathcal{A}}(t)$ as a function of L , for a range of masses of the initial black hole $M = \{0.005, 0.01, 0.02, 0.1\}$, starting from the top, and $\alpha = 0.1$. Lowering the temperature (decreasing M) slightly increases the maximum of $S_{\mathcal{A}}(t)$. The same phenomena is observed for $\alpha = 0.2$.

found in [47], given by

$$v_E^*(3) = \frac{(\eta - 1)^{\frac{1}{2}(\eta-1)}}{\eta^{\frac{1}{2}\eta}} \Big|_{d=3} = \frac{\sqrt{3}}{2^{\frac{4}{3}}} = 0.687, \quad \text{with } \eta = \frac{2(d-1)}{d}. \quad (3.32)$$

We note that temperature does not seem to have an effect on v_E , which is consistent with the above formula. For these parameters, the evolution is described by linear response to good approximation, and in that regime the tsunami velocity seems to capture the spatial propagation of entanglement to very good accuracy.

This behaviour should be anticipated on physical grounds. When the region \mathcal{A} is completely immersed in the quench source, we are back to the case where we may approximately think of the situation as a global quench problem. The fact that the source is not homogeneous in \mathcal{A}^c is irrelevant because all that matters is that the excitations produced by the quench

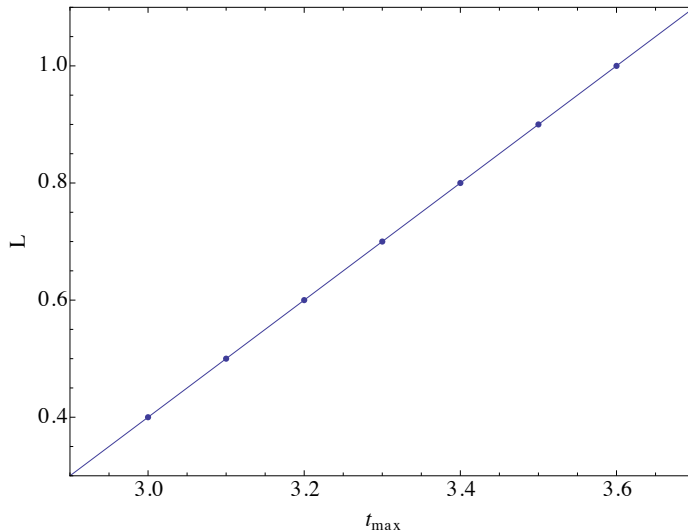


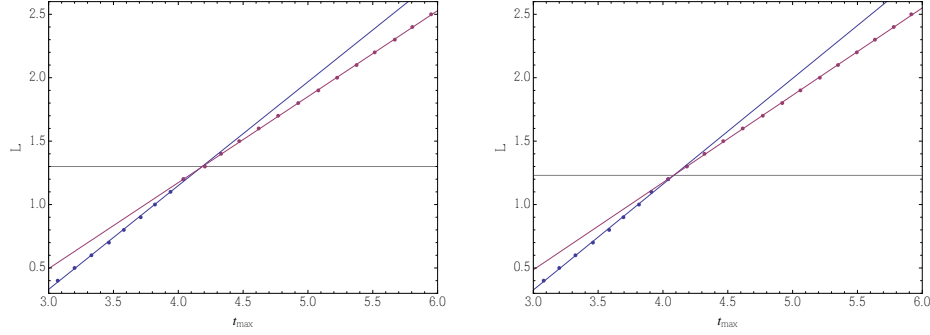
Figure 3.7: Position of the maximum of $S_{\mathcal{A}}(t)$ in the $L-t$ plane for a quench described by $\alpha = 0.5$, $M = 0.1$. The light-cone velocity extracted from the slope of this line is $v_{\text{LC}} = 1$, and is independent of the value of α .

are in the causal past of the entangling surface $\partial\mathcal{A}$. With this in mind we immediately anticipate that the results for the Vaidya quench explore in [47, 61] should apply and one see a linear growth with the tsunami velocity.

The story of the local quench however should be a lot richer than the homogeneous global quench. For one, we can encounter an interplay between the size of \mathcal{A} and the width of the pulse. We also expect that the non-linearities of gravity will play a role as we try to increase the amplitude. Indeed we see that velocity v_E increases as we increase the strength of the non-linearities in the bulk evolution – this is illustrated in Figs. 3.9a and 3.9b (where the scalar field amplitude was doubled from 0.1 to 0.2). This goes against the idea of the tsunami velocity as an upper bound on the speed propagation of the entanglement propagation, at least when that evolution is spatially resolved. Coupled with the earlier observation regarding the upper bound on $v_E \leq 1$, we find it natural to conjecture that

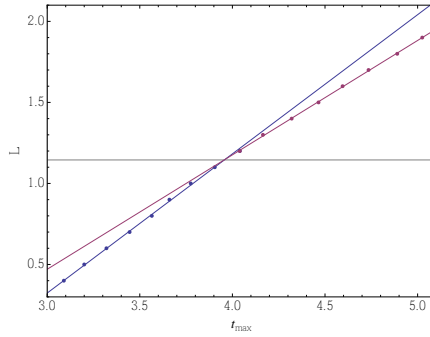
$$v_E^*(3) = 0.687 \leq v_E \leq 1 \quad (3.33)$$

The details of deviation from the two extreme limits appear to depend on



(a) $M = 0.005$, $v_E = 0.678(0.818)$

(b) $M = 0.01$, $v_E = 0.688(0.834)$



(c) $M = 0.02$, $v_E = 0.706(0.859)$

Figure 3.8: Position of the maximum of $S_{\mathcal{A}}(t)$ in the $L - t$ plane for a quenches described by $\alpha = 0.1$, starting from different initial states parameterized by M shown above. The light-cone velocities for large L for the three scenarios are also indicated, as are the corresponding values for small region sizes (in parenthesis). While we give the values of the velocity v_E for small regions, this data should be interpreted with care, for we typically find that edge effects contaminate the data, and these slopes should not be taken at face value in the small L regime.

various effects which we have not yet disentangled. While the upper bound follows from causality, it is unclear at present whether the tsunami velocity encountered (herein and before) is a fundamental bound on information processing in strongly coupled systems. It would be interesting to come up with a model which allows us to explore the different propagation velocities

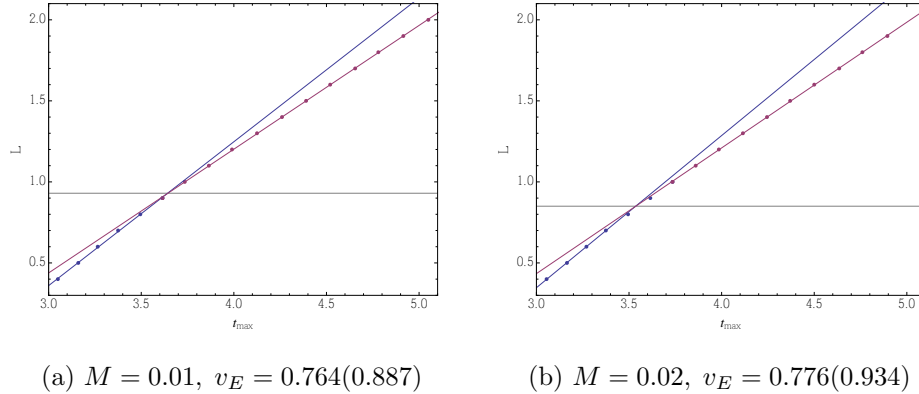


Figure 3.9: Position of the maximum of $S_{\mathcal{A}}(t)$ in the $L - t$ plane for a quenches described by $\alpha = 0.2$, starting from different initial states parameterized by M shown above. The light-cone velocities for large L for the three scenarios are also indicated. Conventions are the same as in Figure 3.8.

perhaps along the lines of [63].

3.4.2 Entanglement Decay

The process of return to equilibrium is characterized by universal behaviour and critical exponents. Therefore, an interesting quantity in our model is the decay of the entanglement entropy after it has reached a local maximum. To our knowledge this is the first time this decay has been calculated in either holographic theories or in higher dimensional conformal field theories.

From our numerical data we find that the profile for the decay is best fitted by an exponential damping

$$\Delta S_{\mathcal{A}}(t) \sim a_1 e^{-a_2(t-a_3)} + a_4, \quad (3.34)$$

where the parameters a_i depend on the specifics of the sources chosen to implement the quench protocol. In Figure 3.10 we depict the behaviour for a particular simulation (parameters in the caption). Note also the time delay in the initial growth, which illustrates the causality feature discussed earlier.

It is interesting to contrast our result for the exponential return to equilibrium against a more slow return seen in some spin chain models. For instance, in [130] the authors study free electrons in a half-filled chain and

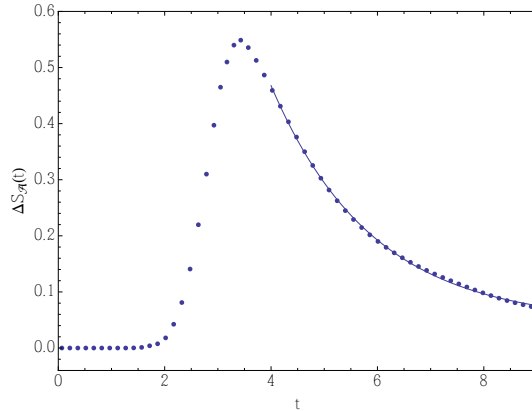


Figure 3.10: Exponential decay of the entanglement entropy evolution at late times; $\alpha = 0.5$, $M = 0.1$, $L = 0.8$. The fit parameters for the particular choice of quench parameters turns out to be $a_1 = 2.5335$, $a_2 = 0.5277$, $a_3 = 0.6049$, and $a_4 = 0.0454$. Note that we evolve the solution for late but finite time, which explains why $a_4 \neq 0$. In the infinite time limit we expect $a_4 = 0$.

determined the growth and decay of the entanglement entropy after a local quench. In that set-up they find a very slow return to the unperturbed value. In two dimensions the decay is characterized by $S_{\mathcal{A}}(t) \sim \frac{a_1 \log(t) + a_2}{t}$ as $t \rightarrow \infty$. The parameters a_1, a_2 are again obtained by fitting and depend on the specific details of the quench.

It is somewhat intriguing that the holographic computations relax much faster. This is reminiscent of features of scrambling in black hole physics, which we comment on in our discussion §3.5.

3.5 Conclusions and Future Directions

The main focus of the present paper was to describe the dynamics of the holographic entanglement entropy following a local quench. While this problem has been studied in the past using various known exact solutions to model the quench, we have carried out a full numerical simulation of Einstein's equations in the presence of a perturbing external source on the boundary of AdS. Given the explicit numerical solution to the quench geometry, we can study the dynamics of entanglement entropy by exploring

the behaviour of extremal surfaces that are anchored on the boundary.

The upshot of our analysis was a clear signal that entanglement entropy disperses linearly, in a manner reminiscent of the Lieb-Robinson light-cone. The dispersion velocity appears to depend on the details of the quench, though we were able to bound the result between two interesting bounds that have been discussed in the literature earlier. On the one hand we found that for wide quench profile, the propagation speed saturated a putative lower bound, given by the entanglement tsunami velocity obtained by [47] in the context of global quenches (modeled using the Vaidya-AdS spacetime). On the other hand well localized quenches appear to propagate entanglement at the speed of light. It is rather curious that we have results very similar to the Vaidya-AdS quench, for the geometry we construct is not the same. This lends support to thesis of [47, 61] that the holographic tsunami velocity ought to be a generic phenomenon.

The second aspect of holographic entanglement entropy which is interesting in our study is the rather rapid reversion of result to the equilibrium value. In various simulations we have tested, the reversion is exponentially fast, in contrast to the much slower logarithmic decay seen in spin models. This suggests again, as has been suspected in the past, that black holes are very efficient at information processing, cf., [131, 132].

There are many other interesting areas for further investigation. It would be interesting to study other quench protocols and other theories, including massive models, primarily to extract a more detailed dependence of the entanglement velocity and the rate of equilibration. A particularly interesting direction is the study of (global and local) quenches past critical points, generalizing the results of [133] to higher dimensions. It would also be interesting to study other non-local measures besides the entanglement entropy, which are more sensitive to the spatial structure of entanglement in quantum field theory, and to the differences between strongly coupled holographic CFTs and CFTs of small central charge. In particular, the mutual information of disjoint intervals would be interesting to calculate in our setup for local quenches. Finally, one can make a direct connection to the study of entanglement entropy following a local quench in two-dimensional CFTs, for which we have analytic results to explain the behaviour at large central charge [124]. We hope to report on these results in the near future [134].

Chapter 4

Comments on Entanglement Propagation

We extend our work on entanglement propagation following a local quench in 2+1 dimensional holographic conformal field theories. We find that entanglement propagates along an emergent lightcone, whose speed of propagation v_E seems distinct from other measures of quantum information spreading. We compare the relations we find to information and hydrodynamic velocities in strongly coupled 2+1 dimensional theories. While early-time entanglement velocities corresponding to small entangling regions are numerically close to the butterfly velocity, late-time entanglement velocities for large regions show less regularity. We also generalize and extend our previous results regarding the late-time decay of the entanglement entropy back to its equilibrium value.

4.1 Introduction

The generation and propagation of quantum information is a fascinating subject, bringing together insights from quantum information theory, many-body physics and perhaps most surprisingly, studies of the quantum mechanics of black holes. Here we focus on entanglement as a measure of quantum information.

One way to generate entanglement is by quenching the system, i.e. starting the evolution from an atypical excited state of the Hamiltonian, usually generated as the ground state of another, closely related Hamiltonian. The quenching process generates short range entanglement which then evolves and propagates as the system reaches the typical, thermal state¹.

¹We note in passing that much of the work on holographic quenches has been done at finite temperature, for example quenching past thermal critical points. Such studies mix quantum entanglement and classical correlations. To directly probe the quantum entanglement of the ground state one needs to work at zero temperature, for example quenching past quantum critical points. While some work in that direction has been done, much more remains to be explored. On the holographic side, the bulk geometry at zero temperature does not involve a regular horizon, which makes both the mechanics and physics quite different from the thermal case.

In the holographic context, quenching the system can be achieved by starting at equilibrium and turning on external sources (non-normalizable modes) for marginal or relevant operators, which drive the system out of equilibrium for a finite duration of time. Much attention has been given to global, i.e. spatially homogeneous, quenches. In this case the time-dependence of the entanglement entropy is the observable of interest, and many insights have been gained both in the holographic context, as well as in more traditional approaches to many body physics. Models of entanglement evolution, based on those results, are put forward in [47, 61, 63, 135, 136]. It would be interesting to incorporate the spatially-resolved holographic results, discussed here and in [137], into such models.

Indeed, the setup of local quenches, whereby the system is excited locally in the spatial domain, provides a spatially-resolved probe of the generation and propagation of entanglement. In [137] we initiated the study of such quenches, and here we continue that study in a more general set of holographic theories involving a charged black hole horizon, corresponding to strongly coupled conformal field theories in 2+1 dimensions at finite charge density. We focus on testing our previous results concerning entanglement propagation in this more general, yet quite similar, context. We are thus able to generalize and improve our original discussion, to test which of our previous results are robust, and to investigate which of our conjectures hold in a more general context².

Similarly to our previous work, we find that entanglement propagation defines an emergent lightcone structure for the theory. The maximal value of entanglement defines a lightcone, except for narrow transition regimes. We typically find two associated lightcone velocities, one to do with short times, and one with longer times³. The associated lightcone velocity v_E in those regimes depends on various parameters, and we have previously found some regularities in the neutral quenches.

Here we extend that analysis: we find that the early-time velocity seems to be related to the butterfly velocity, while late-time velocities have more complicated phenomenology. We discuss the phenomenology of v_E in this more general setup, and compare our results to other measures of entanglement propagation in that regime. We also discuss the return of the entanglement entropy to its equilibrium value, where we are able to give more precise results than previously due to improved numerics.

²This is similar in spirit to [138, 139], where it was found that breaking conformal invariance has only a limited effect on holographic results.

³Due to numerical limitations, these not asymptotically long times.

The outline of this paper goes as follows: In Section 4.2 we discuss our setup for local quenches in charged spacetimes, our numerical integration strategy using the characteristic formulation of general relativity, and our holographic calculation of the extremal surfaces encoding the entanglement entropy of regions on the boundary. Section 4.3 contains analysis of the dynamics of holographic entanglement entropy. We continue our investigation of the emergent lightcone structure that encodes the spatial propagation of entanglement entropy, by including the effects of charge and discussing various mechanisms that may underlie the phenomenology of entanglement dynamics. We also extend our description of entanglement thermalization, for which an improved numerical implementation of the quenches' evolution at late times reveals a logarithmic return to equilibrium rather than an exponential damping. We provide a brief summary of our results in Section 4.4 as well as further details on the numerical aspects of this work in Appendix B.

4.2 Holographic Local Quenches

In this section we introduce our setup for local quenches in charged spacetimes. The local quench is generated by an inhomogeneous scalar source which is turned on for a finite duration. The resulting bulk solution is found numerically, and the extremal surfaces in that geometry encode the dynamics of the entanglement entropy. Here we describe that setup, before turning to the results in the next section. We focus mostly on differences from [137], and the reader may wish to consult that reference for additional details.

4.2.1 Setup for Charged Quenches

We choose our metric to be a generalization of the infalling Eddington-Finkelstein coordinates for black holes in an asymptotically AdS₄ spacetime [73, 140]

$$ds^2 = -2A e^{2\chi} dt^2 + 2e^{2\chi} dt dr - 2F_x dt dx + \Sigma^2 (e^B dx^2 + e^{-B} dy^2), \quad (4.1)$$

and we introduce a gauge field V in the radial gauge

$$V = V_0 dt + V_x dx. \quad (4.2)$$

The coordinate r denotes the radial bulk coordinate, with the boundary located at $r = \infty$, and t is a null coordinate that coincides with time on

the boundary. Our quench, controlled by a relevant scalar on the boundary, will have local support in x while being translationally invariant in the y direction. Hence all the fields under consideration depend only on the coordinates $\{r, t, x\}$ with ∂_y being an isometry.

This null slicing of spacetime, known as the characteristic formulation, is well adapted to treat gravitational infall problems since the coordinates remain regular everywhere as the quench propagates through the bulk. Our ansatz also provides us with a residual radial diffeomorphism

$$r \rightarrow \bar{r} = r + \lambda(x^\mu), \quad (4.3)$$

which we use to fix the coordinate location of the apparent horizon and thus keep the computational domain rectangular.

The Einstein-Maxwell equations in the presence of a scalar field are given by

$$R_{MN} - \frac{R}{2}G_{MN} - \frac{3}{\ell_{\text{AdS}}^2}G_{MN} = T_{MN}^\Phi + T_{MN}^V, \quad (4.4)$$

$$\nabla_M F^{MN} = 0 \quad (4.5)$$

where the matter stress tensors are given by

$$T_{MN}^\Phi = \nabla_M \Phi \nabla_N \Phi + G_{MN} \mathcal{L}_\Phi, \quad \mathcal{L}_\Phi = -\frac{1}{2} (G^{MN} \nabla_M \Phi \nabla_N \Phi + m^2 \Phi^2), \quad (4.6)$$

$$T_{MN}^V = G^{AB} F_{MA} F_{NB} - \frac{1}{4} F^2 G_{MN}, \quad F = dV. \quad (4.7)$$

Before the quench, the spacetime geometry obeys the vacuum Maxwell-Einstein equations and is described by the RNAdS₄ black hole of mass M and charge Q

$$ds^2 = -r^2 f(r) dt^2 + 2 dt dr + r^2 (dx^2 + dy^2), \quad f(r) = 1 - \frac{M}{r^3} + \frac{Q^2}{2r^4}, \quad (4.8)$$

and the time-component of the gauge field is

$$V_0 = \mu - \frac{Q}{r}, \quad \mu \equiv \frac{Q}{r_+}. \quad (4.9)$$

The chemical potential μ is chosen so that V_0 vanishes at the event horizon. In fact, RN black holes typically possess two horizons r_\pm , which correspond

to the two real solutions of $f(r) = 0$. The black hole's Hawking temperature is given by

$$T = \frac{r_+^2 f'(r_+)}{4\pi}, \quad (4.10)$$

and extremality occurs when $T = 0$, i.e. when $Q = \sqrt{3Mr_+/2}$ and the two horizons coincide.

4.2.2 Asymptotic Analysis

We now turn our attention to the asymptotic behaviour of our system. We first make a simplifying choice and take $m^2 \ell_{\text{AdS}}^2 = -2$ in order to ensure that the near-boundary expansion of the bulk scalar field is in integer powers of $1/r$

$$\Phi(r, t, x) = \frac{\phi_0(t, x)}{r} + \frac{\phi_1(t, x)}{r^2} + \dots \quad (4.11)$$

Requiring that the Einstein-Maxwell equations in the presence of Φ are satisfied as $r \rightarrow \infty$ informs us that the gauge field behaves like

$$V_0(r, t, x) = \mu(t, x) - \frac{\rho(t, x)}{r} + \dots \quad (4.12)$$

$$V_x(r, t, x) = \mu_x(t, x) + \frac{j_x(t, x)}{r} + \frac{V_x^{(2)}(t, x)}{r^2} \dots \quad (4.13)$$

whereas the metric components have the asymptotic expansion

$$A(r, t, x) = \frac{(r + \lambda(t, x))^2}{2} - \partial_t \lambda(t, x) - \frac{1}{4} \phi_0(t, x)^2 + \frac{a^{(3)}(t, x)}{r} + \dots \quad (4.14)$$

$$\chi(r, t, x) = \frac{c^{(3)}(t, x)}{r^3} + \dots \quad (4.15)$$

$$F_x(r, t, x) = -\partial_x \lambda(t, x) + \frac{f^{(3)}(t, x)}{r} + \dots \quad (4.16)$$

$$\Sigma(r, t, x) = r + \lambda(t, x) - \frac{1}{4} \phi_0(t, x)^2 + \dots \quad (4.17)$$

$$B(r, t, x) = \frac{b^{(3)}(t, x)}{r^3} + \dots \quad (4.18)$$

The functions $G_{\mu\nu}^{(3)}$ are undetermined by the equations of motion and require the input of boundary data via the stress tensor $T_{\mu\nu}$ [13], defined in its

Brown-York form as [141]

$$T_{\mu\nu} = K_{\mu\nu} - K\gamma_{\mu\nu} + 2\gamma_{\mu\nu} - \left(\gamma R_{\mu\nu} - \frac{1}{2} \gamma R \gamma_{\mu\nu} \right) + \frac{1}{2} \gamma_{\mu\nu} \phi_0^2, \quad (4.19)$$

where $\gamma_{\mu\nu}$ is the induced metric on the boundary, $K_{\mu\nu}, K \equiv \gamma^{\mu\nu} K_{\mu\nu}$ its extrinsic curvatures, and $\gamma R_{\mu\nu}, \gamma R$ its intrinsic curvatures. It is straightforward to show that

$$T_{00} = 2a^{(3)} + 4c^{(3)} + \phi_0 \phi_{\text{response}}, \quad (4.20)$$

$$T_{tx} = \frac{3}{2} f^{(3)} - \frac{1}{2} \phi_0 \partial_x \phi_0, \quad (4.21)$$

and that these components obey the conservation equations

$$\partial_t T_{00} = \partial_x T_{tx} + \partial_t \phi_0 \phi_{\text{response}} - (\partial_t \mu_x - \partial_x \mu)^2 - j_x (\partial_x \mu - \partial_t \mu_x), \quad (4.22)$$

$$\begin{aligned} \partial_t T_{tx} = & \frac{1}{2} \left(\partial_x T_{00} - 3 \partial_x b^{(3)} + \partial_x \phi_0 \phi_{\text{response}} - \phi_0 \partial_x \phi_{\text{response}} \right) \\ & + \rho (\partial_x \mu - \partial_t \mu_x). \end{aligned} \quad (4.23)$$

In addition to energy and momentum, the electric charge and current are also conserved

$$\partial_t \rho = -j_x - \partial_x^2 \mu + \partial_t \partial_x \mu_x, \quad (4.24)$$

$$\partial_t j_x = V_x^{(2)} + j_x \lambda - \frac{1}{2} \partial_x \rho. \quad (4.25)$$

4.2.3 Integration Strategy

The characteristic formulation of the Maxwell-Einstein and Klein-Gordon equations conveniently reorganizes the coupled PDEs in two simpler categories: equations for auxiliary fields that are local in time and that obey nested radial ODEs, and equations for dynamical fields that propagate the geometry from one null slice to the next [73, 140]. Here we outline our numerical integration strategy, and refer the reader to Appendix B for a discussion on the more technical aspects of our implementation.

We modelled the quench source function as $\phi_0(t, x) = f(x)g(t)$, with

$$f(x) = \frac{\alpha}{2} \left[\tanh \left(\frac{x + \sigma}{4s} \right) - \tanh \left(\frac{x - \sigma}{4s} \right) \right], \quad g(t) = \text{sech}^2 \left(\frac{t - t_q \Delta}{t_q} \right). \quad (4.26)$$

We let the scalar field profile reach a maximum value α at time $t = t_q \Delta$. We set $t_q = 0.25$ and $\Delta = 8$, and chose the steepness s according to the width σ of the perturbation in order to have a smooth profile. By $t = 3$, $\phi_0 \approx 0$, and the quench has concluded.

We performed domain decomposition in the radial direction, using 4 domains each discretized by a Chebyshev collocation grid containing 11 points. In doing so, errors located near the boundary or near the apparent horizon remain localized within their respective subdomain [127], thus improving the solutions for auxiliary fields over the entire radial domain. We discretized the spatial direction using a uniformly-spaced Fourier grid over the interval $[-30, 30]$ and used 121 points for $\sigma = 2$, and 173 points for $\sigma = 0.5$ to maintain an acceptable spatial resolution as the quench profile propagates further away at later times.

As for the time evolution, we used an explicit fifth-order Runge-Kutta-Fehlberg (RK5) method with adaptive step size to propagate dynamical quantities. Note that we evolved each quench until $t = 20$, the approximate time at which the fields perturbations reach the spatial boundaries. We also got rid of high-frequency modes that contaminated our solutions by applying a smooth low-pass filter that discarded the top third of the Fourier modes. However, we remark that it is important not to filter the bulk scalar field Φ if we want its RK5-propagated boundary profile to agree with the source ϕ_0 at all times.

4.2.4 Holographic Entanglement Entropy

The next step after obtaining numerical solutions for our local quench is to study the evolution of the holographic entanglement entropy (HEE) of a region \mathcal{A} on the boundary. For simplicity, we consider a strip that extends infinitely in the y direction

$$\mathcal{A} = \{(x, y) \mid x \in (-L, L), y \in \mathbb{R}\}, \quad \partial\mathcal{A} = \{(x, y) \mid x = \pm L, y \in \mathbb{R}\}. \quad (4.27)$$

The covariant HEE prescription [41] tells us that the entanglement entropy is determined by the area of extremal surfaces anchored on $\partial\mathcal{A}$. It is natural to use the quench's translational invariance to parametrize the extremal surfaces by the coordinates τ and y . The extremal surfaces we are looking for will also be translationally invariant in y , and the problem of calculating their area reduces to that of calculating the proper length of the geodesics

$X^M(\tau) = \{t(\tau), r(\tau), x(\tau)\}$ arising from the Lagrangian

$$\mathcal{L} = G_{yy} G_{MN} \dot{X}^M \dot{X}^N. \quad (4.28)$$

The resulting system of 3 second order ODEs can be transformed into a system of 6 first order ODEs in the variables

$$\{t, P_t \equiv \Sigma^2 \dot{t}, r, P_+ \equiv e^{2\chi} (\dot{r} - A \dot{t}), x, P_x \equiv \Sigma^2 \dot{x} - e^{-B} F_x \dot{t}\}, \quad (4.29)$$

for which $\mathcal{L} = 2P_+ P_t + P_x^2$.

Keeping in mind that the length of a geodesic in an asymptotically AdS spacetime is formally infinite, we introduce a UV cutoff $r = \epsilon^{-1}$ and use a regularization scheme in which we subtract the entanglement entropy of a RNAdS₄ geometry expressed with the radial coordinate $\bar{r} = r + \lambda(t, x)$, thus effectively matching asymptotic coordinate charts in both setups and setting $\Delta S_{\mathcal{A}} = 0$ prior to the quench⁴.

To solve the Euler-Lagrange equations derived from (4.28), we adopt an initial value problem point of view in which the initial conditions at the turning point are

$$\{t = t^*, P_t = 0, r = r^*, P_+ = 0, x = 0, P_x = \pm 1\}, \quad (4.30)$$

and we use a shooting method in r^* so that $x = L$ when $r = \epsilon^{-1}$. Note that the tolerance parameters of the ODE solver must be chosen so that $\mathcal{L} = 1$ along the geodesic, which in turn provides us with a safety check for our solutions.

4.3 Results

Having described our setup and methods of calculation, we now turn to summarizing the patterns observed in our extended framework. In each case, we provide context by starting our discussion with a brief reminder of our observations for neutral local quenches before broadening the scope of our analysis to account for the effects of charge.

⁴This regularization procedure is equivalent to subtracting the vacuum entanglement entropy for the region \mathcal{A} with a dynamical cutoff $\epsilon_{\text{vac}}(t, x)$ related to the radial shift $\lambda(t, x)$.

4.3.1 Emergent Lightcone and Entanglement Velocity

Entanglement lightcone

The local nature of the quenches (having finite energy at infinite volume, i.e. zero energy density) implies that the entanglement entropy of any region \mathcal{A} initially grows with time, reaching a maximum, before inevitably decaying to its pre-quench value as the perturbation dissipates away. Much of our analysis has to do with the spatial structure of that maximum, as a function of the spatial extent L of \mathcal{A} and the time t . We find that, except for narrow transition ranges, the curve traced by the maximum in the $L - t$ plane is linear: the spatial propagation of entanglement defines a new lightcone structure, distinct from the causal structure of both bulk and boundary theories.

We note that a similar observation was made in [104], in which local quenches are implemented as a perturbative approximation to the backreaction caused by a massive infalling particle in pure AdS. In that context, the trajectory traced by $\Delta S_{\mathcal{A}}(t_{\max}, L)$ in the $L - t$ plane always follows a slope of $v_E = 1$ (additionally, the amplitude of that maximum remains constant throughout).

It turns out that the structure of our results is much richer since our numerical scheme accounts for the full backreaction of the quench on the geometry. While our data reveals the appearance of an emergent lightcone, this result emerges from the analysis rather than being one of the assumptions put in by hand. Indeed, as we will detail below, we typically find two linear regimes separated by a narrow transition, with distinct velocities at early and late times.

The slope of the curve traced by the maximum, v_E , is a natural measure of how fast entanglement propagates spatially. Much of our analysis has to do with analyzing this velocity v_E . We find a rich structure in the dependence of the emergent lightcone velocity on parameters. In particular, while it is conceptually similar to other measures of quantum information spreading such as the butterfly or tsunami velocities, we find that it is numerically distinct from them under most circumstances.

Let us now turn to describing the regularities found in the entanglement velocity v_E .

Entanglement velocity

As is expected from a relativistic theory, we found that v_E was bounded from above by the speed of light, with the bound being saturated universally in the high temperature regime.

Perhaps more interesting was the discovery of a lower bound on v_E different from the speed of sound of a three-dimensional CFT, $v_{\text{sound}} = 1/\sqrt{2} = 0.707$. Indeed, the speed of sound, which underpins the thermalization of energy and momentum on the boundary theory, seemed a likely candidate to track the generation and propagation of entanglement. However, our initial analysis showed that this lower bound lied slightly below v_{sound} , and in fact was consistently very close to $v_E^*(3)$, the tsunami velocity of a Schwarzschild-AdS₄ black hole [47]

$$v_E^*(d=3) = \left. \frac{(\eta-1)^{\frac{1}{2}(\eta-1)}}{\eta^{\frac{1}{2}\eta}} \right|_{d=3} = \frac{\sqrt{3}}{2^{\frac{4}{3}}} = 0.687, \quad \text{with } \eta = \frac{2(d-1)}{d}. \quad (4.31)$$

The tsunami velocity is a holographic measure of how fast entanglement propagates spatially when spacetime is globally quenched and depends uniquely on a black hole's conserved charges. Given the naturalness of this velocity in matters related to entanglement entropy propagation, we conjectured that v_E should be found within the bounds

$$v_E^*(3) = 0.687 \leq v_E \leq 1. \quad (4.32)$$

This situation is in a way reminiscent of quantum spin systems, which admit an upper *Lieb-Robinson* bound on the speed at which information can travel despite the absence of relativistic constraints [129]. However our holographic calculation also provides us with an unexpected lower bound on information processing based on the properties of spacetime itself.

We now extend our analysis of the structure of the entanglement lightcone and the velocity v_E by including the effects of charge. Our main result persists: in all the cases we examined, the entanglement traces a lightcone structure. We can therefore look more closely at the relation between the entanglement propagation velocity v_E defined by our emergent lightcone structure, and other closely related velocities. We note that while those velocities are conceptually similar, and numerically close to each other for neutral black holes, their dependence on charge is distinct. We can therefore hope to make better distinction between them by examining our results for different parameter ranges, in particular focussing on the charge dependence.

Relation to other velocities

In our simulations for wide quenches we find two stages for entanglement propagation, both exhibiting a lightcone structure, and a narrow transition regime between them. For the early-time results, governing the evolution of small entangling surfaces, it is natural to suspect some relation to the butterfly velocity, quantifying the spatial spread of chaos [142–144]. We note that the presence of charge does not affect its value: $v_{\text{butterfly}} = \sqrt{3}/2 = 0.866$.

Indeed, this velocity seems to play a role in our results for the spatial propagation of entanglement entropy: early-time velocities are in the range $v_E \in [0.8, 0.9]$, numerically close to the butterfly velocity. In fact, it was shown that the butterfly velocity naturally characterizes the saturation time for large strip regions in the case of global quenches [145]. Since the $L < \sigma$ regime under consideration approximates a global quench for which t_{max} can be thought of as the saturation time’s counterpart, $v_{\text{butterfly}}$ seems a likely candidate to quantify the initial spread of quantum information that we observe.

For the late-time velocities, governing the evolution of larger entangling surfaces, we had previously found a relation to the tsunami velocity, which appears as a lower bound of entanglement propagation in the neutral case. It turns out that the tsunami velocity of RNAdS₄ black hole decreases as its charge increases, ultimately vanishing at extremality. If the tsunami velocity serves as a lower bound for all values of the charge, then the addition of charge should change the measured slopes v_E in a predictable way. In particular, we should find that the spatial propagation of the entropy significantly slows down near extremality.

Note however a subtle order of limits issue. Our numerics, performed outside the apparent horizon, are restricted to sufficiently narrow entangling surfaces. This is sufficient for discovering the emergent lightcone structure, which we investigate here. However, the asymptotic IR limit $L \rightarrow \infty$ is a priori distinct and may exhibit different regularities. In particular, even in the extremal limit, the entangling surfaces relevant for the emerging lightcone are not deformed much in the near-horizon region. It may be the case that infinitely wide surfaces are more sensitive to the near-horizon geometry, and thus exhibit a more dramatic behaviour in the near-extremal limit.

As it turns out, the inclusion of charge does not affect our results in a dramatic way, in this regime. Figure 4.1 shows the small effect charge has on the lower bound for entanglement propagation speeds; the slopes v_E all fall within the same range for all charged configurations. In the case where

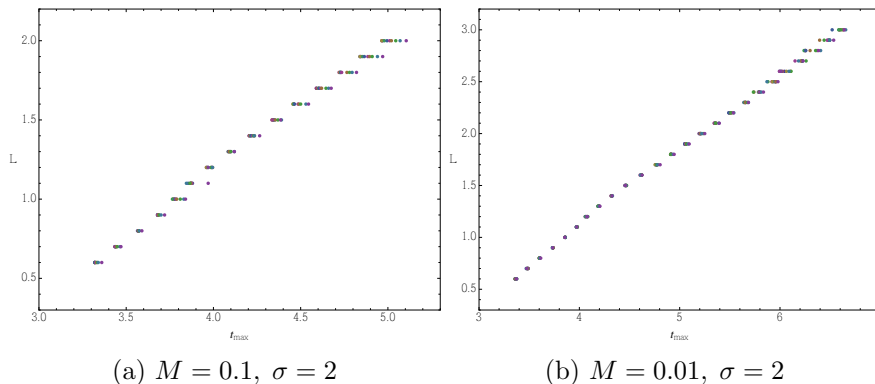


Figure 4.1: The curves traced by the maximum of $\Delta S_{\mathcal{A}}(t)$ in the $L-t$ plane. Note that all charged configurations have been included in the same figure to illustrate the weak dependence of the lightcone behaviour with respect to charge. In both cases, the early-time velocities are found in close proximity to the butterfly velocity ($v_E \in [0.8, 0.9]$), whereas the late-time velocities are found within $v_E \in [0.65, 0.71]$, an interval containing various velocities of interest.

the minimal surfaces can penetrate deeper in the bulk, we still observe two linear regimes (as in Fig. 4.1b) corresponding approximately to $L < \sigma$ and $L > \sigma$. The tsunami velocity originally appeared in the large L limit, and we observe that charge only marginally decreases the slope v_E .

The range of the lightcone velocities found at large L in our simulations, $v_E \in [0.65, 0.71]$, is also fairly close to other hydrodynamic velocities: $v_{\text{sound}} = 0.707$ and $v_{\text{shear}} = 0.665$. The latter is obtained from second-order hydrodynamics results interpreted in terms of the phenomenological Muller-Israel-Stewart theory. This shear velocity, which encodes the velocity of the wavefront of momentum relaxation, is defined as [146]

$$v_{\text{shear}} = \sqrt{\frac{D_\eta}{\tau_\Pi}} \approx 0.665, \quad (4.33)$$

where D_η is the effective shear “diffusion” constant obtained from an analysis of the sound pole, and the hydrodynamic parameter τ_Π is the shear relaxation time, which can be calculated from AdS/CFT [147]

$$D_\eta = \frac{1}{4\pi T}, \quad \text{and} \quad \tau_\Pi = \frac{3}{4\pi T} \left[1 - \frac{1}{2} \left(\log 3 - \frac{\pi}{3\sqrt{3}} \right) \right]. \quad (4.34)$$

As this velocity has to do with entropy production, it can naturally affect the evolution of holographic entanglement entropy in our setup.

In summary, it remains unclear exactly what phenomena come into play to influence entanglement propagation in the late-time regime, where we find an emergent lightcone. On one hand, we have seen that the slope traced by $\Delta S_{\mathcal{A}}(t_{\max}, L)$ does not decrease as we approach extremality, which suggests that the charged tsunami velocity does not provide an appropriate description of the lower bound for v_E . Additionally, our analysis remains inconclusive as to the relevance of the neutral tsunami velocity $v_E^*(3)$. We also see that the entanglement velocity is fairly close to hydrodynamical velocities, related to entropy production. As such we are unable to disentangle the various effects which may influence entanglement propagation, and it is entirely possible that different mechanisms may compete to influence the shape of the entanglement lightcone in the late-time regime, resulting in the variations observed in v_E .

4.3.2 Entanglement Maximum

In the neutral case, we found that the value of the entanglement entropy maximum $\Delta S_{\mathcal{A}}(t_{\max})$ increased linearly with the size L of the entangling region for small L . This increase was also quantified as a function of the scalar source's maximal amplitude α

$$\frac{\partial}{\partial L} \Delta S_{\mathcal{A}}(t_{\max}, L; \alpha) \sim \alpha^2. \quad (4.35)$$

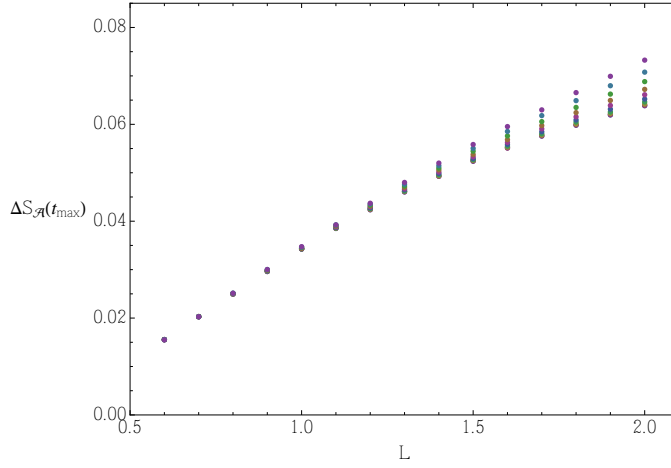
For fixed amplitudes, we observe that the maximum $\Delta S_{\mathcal{A}}(t_{\max})$ was not affected by the addition of charge for small L , and increased marginally when changing Q , even as we approach extremality (see Figure 4.2). Thus, our previously discovered regularities seem robust to the addition of charge.

4.3.3 Entanglement Decay

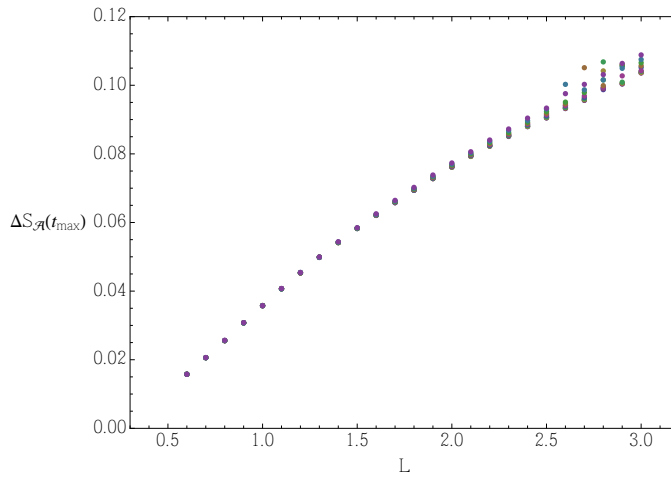
We now turn our attention to the late-time behaviour of holographic entanglement entropy. Our earlier work on neutral quenches showed evidence that the process of return to equilibrium was best described by an exponential damping

$$\Delta S_{\mathcal{A}}(t) = a_1 e^{-a_2(t-a_3)} + a_4. \quad (4.36)$$

The parameters a_i depended on the particular features of the quench but did not seem to follow any discernible pattern. However, our analysis was



(a) $M = 0.1, \sigma = 2$



(b) $M = 0.01, \sigma = 2$

Figure 4.2: The maximum of $\Delta S_{\mathcal{A}}(t)$ as a function of strip width L for $\alpha = 0.1$. Note that all charged configurations have been included in the same figure to illustrate the weak dependence of the entanglement entropy with respect to charge.

limited by the quality of our numerical quench solutions. In particular, the bulk fields could not be propagated past $t = 9$ without loss of accuracy at large x and large memory requirements. We managed to evolve the quenches up until $t = 20$ in a reasonable time by making a few modifications,

including increasing the spatial resolution by discretizing the x direction with a uniform Fourier grid and by solving the radial ODEs for the auxiliary fields independently for each discretized x_j .

These improvements allowed us to investigate the late-time behaviour of the entanglement entropy over much larger time intervals. This additional information revealed that the exponential decay we observed previously was due to fitting the late-time data over too short of a time interval. In fact, the new data instead suggests that

$$\Delta S_{\mathcal{A}}(t) \sim \frac{a_1 \log t + a_2}{t^\delta}, \quad (4.37)$$

is a much better fit, as illustrated in Figure 4.3. This result is more in line with those derived from spin chain models [130].

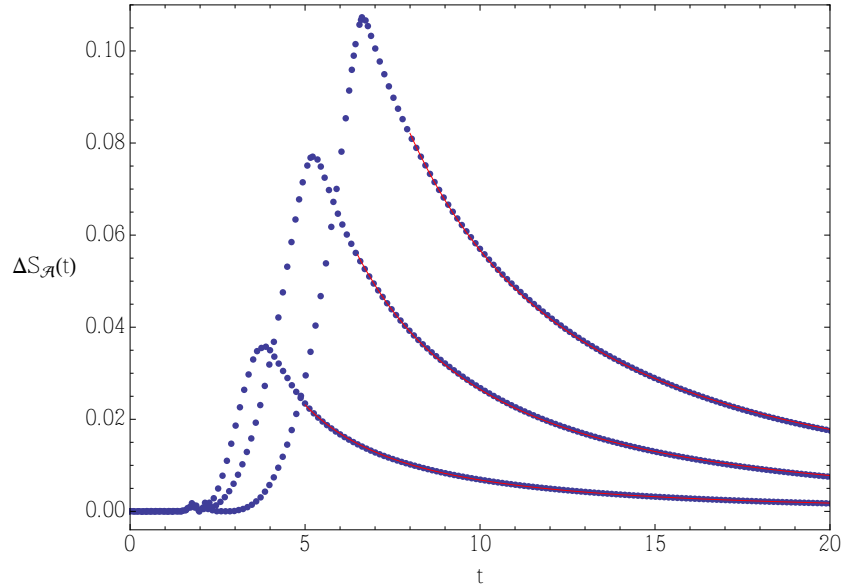


Figure 4.3: The late-time behaviour of the entanglement entropy closely follows the logarithmic decay (4.37) for $L = \{1, 2, 3\}$, from top to bottom, for $\alpha = 0.1$, $M = 0.01$, $\sigma = 2$ and $Q = 0.04$. In this particular case, the best fit exponents are, respectively, $\delta = \{1.36, 1.48, 1.49\}$.

Interestingly, the best-fit exponents δ , obtained by a least-square fit, are generally clustered around either $\delta = 1$ or $\delta = 1.5$, which marks a departure

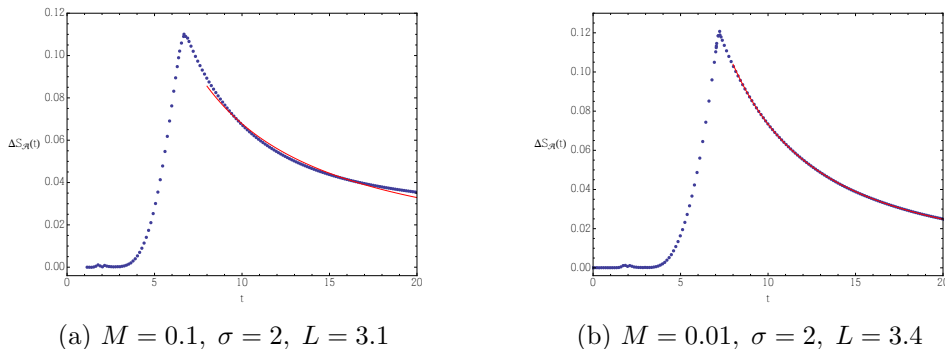


Figure 4.4: The decay of $\Delta S_{\mathcal{A}}(t)$ and its best logarithmic fit for $Q = 0.99 Q_{\text{ext}}$ and $\alpha = 0.1$. The sizes L have been chosen such that the extremal surfaces probe the near-horizon geometry at one point during the quench's evolution, i.e. L is taken as large as the quench allows it to be. We find $\delta = 1.5$ for the figure on the right.

from the prediction $\Delta S_{\mathcal{A}}(t) \sim t^{-6}$ made in the perturbative analysis of [104]. Our findings show that there is a complex interplay between the size L , the initial energy density M , the initial charge density Q , and the amount of injected energy in the characterization of entanglement entropy's return to equilibrium. When $M = 0.1$, the logarithmic decay fits the data with $\delta = 1.5$ at low Q and small L for both $\sigma = 0.5$ and $\sigma = 2$. However, (4.37) becomes a bad fit as either the charge and/or the size of \mathcal{A} are increased, as showcased in Figure 4.4a. We find that the breakdown occurs around $Q \sim Q_{\text{ext}}/2$.

In contrast, the logarithmic return to equilibrium fits the data for all values of Q and L when $M = 0.01$. When $\sigma = 0.5$, thermalization is dominated by $\delta = 1$ except for near-extremal black holes $Q = 0.99 Q_{\text{ext}}$, for which $\delta = 1.5$ no matter the size of the entangling surface. Taking $\sigma = 2$ reveals an even richer picture in which we observe a sharp transition between decays characterized by $\delta = 1$ and $\delta = 1.5$. As illustrated in Figure 4.5, the late-time evolution of holographic entanglement entropy in the neutral, large size limit is fitted best with $\delta = 1$. The exponent $\delta = 1.5$ appears either as extremality is approached, as in the $\sigma = 0.5$ case, or in the small L limit, as in the $M = 0.1$ case.

These observations lead us to believe that the late-time behaviour of $\Delta S_{\mathcal{A}}(t)$ is influenced not only by the parameters characterizing the geodesics and the geometry of the unquenched spacetime, but also by the amount of energy injected by the scalar quench. As such it is hard to disentangle

and generalize our findings when the underlying competing processes harbor inherently different length scales.

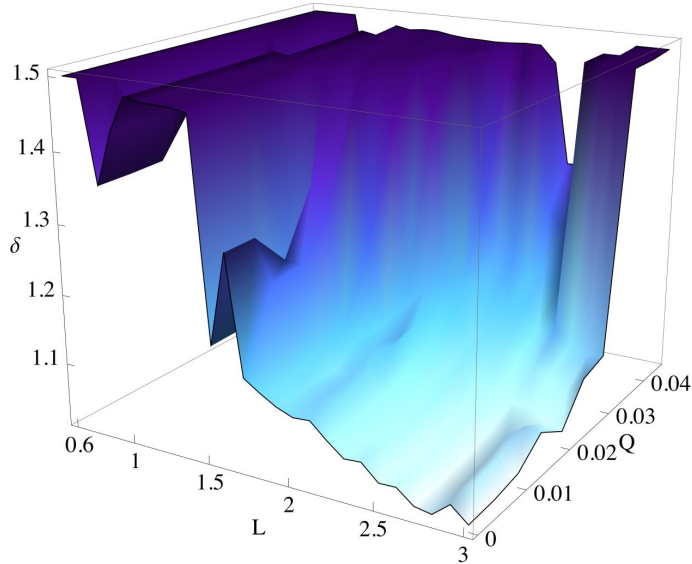


Figure 4.5: This figure illustrates the sharp transition between $\delta = 1$ and $\delta = 1.5$ in the logarithmic decay of the HEE as a function of Q and L for $M = 0.01$ and $\sigma = 2$.

4.4 Summary

We have studied the spatial propagation of entanglement entropy following a local excitation of the system. We find that the entanglement generically propagates along an emergent lightcone, whose velocity may change over a narrow transition regime. In our simulation we find early and late-time velocities, and look at their dependence on parameters and relation to other interesting information and hydrodynamical velocities.

The early-time entanglement velocity for small strips seems similar to the butterfly velocity. As both have to do with the initial propagation of quantum information, we find that relation plausible, especially as it mirrors an analytical result derived in an analogous global quench scenario. We are however unable to disentangle the various effects that could influence the late-time entanglement velocity: the propagation in that regime seems likely to be controlled by a combination of many mechanisms.

We are also able to exhibit some universality in the logarithmic return of the entanglement to its equilibrium value. In particular, the relation to known results for spin chains in 1+1 dimensional CFTs is intriguing.

There are very few avenues to investigate the propagation of quantum information in higher-dimensional strongly coupled conformal field theories. We hope that the phenomenology we present can illuminate that difficult subject: in particular it would be instructive to have a simple model incorporating the regularities we find in the holographic results. We hope to return to these issues in the future.

Chapter 5

On Brane Instabilities in the Large D Limit

Using an expansion in large number of dimensions, taken to subleading orders, we discuss several issues concerning the Gregory-Laflamme instabilities. We map out the phase diagram of neutral and charged black strings, and comment on the possible transition in the nature of the final state of the instability at higher order in the $1/D$ expansion. We also discuss unstable black membranes, and show that in certain limits the preferred shape of the non-uniform phase is a triangular lattice.

5.1 Introduction

Since its discovery, the Gregory-Laflamme instability [66, 67] has been a source of many insights into General Relativity and its extended black brane solutions in higher dimensions. The fate of the instability for a string is much studied (for a comprehensive review, see [148]): there is now strong evidence that the end-point of the black string instability depends on the number of spacetime dimensions. It was shown in [70] that there exists a critical dimension $D^* = 13.5$ above which non-uniform black strings (NUBS) become stable and have larger horizon areas than their uniform counterparts, thus making them natural candidates as the end-point of the GL instability. Below D^* , numerical simulations [69, 149] have presented evidence that black string horizons bifurcate in a self-similar cascade of black holes pinching off to arbitrary small scales along the string direction, thus violating the cosmic censorship hypothesis (despite the arguments proposed by [68]). A numerical evolution beyond the critical dimension would be a welcome addition, but the high-performance computing resources required would be an obstacle to this endeavour.

A different approach — general relativity in the limit where the number of dimensions is large [64] — offers a promising framework in which one can address such questions analytically, or numerically with only modest resources. Despite the theory being formally valid only when $D \rightarrow \infty$, its potential even at finite D was highlighted in a range of applications, ranging

from the striking agreement of large D black holes quasinormal modes for both large and small values of D , to the alternative derivation of the critical dimension D^* found in [72].

In this paper we discuss different aspects of the phase structure of the non-uniform black objects. Following in the footsteps of [71, 150], we perform our analysis by promoting the mass, charge and momentum densities on the string to be collective variables, and solve the resulting equations numerically, observing their conserved charges at asymptotic infinity. Using this approach, we discuss several issues concerning the end-state of the Gregory-Laflamme instability of extended black objects.

Discussing the general charged black string, we find that the entropy difference between the non-uniform configuration and its uniform counterpart remains finite and positive for all such charged black strings, even in the extremal limit. Indeed, in the extremal limit we are able to show that fact analytically. Thus we conclude that there is a second order transition to a non-uniform phase for all charged NUBS, which are entropically favoured despite the weakening of the GL instability due to the addition of electric charge.

We also investigate the physics of the neutral string to next-to-leading order (NLO). Our goal is to find the signal, in the large D expansion, of the transition of the instability end-point from a non-uniform black string to a pinch-off scenario. Indeed, below the critical dimension D^* where the NUBS have lower entropy than the uniform string, there is a different end-point to the instability, which is expected to be a pinch-off. While we find signs that this is indeed the case, we are unable to find a universal value for the associated critical dimension (which may be different from D^*) from our analysis.

Lastly, we turn our attention to the phase structure of two-dimensional unstable membranes on oblique lattices. By comparing brane solutions of different shapes, we find that the triangular lattice configuration is the one that minimizes the corresponding thermodynamic potential for localized 2-branes.

The outline of the paper is as follows: In Section 5.2, we summarize how to obtain charged (and neutral) black string solutions in the characteristic formulation of general relativity, at leading order in D . This serves to set up our notations and explains our numerical method. In Section 5.3, we discuss the phase structure of charged black string. To that end, we find the subleading corrections to the metric and gauge field, necessary to discuss the entropy difference (in the micro-canonical ensemble) between the uniform and non-uniform solutions. We find that a charged non-uniform string

always have a larger horizon area than uniform configurations, even in the extremal limit. We also obtain the equations governing the dynamics of the $1/D$ corrections to the mass and momentum densities, and discuss stability conditions of the neutral string to next-to-leading order, and the signals that there may be a transition to pinch-off as the final state as we lower D . Lastly, we explore the thermodynamics of unstable two-dimensional branes on general oblique lattices in Section 5.4. We find that the preferred shape of the lattice is triangular, up to small deviations, likely due to finite size effects.

5.2 Charged p -brane Solutions

We start our analysis by finding static charged black string solutions. Keeping in mind that we are interested in finding non-uniform black string solutions, we must allow redistribution of mass and charge to occur along the spatial direction. To this end, we introduce a local Galilean boost velocity and promote the mass and charge densities to vary along the string. We then solve the Einstein-Maxwell equations at leading and subleading orders, from which we extract the effective equations that describe the nonlinear fluctuations of the string horizon.

5.2.1 Uniformly Charged p -Branes

The equations of motion that charged, spherically symmetric p -branes satisfy in the limit where $D \rightarrow \infty$ can be obtained by considering the Einstein-Maxwell action in $D = n + p + 3$ dimensions,

$$I_{\text{EM}} = \int d^D x \sqrt{G} \left(R_G - \frac{F^2}{4} \right), \quad (5.1)$$

where $F = dV$ is a Maxwell potential. Performing dimensional reduction on (5.1) so that the metric becomes of the form

$$ds_G^2 = g_{\mu\nu}(x) dx^\mu dx^\nu + e^{\phi(x)} d\Omega_{n+1}^2, \quad (5.2)$$

where the coordinates $x^\mu = (t, r, z^A)$ span a $p + 2$ dimensional space, we obtain the action (see Appendix C for details)

$$I_{\text{EM}} = \int d^{p+2} x \sqrt{g} e^{\frac{(n+1)\phi}{2}} \left(R_g + n(n+1)e^{-\phi} + \frac{n(n+1)}{4} (\nabla\phi)^2 - \frac{F^2}{4} \right). \quad (5.3)$$

The equations of motion that follow from (5.3) are [151]

$$\begin{aligned}
R_{\mu\nu} - \frac{n+1}{2}\nabla_\mu\nabla_\nu\phi - \frac{n+1}{4}\nabla_\mu\phi\nabla_\nu\phi \\
- \frac{1}{2}\left(F_{\mu\alpha}F_\nu{}^\alpha - \frac{1}{2(n+p+1)}F^2g_{\mu\nu}\right) &= 0 \\
\nabla_\alpha F^{\alpha\mu} + \frac{n+1}{2}\nabla_\alpha\phi F^{\alpha\mu} &= 0 \\
n e^{-\phi} - \frac{n+1}{4}(\nabla\phi)^2 - \frac{1}{2}\nabla^2\phi + \frac{1}{4(n+p+1)}F^2 &= 0.
\end{aligned} \tag{5.4}$$

The solution to these equations is known [152]: non-dilatonic black p -branes in the presence of an electric potential have the metric

$$ds^2 = -\frac{f}{h^2}dt^2 + h^B\left(\frac{dr^2}{f} + r^2d\Omega_{n+1}^2 + dz^2\right), \tag{5.5}$$

where

$$f(r) = 1 - \left(\frac{r_0}{r}\right)^n, \quad h(r) = 1 + \left(\frac{r_0}{r}\right)^n \sinh^2\alpha, \quad B = \frac{2}{n+p}, \tag{5.6}$$

whereas the gauge field V has solution

$$V = -\frac{\sqrt{N}}{h}\left(\frac{r_0}{r}\right)^n \sinh\alpha \cosh\alpha dt, \quad N \equiv B + 2. \tag{5.7}$$

In these coordinates, the outer horizon is located at $r = r_0$, whereas the inner horizon coincides with the singularity at $r = 0$.

5.2.2 Characteristic Formulation for a Charged Black String

To describe a non-uniform charged black string, we start by a more general ansatz where the black string is locally boosted along its worldvolume $z^a = (t, z^A)$. Doing so is easier in the characteristic formulation of general relativity, where the metric is expressed in terms of the ingoing Eddington-Finkelstein (EF) coordinates. For a general Lorentz boost u^a , the EF coordinates $\sigma^a = (v, x^A)$ take the form [153, 154]

$$\sigma^a = z^a + u^a r_*, \quad r_*(r) = r + \int_r^\infty \frac{f - h^{N/2}}{f} dr. \tag{5.8}$$

The boosted metric for the charged string becomes

$$ds^2 = h^B \left(-\frac{f}{h^N} u_a u_b d\sigma^a d\sigma^b - 2h^{-N/2} u_a d\sigma^a dr + \Delta_{ab} d\sigma^a d\sigma^b + r^2 d\Omega_{n+1}^2 \right), \quad (5.9)$$

where $\Delta_{ab} = \eta_{ab} + u_a u_b$ is the orthogonal projector defined by the boost vector. Similarly, the gauge potential V becomes

$$V = -\frac{\sqrt{N}}{h} \left(\frac{r_0}{r} \right)^n \sinh \alpha \cosh \alpha u_a d\sigma^a, \quad (5.10)$$

and we take the radial gauge in order to set $V_r = 0$.

Our aim is to find solutions to the Einstein-Maxwell equations in which the black string's energy and charge densities, as well as the boost velocity along the string, are promoted to collective coordinates that vary in time along the x -direction. Given the hierarchy of scales present in the large D limit of black holes, we must specify the length scale relevant to the physics we wish to explore. It is known that black branes are unstable when subjected to perturbations of wavelength $\sim r_0/\sqrt{D}$. As such, we need to rescale the direction x along the string, $dx \rightarrow dx/\sqrt{n}$, thus making the boost non-relativistic. Additionally, the quasinormal modes under consideration scale like $\omega \sim \mathcal{O}(D^0)$, implying that the dynamics of the near-horizon geometry is decoupled from the asymptotic region [155]. Consequently, we will require the metric components to be asymptotically flat and the potentials to vanish at infinity at all orders in the perturbative expansion.

We write the metric and the gauge potential in terms of unknown fields

$$ds^2 = -Adv^2 + 2u_v dv dr + 2u_a dx^a dr - 2C_a dx^a dv + G_{ab} dx^a dx^b, \quad (5.11)$$

$$V = V_0 dv + V_a dx^a, \quad (5.12)$$

for which we allow the following $1/n$ expansion:

$$A = \sum_{k \geq 0} \frac{A^{(k)}(v, x, \mathbf{R})}{n^k}, \quad u_v = \sum_{k \geq 0} \frac{u_v^{(k)}(v, x, \mathbf{R})}{n^k}, \quad C_a = \sum_{k \geq 0} \frac{C_a^{(k)}(v, x, \mathbf{R})}{n^{k+1}}, \quad (5.13)$$

$$G_{ab} = \frac{1}{n} \left(1 + \sum_{k \geq 0} \frac{G_{ab}^{(k)}(v, x, \mathbf{R})}{n^{k+1}} \right), \quad u_a = \frac{u_a^{(0)}}{n} + \sum_{k \geq 1} \frac{u_a^{(k)}(v, x, \mathbf{R})}{n^{k+1}}, \quad (5.14)$$

$$V_0 = \sum_{k \geq 0} \frac{V_0^{(k)}(v, x, R)}{n^k}, \quad V_a = \sum_{k \geq 0} \frac{V_a^{(k)}(v, x, R)}{n^{k+1}}, \quad (5.15)$$

where the new radial coordinate $R = (r/r_0)^n$ is well-suited for near-horizon analysis. For the scalar field, we make the choice to keep $\phi = \log(r^2 h^B)$ at all orders in the expansion in order to maintain the spherical symmetry of the solution. Also note that demanding u_a to be a constant at leading order is simply a gauge choice; we will set $u_a^{(0)} = 0$ to fix the rest frame of the black string.

5.2.3 Solutions and Effective Brane Equations at Leading Order

At leading order, the solutions to the Einstein-Maxwell equations are given by

$$A^{(0)} = 1 - \frac{m}{R} + \frac{q^2}{2R^2}, \quad C_a^{(0)} = \left(1 - \frac{q^2}{2mR}\right) \frac{p_a}{R}, \quad u_v^{(0)} = 1, \quad (5.16)$$

$$G_{ab}^{(0)} = \left(1 - \frac{q^2}{2mR}\right) \frac{p_a p_b}{mR} - \log\left(1 - \frac{R_-}{R}\right) \left(2\delta_{ab} + \partial_a \frac{p_b}{m} + \partial_b \frac{p_a}{m}\right), \quad (5.17)$$

$$V_0^{(0)} = -\frac{q}{R}, \quad V_a^{(0)} = \frac{q p_a}{mR}. \quad (5.18)$$

Note that the radial coordinate appearing above has been shifted so that the outer and inner horizons of the charged black hole are now located at

$$R_{\pm} = \frac{1}{2} \left(m \pm \sqrt{m^2 - 2q^2}\right). \quad (5.19)$$

The collective variables m and q are directly related to the energy and charge densities \mathcal{M} and \mathcal{Q} of uniform p -branes

$$\mathcal{M} = r_0^n (n + 1 + nN \sinh^2 \alpha), \quad \mathcal{Q} = n\sqrt{N} r_0^n \sinh \alpha \cosh \alpha. \quad (5.20)$$

The large n expansion of these conserved quantities shows a correspondence between the old and new effective fields on the branes at leading order:

$$m \equiv r_0^n \cosh 2\alpha \quad \text{and} \quad q \equiv \frac{r_0^n}{\sqrt{2}} \sinh 2\alpha. \quad (5.21)$$

As for p , it is related to the momentum density on the black brane; the gauge choice $u_a^{(0)} = 0$ ensures that the total momentum on the brane vanishes.

The equations that govern the dynamics of the collective variables for general p -branes are¹ [150]:

$$\partial_t m - \partial_i \partial^i m = -\partial_i p^i, \quad (5.22a)$$

$$\partial_t q - \partial_i \partial^i q = -\partial_i \left(\frac{p^i q}{m} \right), \quad (5.22b)$$

$$\partial_t p_i - \partial_j \partial^j p_i = \partial_i (R_+ - R_-) - \partial^j \left[\frac{p_i p_j}{m} + R_- \left(\partial_i \frac{p_j}{m} + \partial_j \frac{p_i}{m} \right) \right]. \quad (5.22c)$$

These equations, which describe the fluctuations of black branes on the compactified string directions x^i in the large D limit, can also be written as conservation equations $\partial_\mu \tau^{(0)\mu\nu} = 0$ for a quasilocal stress tensor at $R \rightarrow \infty$, whose components are

$$\tau_{00}^{(0)} = m, \quad \tau_{0i}^{(0)} = \partial_i m - p_i, \quad (5.23)$$

$$\tau_{ij}^{(0)} = \partial_i \partial_j m - (R_+ - R_-) \delta_{ij} + \frac{p_i p_j}{m} - (\partial_i p_j + \partial_j p_i) \left(1 - \frac{R_-}{m} \right). \quad (5.24)$$

These equations are very easy to solve numerically. In doing so we discover the stable end-point of the charged string instability, as well as the time-dependent process leading to that end-point. To discuss the thermodynamics, to which we turn next, we need to discuss the next order in the large D expansion.

5.3 Phase Structure of the NUBS

Having set up our equations and non-uniform solutions, we now turn our attention to the phase structure of the charged black string, compactified along $x \in [-L/2, L/2]$. A proper analysis first requires us to examine the properties of NUBS to subleading order in the large D expansion.

¹In the large n limit, $\partial_t = \partial_v$ and the dynamics of the collective variables take place in Schwarzschild time.

5.3.1 Solutions and Effective Brane Equations at Subleading Order

At subleading order for the charged black string ($p = 1$), we find the solutions

$$A^{(1)} = -\frac{\delta m}{R} + \frac{q\delta q}{R^2} - \frac{q^2}{2R^2} + \log\left(1 - \frac{R_-}{R}\right) \left[-\frac{m}{R} + \frac{q^2}{2R^2}\right] \left(\frac{p}{m}\right)' - \log R \left[\frac{p'}{R} - \frac{q}{R^2} \left(\frac{pq}{m}\right)'\right] \quad (5.25)$$

$$V^{(1)} = -\frac{\delta q}{R} - \frac{q}{R} \log\left(1 - \frac{R_-}{R}\right) \left(\frac{p}{m}\right)' - \frac{\log R}{R} \left(\frac{pq}{m}\right)' \quad (5.26)$$

$$u_v^{(1)} = \frac{p^2}{2m^2} \left[-\frac{m}{R} + \frac{q^2}{2R^2}\right] - \left(1 - \frac{R_-}{R}\right)^{-1} \frac{R_-}{R} \left(\frac{p}{m}\right)' \quad (5.27)$$

where a prime denotes differentiation with respect to x . It is straightforward to verify that $\delta m(\sigma)$ and $\delta q(\sigma)$, which appear as integration constants, indeed correspond to the $1/n$ corrections to the mass and charge densities by computing the ADM mass \mathcal{M} and the electric flux at infinity via

$$\mathcal{M} = -\oint_{S_\infty^{n+1}} \nabla^\mu \xi_{(v)}^\nu dS_{\mu\nu} = \int \left(m(\sigma) + \frac{\delta m(\sigma)}{n} + \dots\right) dx, \quad (5.28)$$

$$\mathcal{Q} = \frac{1}{2} \oint_{S_\infty^{n+1}} F^{\mu\nu} dS_{\mu\nu} = \int \left(q(\sigma) + \frac{\delta q(\sigma)}{n} + \dots\right) dx, \quad (5.29)$$

where $\xi_{(v)}^\mu = \delta_v^\mu$ is a timelike Killing vector, and the integration is performed over S_∞^{n+1} at spatial infinity. Some ambiguity remains when using (5.28) and (5.29) to define the mass and charge density corrections since a shift in either quantity by the derivative of a periodic function results in identical ADM mass and electric flux. We thus examine the multipole expansion of g_{00} and V_0 about asymptotic infinity to identify $\delta m(\sigma)$ and $\delta q(\sigma)$ as the appropriate corrections. Let us remark that \mathcal{M} and \mathcal{Q} remain conserved at all orders in the $1/n$ expansion, and as such the corrections $\delta m(\sigma)$ and $\delta q(\sigma)$ have vanishing integrals over the string direction.

The above solutions will be useful in Section 5.3.2. For the remainder of this section, we will focus our efforts on the neutral case. The string's momentum correction is found in the $dvdx$ component of the metric

$$C_x^{(1)} = \frac{\delta p}{R} + \frac{\log R}{R} \left(\frac{p^2}{m}\right)'; \quad (5.30)$$

it is a quantity associated with the asymptotic Killing vector $\xi_{(x)}^\mu = \delta_x^\mu$

$$\mathcal{P} = \oint_{S_\infty^{n+1}} \nabla^\mu \xi_{(x)}^\nu dS_{\mu\nu} = \int \left(p(\sigma) + \frac{\delta p(\sigma)}{n} + \dots \right) dx. \quad (5.31)$$

The equations that govern the dynamics of δm and δp are²

$$\partial_t \delta m - \delta m'' + \delta p' = F'_{\delta m}, \quad (5.32a)$$

$$\partial_t \delta p - \delta p'' - \left[\left(1 + \frac{p^2}{m^2} \right) \delta m - \frac{2p}{m} \delta p \right]' = F'_{\delta p}, \quad (5.32b)$$

with the source functions $F_{\delta m}$ and $F_{\delta p}$ given by

$$F_{\delta m} = p + \left(m + 2p' - \frac{3p^2}{2m} \right)', \quad (5.33)$$

$$F_{\delta p} = F_0 \log m + \frac{F_0}{2} - \frac{p^2}{m} - \frac{3}{2} \left(\frac{p^3}{m^2} \right)' + \frac{4pm'}{m} - \frac{2p^2 m''}{m^2} + \frac{4pp''}{m}, \quad (5.34)$$

and

$$F_0 = 2m \left[1 + \left(\frac{p}{m} \right)' \right] \left(\frac{p}{m} \right)'. \quad (5.35)$$

As is the case at leading order, these equations can also be rewritten as correction terms for the asymptotic stress tensor τ_{ij} :

$$\tau_{00}^{(1)} = \delta m, \quad \tau_{0x}^{(1)} = \delta p - \delta m' - F_{\delta m}, \quad (5.36)$$

$$\begin{aligned} \tau_{xx}^{(1)} = & -F_0(\log m - 3) + m - \delta m \left(1 + \frac{p^2}{m^2} \right) + 2\delta p \frac{p}{m} \\ & + \left(\delta m + 4m + 4p' - 7\frac{p^2}{m} \right)'' - 2 \left(\delta p + 3p - \frac{3}{2} \frac{p^3}{m^2} \right)'. \end{aligned} \quad (5.37)$$

The left-hand sides of equations (5.32) correspond to the differential operators one would find at order $1/n$ by letting $m \rightarrow m + \delta m/n$ and $p \rightarrow p + \delta p/n$ in the collective equations (5.22). However, the presence of the source terms breaks Galilean invariance. Moreover, whereas the leading order equations are invariant under a rescaling of the mass and momentum, the collective

²The large D equations at NLO were first obtained in [156] for asymptotically AdS spacetimes, albeit in a gauge different from ours. We have confirmed that the equations we obtain agree with their AdS counterpart up to a redefinition of the momentum correction and a few sign flips.

equations for the correction terms are not. This can be understood as a consequence of the dependence of the black string temperature on its mass density m_0 at NLO. Indeed, when the NUBS is stationary, one can calculate the surface gravity κ via the relation

$$\kappa^2 = \sqrt{-\frac{1}{2}\nabla^\mu\xi_{(v)}^\nu\nabla_\mu\xi_{(v)\nu}}, \quad (5.38)$$

and evaluation at the Killing horizon is understood. Rescaling the surface gravity such that the temperature is of $\mathcal{O}(1)$ at leading order, we obtain

$$T = \frac{\kappa}{2\pi n} = \frac{1}{4\pi} - \frac{1}{4\pi n} \left(\log m - \frac{(m')^2}{2m^2} + \frac{m''}{m} \right) = T^{(0)} + \frac{T^{(1)}}{n}, \quad (5.39)$$

$$\text{with } T^{(1)} = -\frac{1}{4\pi} \left(\log m - \frac{m'^2}{2m^2} + \frac{m''}{m} \right). \quad (5.40)$$

As a consequence of this, we find that the shapes of δm and δp depend on the additional parameter m_0 . However, m_0 should not be regarded as an independent parameter of our solutions. The initial state of our system is uniquely characterized by D and the ratio L/r_0 , and as such mass and momentum profiles at different initial temperatures contain the same information packaged differently. It is easier to work in units where $r_0 = 1$ (for which $m_0 = 1$ also), but we can equivalently rescale all dimensionful quantities by an appropriate power of r_0 to obtain the same information.

Let us now turn our attention to the next-to-leading order correction to the dispersion relation for the black string. Linearized perturbations around the uniform black string solution $m(x) = m_0 + \Delta m e^{-i\omega t + ikx}$, with momentum $k = 2\pi/L$ aligned along the string direction x , allow for a non-trivial solution only if the condition

$$\begin{vmatrix} -k^2 + i\omega - \frac{k^2}{n} & -ik + \frac{ik(1-2k^2)}{n} \\ ik & -k^2 + i\omega - \frac{k^2(1+2\log m_0)}{n} \end{vmatrix} = 0 \quad (5.41)$$

is satisfied. Letting $\Omega = -i\omega$, the dispersion relation for the black string reads

$$\Omega(k) = k - k^2 - \frac{k}{2n} (1 + 2k + 2k \log m_0 - 2k^2) + \mathcal{O}(n^{-2}). \quad (5.42)$$

This yields the corrected threshold mode $\Omega(k_{\text{GL}}) = 0$ to be

$$k_{\text{GL}} = 1 - \frac{1 + 2 \log m_0}{2n} + \mathcal{O}(n^{-2}). \quad (5.43)$$

Rewriting the above equations as $\hat{\Omega}(\hat{k}) \equiv \Omega(kr_0)r_0$ so that they become dimensionless eliminates the dependence on the mass density m_0

$$\hat{\Omega}(\hat{k}) = \hat{k} - \hat{k}^2 - \frac{\hat{k}}{2n} \left(1 + 2\hat{k} - 2\hat{k}^2\right) + \mathcal{O}(n^{-2}), \quad \hat{k}_{\text{GL}} = 1 - \frac{1}{2n} + \mathcal{O}(n^{-2}), \quad (5.44)$$

and thus we recover the expected result [64], regarding the shift of the critical wavelength of the Gregory-Laflamme instability at subleading order.

5.3.2 Charged Black String Phase Diagram

When $k < k_{\text{GL}}$, neutral NUBS always have a lower event horizon surface area than uniform string solutions. Since the addition of charge weakens the GL instability of black strings, it is natural to wonder if the NUBS remains entropically favoured, especially as we approach extremality.

The entropy \mathcal{S} of a black string is related to the area of its horizon

$$\mathcal{S} = \frac{\Omega_{(n+1)}}{4G} \int_{\text{horizon}} \sqrt{g_{xx}} e^{\frac{(n+1)\phi}{2}} dx = \frac{\Omega_{(n+1)}}{4G\sqrt{n}} \left(\mathcal{S}_0 + \frac{\mathcal{S}_1}{n} + \dots \right). \quad (5.45)$$

At leading order, the area of a boosted string is given by the integral of the outer horizon radius

$$\mathcal{S}_0 = \int R_+ dx. \quad (5.46)$$

Due to conservation of energy and charge, this integral is the same for the UBS and NUBS, and we need to examine \mathcal{S}_1 to witness an entropy difference between the two phases. However, it does not suffice to know the expansion of $\sqrt{g_{xx}}$ at subleading order; one also has to take into consideration the $1/n$ correction to the Killing horizon. We obtain the latter by requiring

$$g_{00} = A^{(0)}(v, x, R_h) + \frac{A^{(1)}(v, x, R_h)}{n} = 0, \quad \text{with } R_h = R_+ + \frac{R_h^{(1)}}{n}. \quad (5.47)$$

Thus we find

$$\mathcal{S}_1 = R_h^{(1)} + R_+ \log(R_+ - R_-) + \frac{R_+}{2} G_{xx}^{(0)}(R_+) \quad (5.48)$$

At equilibrium, charge density diffuses until it becomes proportional to the mass profile of the non-uniform black string, which enables us to write $q = \rho m$, with $\rho = q_0/m_0$ being the (conserved) charge-to-mass ratio of the black string. This yields

$$\begin{aligned} \mathcal{S}_1^{\text{NUBS}} = & \int \frac{1 + \sqrt{1 - 2\rho^2}}{2} \left\{ (m'' + m) \log \left((1 + \sqrt{1 - 2\rho^2}) \frac{m}{2} \right) \right. \\ & \left. + \frac{1}{2} \left(\frac{2\rho^2}{1 - 2\rho^2 + \sqrt{1 - 2\rho^2}} m + \frac{m'^2}{m} \right) \right\} dx \end{aligned} \quad (5.49)$$

$$\mathcal{S}_1^{\text{UBS}} = \frac{2\pi}{k} (1 + \sqrt{1 - 2\rho^2}) \left\{ \frac{m_0}{2} \log \left((1 + \sqrt{1 - 2\rho^2}) \frac{m_0}{2} \right) \right. \quad (5.50)$$

$$\left. + \frac{\rho^2}{1 - 2\rho^2 + \sqrt{1 - 2\rho^2}} \frac{m_0}{2} \right\} \quad (5.51)$$

where we have taken advantage of the fact that the coefficients multiplying δm and δq were constant to integrate them away. It is easy to check that the difference in the two phases' horizon area $\Delta\mathcal{S}_1 \equiv \mathcal{S}_1^{\text{NUBS}} - \mathcal{S}_1^{\text{UBS}}$ is always positive no matter the ratio ρ . In particular, the entropy difference at extremality is half that of neutral strings

$$\Delta\mathcal{S}_1|_{\rho=\frac{1}{\sqrt{2}}} = \frac{1}{2} \Delta\mathcal{S}_1|_{\rho=0} = -\frac{2\pi m_0}{k} \left(T_{\text{NUBS}}^{(1)} - T_{\text{UBS}}^{(1)} \right) > 0. \quad (5.52)$$

This result indicates that the NUBS is always the preferred phase, and thus the instability persists for all charged brane configurations (as illustrated in Figure 5.1). However, despite the effective theory (5.22) admitting a smooth limit when $\rho \rightarrow \frac{1}{\sqrt{2}}$, we need to keep in mind that the large D expansion formally breaks down at extremality. Nevertheless, this result corroborates the ones obtained via hydrodynamics [154]. This and the exact cancellation in (5.52) of the pathologic divergences typically encountered at extremality both offer a positive outlook on the validity of results beyond the limits of our approximation.

We note that the numerical results of this section and the next have been obtained by evolving small periodic perturbations around a uniform black string solution using a Runge-Kutta-Fehlberg method on a periodic Fourier grid made of 41 points. The conserved quantities \mathcal{M} , \mathcal{Q} and \mathcal{P} , as well as the charge-to-mass ratio ρ , all remained constant during the evolution. Likewise, the integrals of δm and δp along the string direction were both

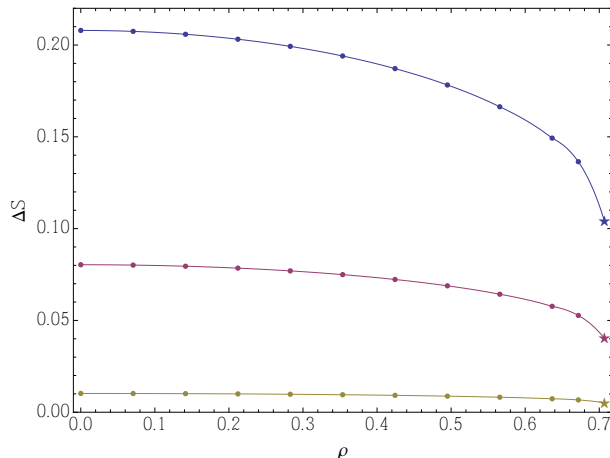


Figure 5.1: Entropy difference per unit length as a function of the charge density for $k = \{0.75, 0.85, 0.95\}$, starting from the top. The numerical evolution breaks down at extremality, hence we use a star plot marker to distinguish the analytical result at $\rho = 1/\sqrt{2}$ from the others.

zero to very good numerical accuracy until the final state was reached.

5.3.3 Pinch-Off?

Let us now turn our attention back to the mass and momentum corrections δm and δp . In principle, the contents of equations (5.32) should provide us with a method for identifying the critical dimension D^* below which the black string would *pinch-off*, rather than settle on a smooth non-uniform final state. Such a transition in the nature of the final state is expected at low enough D . It is interesting to see how this manifests itself in the large D expansion.

Below we present criteria we impose on the solutions, and the time evolution towards those solutions, to investigate that question. While the various criteria we impose clearly indicate a tendency towards a pinch-off, we were not able to find a universal value for the critical dimension D^* .

To determine the critical dimension n^* , we first define the total corrected mass density

$$M_n(x) = m(x) + \frac{\delta m(x)}{n}, \quad (5.53)$$

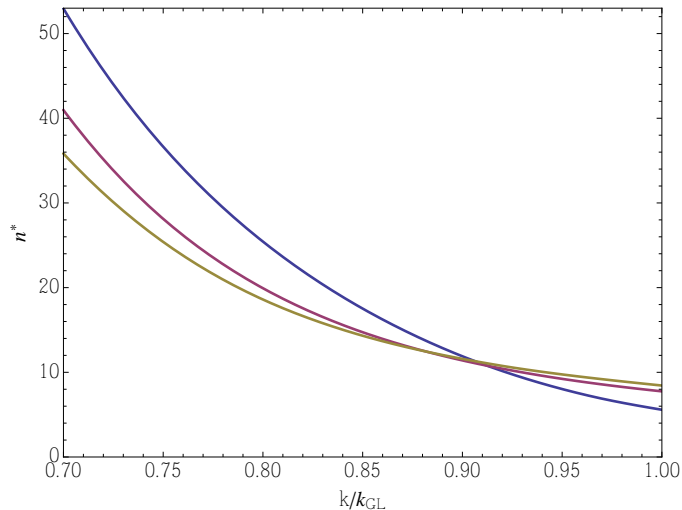


Figure 5.2: The critical curves n^* for $m_0 = \{1, 3, 5\}$, from top to bottom, obtained at NLO. Black strings with parameters above the critical curves correspond to stable NUBS, whereas we conjecture a pinch-off scenario for the those below, which exhibit negative tension.

and the corrected tension

$$\mathcal{T}_n = - \int \left(\tau_{xx}^{(0)} + \frac{\tau_{xx}^{(1)}}{n} \right) dx, \quad (5.54)$$

which are both gauge invariant quantities.

One attempt at diagnosing the stability of the black string at subleading order using our knowledge of $m(x)$ and $\delta m(x)$ is to find n^* such that $M_{n^*}(x)$ becomes locally negative. One can do so either by looking at the dynamical evolution, or by examining the properties of the final state only. It turns out that the dynamical evolution of the collective variables is highly sensitive to the size of the initial perturbations around the uniform solution $m(x) = m_0$. As such, this method does not provide a reliable stability diagnostic. As for the shape of the end-point of the dynamical evolution, the final shape of $\delta m(x)$ does depends solely on the static profile $m(x)$. This makes it possible to find n^* such that $M_{n^*}(x) < 0$ locally, but this method has not yielded accurate results.

An alternate, more successful, method to identify the critical dimension n^* uses the corrected tension (5.54). Indeed, it is possible to find a critical curve n^* as a function of the dimensionless wavenumber k/k_{GL} by assuming that the fate of a NUBS with negative tension is to pinch-off. Our results are summarized Figure 5.2 for three different initial configurations m_0 . Note that as we vary m_0 we change k_{GL} , so this is an alternate way to scan the the “thickness” k/k_{GL} . However, while the qualitative features are similar, we still see slight differences between the three curves, which are either an artifact of early truncation in the $1/n$ expansion or a sign that negative brane tension is a sufficient but not necessary condition for pinching-off. Indeed, nothing stops a pinch-off from happening at positive tension, and as such our critical curves may be thought of as an approximate probe until further investigation.

While the results we obtain preclude us from assigning an unambiguous value for the critical dimension, it can serve as a bound on the dimension in which the final state pinches off, and it illustrates the dependence of the critical dimension on the brane thickness. It is interesting to note that the dimensions near the critical point $k = k_{GL}$ are quite close to the expected value $n^* = 9$.

5.4 Two Dimensional Non-Uniform Phases

We now move to discuss the case of unstable membranes, for which there are two independent modes of Gregory-Laflamme instabilities. Similar to the one-dimensional case we find that in the leading order in the large D limit, the final state is a smooth and non-uniform configuration which we call a lattice. Using the tools developed above, we study the phase diagram and determine the preferred size and shape of this lattice configuration.

In two dimensions, it is possible to construct periodic black brane configurations over oblique lattices. The lattices can be described by two vectors, describing the periodicities of the system:

$$\mathbf{k}_x = \frac{2\pi}{L_x}(\cos \alpha, -\sin \alpha), \quad \mathbf{k}_y = \frac{2\pi}{L_y}(0, 1), \quad \text{with } 0 \leq \alpha \leq \pi/2. \quad (5.55)$$

Thus we parametrize possible non-uniform solutions solutions by the three parameters (L_x, L_y, α) . Furthermore, since we are mostly interested in the preferred shape of the non-uniform configuration, we take $L_x = L_y = L$. The angle α characterizes then the shape: special cases include $\alpha = 0$ for checkerboard lattices, $\alpha = \pi/6$ for triangular lattices, and $\alpha = \pi/2$ for

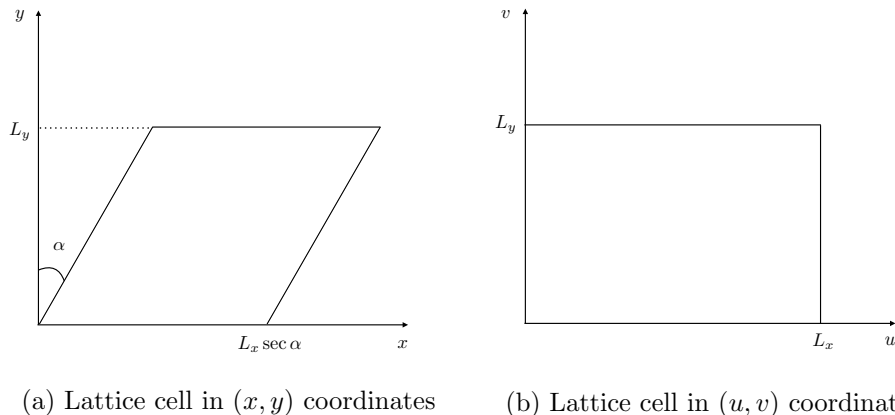


Figure 5.3: The change of coordinates from (x, y) to (u, v) maps oblique lattice cells (a) to rectangular ones (b). Their area is $\mathcal{A}_{\text{cell}} = L_x L_y \sec \alpha$.

stripes.

For the purpose of constructing the solutions, it is easier to work with the coordinates (u, v) defined by

$$u = x \cos \alpha - y \sin \alpha, \quad v = y. \quad (5.56)$$

In these coordinates (illustrated in Figure 5.3), periodic boundary conditions are simply

$$(u, v) \equiv (u + L_x n_x, v + L_y n_y). \quad (5.57)$$

for any integers n_x, n_y .

In order to make meaningful comparison between lattices of different size and shape, we need to work with the right thermodynamic potential. Instead of fixing the size and the shape of the unit cell, we instead fix the conjugate variables: the tensions in different directions. See [157] for a general discussion, and [158] for a recent application closely related to the current discussion.

The first law of black brane dynamics, in the micro-canonical ensemble, can be written as

$$dM = \kappa dA + \mathcal{T}^{ab} dV_{ab}, \quad (5.58)$$

where \mathcal{T}^{ab} are related to the tensions along brane directions, and V_{ab} is a matrix of periodicities. To fix the conjugate variables instead of the size and

shape of the brane configuration, we define the “enthalpy” H of the brane³ as the Legendre transform

$$H \equiv M - \mathcal{T}^{ab}V_{ab}. \quad (5.59)$$

Our goal is to minimize this new potential. But first, we need to find an expression for the tensions \mathcal{T}^{ab} . These are usually obtained from the quasilocal stress tensor at $R \rightarrow \infty$, which we have already found in (5.24):

$$\tau^{ab} = \partial_a \partial_b m - m \delta_{ab} + \frac{p_a p_b}{m} - (\partial_a p_b + \partial_b p_a). \quad (5.60)$$

We identify this boundary stress tensor as the source for the tensions, such that

$$\mathcal{T}^{ab} = \langle \tau^{ab} \rangle = \iint_{\text{cell}} \tau^{ab} dx dy / \iint_{\text{cell}} dx dy = \frac{1}{L^2} \iint_{\text{cell}} \tau^{ab} dudv. \quad (5.61)$$

In the orthogonal coordinates (u, v) , only the pressures \mathcal{T}^{uu} and \mathcal{T}^{vv} should contribute, and as such we take $V_{mn} = L^2 \delta_{mn}$ for $m, n = u, v$. Since we are working at constant mass, the quantity we must minimize is the tension β given by

$$\beta(\alpha) = -\mathcal{T}^{mn} \delta_{mn} \quad (5.62)$$

$$= -\frac{1}{L^2} \iint_{\text{cell}} (\cos^2 \alpha \tau^{xx} - 2 \cos \alpha \sin \alpha \tau^{xy} + (1 + \sin^2 \alpha) \tau^{yy}) dudv. \quad (5.63)$$

As expected, the enthalpy of oblique lattices includes contributions from the shear components of the stress tensor τ^{xy} .

It is straightforward to apply the change of variables (5.56) to (5.22) in order to find the inhomogeneous solutions on the oblique lattice numerically. For that purpose we discretize the lattices on a 31×31 periodic Fourier spectral grid, and we used the fifth order Runge-Kutta-Fehlberg time-stepping algorithm to perform the time evolution towards the stable inhomogeneous solution.

Once we obtain the solutions for different shapes, we can find which shape is preferred — our results are illustrated in Figure 5.4 for two different choices of lattice size. We find that the minimum of H is reached for lattices with opening angles close to $\alpha = \pi/6$, which corresponds to the triangular

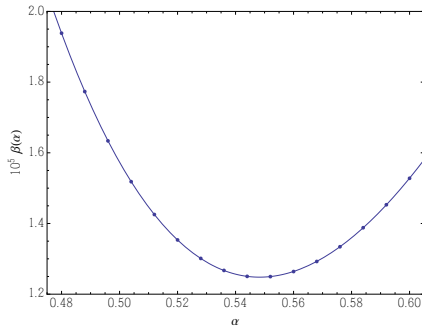
³The conventional enthalpy is obtained by Legendre transform with respect to the total volume, to work with fixed pressure instead.

lattice. Unsurprisingly, the position of the minimum depends on the size of the cell. Based on these results, we expect that for asymptotically large lattices the triangular lattice is the preferred configuration, and the slight deviations we see are due to finite size effects.

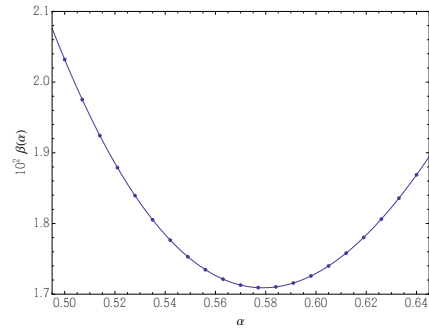
One can repeat the exercise with respect to the size of the preferred configuration. Indeed, in the one-dimensional case, where there is a size but not shape parameter, the tension β of a black string with mass density m_0 decays exponentially with the string length L

$$\beta(L) = -\langle \tau^{xx} \rangle \sim m_0 e^{-a(L-2\pi)}, \quad \text{with } a \approx 1.827, \quad (5.64)$$

meaning that the size of the preferred configuration is asymptotically large.



(a) The tension as a function of the opening angle for $k = 0.6$. The minimum is located at $\alpha \approx 0.548$.



(b) The tension as a function of the opening angle for $k = 0.8$. The minimum is located at $\alpha \approx 0.579$.

Figure 5.4: The enthalpy of the Bravais lattices reaches its minimum closer to $\alpha = \pi/6 \approx 0.524$ as the size of the cell increases. Note that the numerical evolution becomes unstable for large α and large L , thus preventing us from probing larger oblique cells.

5.5 Conclusion

The principal focus of our work was to determine the fate of extended black objects, in the approximation where the number of dimensions is large. The tools of general relativity at large D have proven useful at unveiling robust properties of higher dimensional black holes to surprising accuracy, and our hope is that likewise the results presented in this paper hold up beyond the

asymptotic limit of that approximation.

The main loose end left in this work is determining whether negative brane tension is an appropriate test to accurately determine the fate of the black string instability. While we see indications that the pinch-off scenario is likely as the final state at sufficiently low D , as well as a non-trivial dependence of the associated critical dimension on the string thickness, we have not obtained a precise unambiguous result nor succeeded in reconciling these features of our solution with the current results in the literature. We hope to return to this in the future.

It would also be an interesting endeavour to explore the dynamics of charged dilatonic Kaluza-Klein black holes given the existence of exact uniform solutions. Such a direct comparison would expand our understanding of the effects of charge on the stability of black strings in more general scenarios.

Chapter 6

Conclusion

6.1 Summary and Future Directions

In this dissertation we investigated the consequences of breaking spatial translation invariance in gravitational systems. We used the tools of the gauge/gravity duality to construct a Josephson junction holographically and to examine entanglement propagation in strongly coupled systems. We also made use of the so-called large D approximation of general relativity to address black brane instabilities at next-to-leading order for asymptotically flat spacetimes.

6.1.1 AdS/CMT

In chapter 2 we constructed the holographic equivalent of a chiral Josephson junction as part of the AdS/CMT (condensed matter theory) programme. Chiral superconductivity occurs at low temperatures when an operator with $p + ip$ -wave symmetry acquires a vacuum expectation value that explicitly breaks the $U(1)$ subgroup of $SU(2)$, which we identified with electromagnetism. To model a Josephson junction, we considered a chemical potential varying spatially in such a way that the order parameter was non-zero everywhere except for a narrow region in the centre, effectively corresponding to a metallic weak link surrounded by two infinite $p + ip$ -wave superconductors.

Our setup showed the expected current-phase sinusoidal relation known as the Josephson current as well as various relationships obeyed by this critical current and the order parameter. However, the $p + ip$ symmetry of our setup revealed a curious feature absent from p - and s -wave superconductors: gapless chiral counter-propagating currents localized at the boundary between phases. We found that the intensity of these edge currents remained approximately constant for S-N-S junctions regardless of the charge density of the normal phase, whereas it decreased linearly as a function of the chemical potential for S-S'-S junctions. In addition we observed a quadratic relationship between the edge currents and the magnitude of the order parameter.

Gapless chiral signatures such as these edge currents are usually indica-

tive of Majorana topological modes, albeit indirectly. Our holographic setup is unfortunately insensitive to other unconventional features of topological superconductivity, such as the 4π -periodicity of the Josephson current. In the condensed matter literature this 4π -periodicity anomaly is typically observed in the AC Josephson effect, which can be constructed holographically by having a time-dependent phase for the bulk order parameter. Such a setup should be relatively easy to study now that we have developed the tools to treat with non-static geometries effectively.

Alternatively, the presence of Majorana zero-modes may be revealed by investigating fermion scattering across a chiral interface. The conventional Josephson effect is attributed to Cooper pair tunnelling, but is believed to be transported by single electrons in topological superconductors. As such studying a fermionic action with a Majorana mass term [159]

$$S_\eta = \int d^{d+1}x \sqrt{-g} \phi^* \bar{\psi}^c (\eta^* + \eta_5^* \Gamma^5) \psi + \text{h.c.} \quad (6.1)$$

in the presence of a chiral superconductor is akin to studying Andreev reflection at strong coupling, which has the potential to reveal unconventional signatures indicative of topological zero-modes. Complications arising from studying the Dirac equation in curved spacetimes with spatial inhomogeneities prevented a preliminary analysis to be carried out, but we nonetheless believe that (6.1) may hold answers to address topological superconductivity with the gauge/gravity duality.

The AdS/CMT programme is also quite vast and offers various other opportunities to investigate spatial inhomogeneities. For instance, holographic systems intrinsically lack the lattice structure responsible for momentum relaxation in conventional systems. Indeed, translation invariance in field theories at finite density results in the appearance of an anomalous delta function in the optical conductivity at zero frequency. This infinite metallic Drude peak is due to the inability for charge carriers to dissipate their momentum in homogeneous holographic theories. The introduction of a symmetry-breaking lattice in the form of a periodic neutral scalar field that can backreact of the geometry broadens this Drude peak [160], a feature more in line with experimental observations. An alternate method for incorporating momentum dissipation without compromising the homogeneity of bulk solutions is to introduce spatially-dependent massless scalar sources that effectively act as a channel for relaxation [161]. Such a model also results in a widened Drude peak at zero frequency.

Regardless of the method, the addition of momentum dissipation can

help broaden our understanding of current models: the transport properties of holographic superconductors may change in the presence of a lattice; the phonon spectrum of the field theory may be calculated via the fluctuations of the bulk field responsible for the lattice; Fermi surfaces calculated from probe fermions may have more realistic features, etc. Breaking translation invariance invariably results in a more accurate description of the models at the cost of computational complexity, but holography makes this cost bearable compared to traditional methods. It is our hope that the numerical techniques used throughout this thesis help bridge the complexity gap in addressing this type of problem in the future.

6.1.2 Holographic Entanglement Entropy

Chapters 3 and 4 were devoted to the study of entanglement propagation in field theories admitting a gravitational dual. Entanglement was produced by the intermediary of a scalar source responsible for a localized injection of energy into a system in thermal equilibrium. The resulting thermalization of spacetime was then probed via the dynamics of bulk extremal surfaces anchored on the boundary whose area acts as a dual measure of entanglement entropy. The two most striking results were the appearance of an entanglement lightcone structure in the $L - t$ plane and the logarithmic decay of entanglement entropy.

The emergent lightcone featured two distinct regimes of entanglement propagation: early-time propagation for wide quenches ($L < \sigma$), and late-time propagation for large entangling surfaces ($L > \sigma$). Our analysis suggests that the mechanisms responsible for the spatial spread of chaos in holographic theories, characterized by the butterfly velocity $v_{\text{butterfly}} = \sqrt{3}/2 = 0.866$, are very likely to influence the thermalization of entanglement degrees of freedom at early-times. This result also echoes those found in the literature for global quenches, where entanglement saturation occurs at times $t \sim L/v_{\text{butterfly}}$ for large strip regions. Local quenches for large entangling surfaces were instead characterized by a lightcone velocity $v_E \in [0.65, 0.7]$, an interval that comprises many velocities of interest. These include the speed of sound, the shear velocity, and the tsunami velocity. Our initial analysis suggested that the latter could play a role in quantifying the spread of entanglement at late-times given that it is an intrinsic property of the equilibrium thermal state, but the addition of charge quickly dispelled this notion. Extremal black holes are characterized by a vanishing tsunami velocity, but v_E was found to be robust against the addition of charge, which led us to speculate that the mechanisms underlying momentum diffusion in

the sound and shear channels would be responsible for entanglement propagation instead.

As for the decaying behaviour of entanglement entropy, improved numerics helped us revise our initial conclusions indicative of an exponential damping at late-times. Modifications including domain decomposition in the radial direction, higher spatial resolution, and other “under the hood” changes, allowed us to extend the evolution of the quench for twice as long in a reasonable computational time. This extra data instead revealed that a logarithmic decay $\sim \log t/t^\delta$ provided a much better fit. This result mirrors similar conclusions obtained in the context of spin chains in two-dimensional CFTs (which have $\delta = 1$), but we also found evidence for a transition between the $\delta = 1$ and $\delta = 1.5$ regimes as a function of charge and strip width, indicating a richer story that we have yet to discover.

These two projects were very ambitious but technical limitations complicated the analysis. For instance the space of parameters that could be explored was huge; the scalar quench amplitude and width, the strip width, the initial mass density and the initial charge density could all be varied independently, and each typically introduced an inherent length scale of its own. Given the competition between these different scales and our reliance on a numerical approach, it became difficult to thoroughly characterize the defining regimes in order to compare and contrast our results with those in the literature. We were also confronted to an order of limits issue when studying theories at finite charge densities. The near-horizon geometry of extremal black holes is $\text{AdS}_2 \times \mathbb{R}^2$, which indicates an emergent scale invariance in the IR. Our original motivation for studying RN backgrounds was then to investigate the dynamics of extremal surfaces as we progressively changed the near-horizon topology. Unfortunately our numerics restricted us to the study of narrow entangling surfaces, which did not allow for deep enough probes of the geometry. As such the $L \rightarrow \infty$ and extremal limits, as well as their potentially distinct regularities, remained out of reach with this setup.

A proper numerical analysis of large entangling regions and their IR dynamics in near-extremal backgrounds would be a welcome addition to the current analysis. Moreover, the technology we have developed to solve the dynamical Einstein and geodesic equations could be used to investigate shapes other than the infinite strip, such as spherical regions or off-center geometries. Other measures of quantum information would also be interesting to compute in our setup. In particular, the mutual information between

two regions \mathcal{A} and \mathcal{B} , defined as

$$I(\mathcal{A}, \mathcal{B}) = S_{\mathcal{A}} + S_{\mathcal{B}} - S_{\mathcal{A} \cup \mathcal{B}}, \quad (6.2)$$

is UV-finite and provides a measure of the total quantum correlations between \mathcal{A} and \mathcal{B} without contributions from thermal entropy [162].

The connection between the gauge/gravity duality and quantum information is only just starting to be unraveled. Recent developments have shown that AdS/CFT provides a natural setting to study tensor networks working as encoders for quantum error-correction code [163, 164]. Moreover, a tensor network known as Multi-scale Entanglement Renormalization Ansatz (MERA), used to estimate the ground state of quantum systems with long-range entanglement, was found to resemble the hyperbolic geometry of anti-de Sitter spacetimes, suggesting there might be an underlying AdS/MERA correspondence at work [165]. Work in that direction has the potential to provide answers to fundamental questions about the nature of entanglement.

Lastly, other future directions include studies of thermalization in strongly coupled field theories far-from-equilibrium. The gauge/gravity duality allows us to investigate QCD-like theories, which may reveal insights about the dynamics of the quark-gluon plasma and the confinement/deconfinement phase transition characteristic of asymptotic freedom. The power of numerical relativity has already been harnessed to model heavy ion collisions and jet quenching, and the gauge/gravity duality has provided a language to discuss hydrodynamic quantities such as shear viscosity at strong coupling [166]. The current models boast a high degree of symmetry, and more realistic features are bound to be extracted by considering inhomogeneous settings as we have done throughout this dissertation.

6.1.3 Large D Limit of General Relativity

In chapter 5 we set our sights on brane instabilities in asymptotically flat spacetimes. Solving the full dynamics of the inhomogeneous Einstein equations is typically very difficult in flat space, but the formalism of general relativity when the number of dimensions D is large reduces the computation to an asymptotic matching problem. This simplification occurs because the gravitational field of a black hole becomes localized within a distance $\sim 1/D$ of the horizon, thus decoupling it from the outside dynamics.

The effective conservation equations describing the fluctuations in the brane's energy, momentum and charge densities at leading and next-to-

leading order in a $1/D$ expansion were both easily solvable numerically and amenable to a linearized perturbation analysis. Examining these equations in turn allowed us to recover the instability spectrum at next-to-leading order and improved our understanding of the black string's phase structure. In particular, we confirmed that unstable branes remain unstable at extremality, established a novel condition to determine the critical dimension below which the string is prone to fragmentation, and discovered that two-dimensional membranes minimize their enthalpy on triangular lattices. Our investigation thus adds to the wealth of results already supporting the validity of the large D approximation.

A notable aspect of this formalism is its hydro-elastic complementarity, which describes the equivalence between the black branes' elastic theory description and their hydrodynamical features at large D . To paraphrase the authors of [150], ripples on a black brane can be interpreted both as pressure waves on a fluid and as wrinkles on a membrane. The equivalence is manifest in that the effective equations can be described in terms of curvatures and surface gravity (the elastic point of view), as well as via the dynamics of a stress tensor with a truncated gradient expansion (as in hydrodynamics). Note however that the large D formalism has more predictive power than a naive hydrodynamical approach since it captures phenomena the latter cannot (e.g. static NUBS) and typically remains valid even when gradients become steep. We made use of this alternative point of view to compute brane tension in our work, which provided us with a novel criteria to predict brane instability. However a proper analysis of the effective equations and their hydro-elastic formulation at next-to-leading order is still lacking and would definitely be worth pursuing.

The large D approximation can also be used in anti-de Sitter geometries, which opens up endless possibilities when combining it with the tools of the gauge/gravity correspondence. In fact holographic superconductors have already been subjected to this formalism [167], and an analysis of the dynamics between rarefaction waves and shockwaves using the tools of the fluid/gravity correspondence at large D was conducted in [156]. Problems due to backreaction of matter on the geometry are trivialized in this context, and extensions to include different symmetries and conserved charges could be pursued straightforwardly. We could also investigate condensed matter systems admitting a gravitational dual and their properties robust to taking $D \rightarrow \infty$, extract the generic features of thermalization of strongly coupled field theories in a $1/D$ expansion, and so on. The large D formalism is highly flexible and its many applications have the promising potential to unravel the mysteries of black hole dynamics further than ever before.

6.2 Concluding Remarks

The principal contribution of the work presented in this dissertation is the study of gravitational systems with a reduced degree of symmetry due to the presence of spatial inhomogeneities. The loss of translation invariance adds a layer of complexity compared to the homogeneous case since the physical content of general relativity comes packaged in coupled non-linear partial differential equations requiring a numerical approach. We have however repeatedly seen that this compromise in complexity typically results in richer dynamics. Indeed, through the lens of the gauge/gravity duality we were able to reproduce the physics of Josephson junctions and observed unconventional gapless chiral currents at the normal metal/superconductor interface. We also observed an entanglement lightcone by studying local quenches in holographic theories, which allowed us to speculate about the mechanisms responsible for entanglement propagation. This structure had not been fully appreciated in the study of global quenches due to entanglement entropy saturation, an issue that we circumvented by injecting a finite amount of energy via a localized excitation. Finally, we succeeded in reproducing many salient features of black string dynamics with the formalism of general relativity with infinite dimensions. Technical issues, such as numerical instabilities typically found in asymptotically flat spacetimes and gauge redundancies in gravity perturbation theory, were eschewed in favour of simpler effective brane equations that captured many universal aspects of non-uniform black strings. In view of all this, the central lesson from chapters 2 through 5 is that there is still much to learn by adding more realistic features to the current models.

Despite its technical challenges, numerical holography is currently one of the most promising tools at our disposal to learn about phenomena defying our current understanding. It offers surprising connections between vastly different systems via the unifying language of black holes and provides a wealth of opportunities to study systems of reduced symmetry without the severe limitations of more standard approaches. Similarly to the large N limit of strongly coupled field theories, the large D limit of general relativity brings about important simplifications of gravitational dynamics, which in turn provides a method to investigate a wide variety of higher-dimensional black objects without relying on prohibitively expensive simulations. It is our hope that the various numerical approaches presented and developed in this thesis will soon become a standard part of the professional toolkit used in modelling phenomena of increasing realism.

Bibliography

- [1] J. Casalderrey-Solana, H. Liu, D. Mateos, K. Rajagopal, and U. A. Wiedemann, *Gauge/String Duality, Hot QCD and Heavy Ion Collisions*, [arXiv:1101.0618](#).
- [2] G. 't Hooft, *A Planar Diagram Theory for Strong Interactions*, *Nucl. Phys.* **B72** (1974) 461.
- [3] J. M. Maldacena, *The Large N limit of superconformal field theories and supergravity*, *Int. J. Theor. Phys.* **38** (1999) 1113–1133, [[hep-th/9711200](#)]. [*Adv. Theor. Math. Phys.*2,231(1998)].
- [4] V. E. Hubeny, S. Minwalla, and M. Rangamani, *The fluid/gravity correspondence*, in *Black holes in higher dimensions*, pp. 348–383, 2012. [arXiv:1107.5780](#). [[817\(2011\)](#)].
- [5] J. Polchinski, *Tasi lectures on D-branes*, in *Fields, strings and duality. Proceedings, Summer School, Theoretical Advanced Study Institute in Elementary Particle Physics, TASI'96, Boulder, USA, June 2-28, 1996*, pp. 293–356, 1996. [hep-th/9611050](#).
- [6] E. Witten, *Bound states of strings and p-branes*, *Nucl. Phys.* **B460** (1996) 335–350, [[hep-th/9510135](#)].
- [7] G. T. Horowitz and A. Strominger, *Black strings and P-branes*, *Nucl. Phys.* **B360** (1991) 197–209.
- [8] P. Di Francesco, P. Mathieu, and D. Sénéchal, *Conformal Field Theory*. Graduate Texts in Contemporary Physics. Springer, 1997.
- [9] R. Bousso, *The Holographic principle*, *Rev. Mod. Phys.* **74** (2002) 825–874, [[hep-th/0203101](#)].
- [10] J. D. Bekenstein, *Universal upper bound on the entropy-to-energy ratio for bounded systems*, *Phys. Rev. D* **23** (Jan, 1981) 287–298.
- [11] A. W. Peet and J. Polchinski, *UV / IR relations in AdS dynamics*, *Phys. Rev.* **D59** (1999) 065011, [[hep-th/9809022](#)].
- [12] K. Skenderis, *Lecture notes on holographic renormalization*, *Class. Quant. Grav.* **19** (2002) 5849–5876, [[hep-th/0209067](#)].

- [13] S. de Haro, S. N. Solodukhin, and K. Skenderis, *Holographic reconstruction of space-time and renormalization in the AdS / CFT correspondence*, *Commun. Math. Phys.* **217** (2001) 595–622, [[hep-th/0002230](#)].
- [14] P. Breitenlohner and D. Z. Freedman, *Stability in Gauged Extended Supergravity*, *Annals Phys.* **144** (1982) 249.
- [15] I. R. Klebanov and E. Witten, *AdS / CFT correspondence and symmetry breaking*, *Nucl.Phys.* **B556** (1999) 89–114, [[hep-th/9905104](#)].
- [16] J. Bardeen, L. N. Cooper, and J. R. Schrieffer, *Theory of superconductivity*, *Phys. Rev.* **108** (Dec, 1957) 1175–1204.
- [17] P. W. Anderson, *Plasmons, gauge invariance, and mass*, *Phys. Rev.* **130** (Apr, 1963) 439–442.
- [18] S. Weinberg, *Superconductivity for Particular Theorists*, *Prog. Theor. Phys. Suppl.* **86** (1986) 43.
- [19] M. Greiter, *Is electromagnetic gauge invariance spontaneously violated in superconductors?*, *Annals of Physics* **319** (Sept., 2005) 217–249, [[cond-mat/0503400](#)].
- [20] S. S. Gubser, *Breaking an Abelian gauge symmetry near a black hole horizon*, *Phys. Rev.* **D78** (2008) 065034, [[arXiv:0801.2977](#)].
- [21] S. A. Hartnoll, C. P. Herzog, and G. T. Horowitz, *Building a Holographic Superconductor*, *Phys. Rev. Lett.* **101** (2008) 031601, [[arXiv:0803.3295](#)].
- [22] S. A. Hartnoll, C. P. Herzog, and G. T. Horowitz, *Holographic Superconductors*, *JHEP* **12** (2008) 015, [[arXiv:0810.1563](#)].
- [23] J. D. Bekenstein, *Black hole hair: 25 - years after*, in *Physics. Proceedings, 2nd International A.D. Sakharov Conference, Moscow, Russia, May 20-24, 1996*, pp. 216–219, 1996. [[gr-qc/9605059](#)].
- [24] T. Hertog, *Towards a Novel no-hair Theorem for Black Holes*, *Phys. Rev.* **D74** (2006) 084008, [[gr-qc/0608075](#)].
- [25] G. T. Horowitz and M. M. Roberts, *Holographic Superconductors with Various Condensates*, *Phys. Rev.* **D78** (2008) 126008, [[arXiv:0810.1077](#)].

- [26] R.-G. Cai, L. Li, L.-F. Li, and R.-Q. Yang, *Introduction to Holographic Superconductor Models*, *Sci. China Phys. Mech. Astron.* **58** (2015), no. 6 060401, [arXiv:1502.00437].
- [27] S. S. Gubser and S. S. Pufu, *The Gravity dual of a p-wave superconductor*, *JHEP* **11** (2008) 033, [arXiv:0805.2960].
- [28] M. M. Roberts and S. A. Hartnoll, *Pseudogap and time reversal breaking in a holographic superconductor*, *JHEP* **08** (2008) 035, [arXiv:0805.3898].
- [29] C. Kallin and A. J. Berlinsky, *Is Sr_2RuO_4 a chiral p-wave superconductor?*, *Journal of Physics Condensed Matter* **21** (Apr., 2009) 164210, [arXiv:0902.2170].
- [30] Y. Maeno, S. Kittaka, T. Nomura, S. Yonezawa, and K. Ishida, *Evaluation of Spin-Triplet Superconductivity in Sr_2RuO_4* , *Journal of the Physical Society of Japan* **81** (Jan., 2012) 011009–011009, [arXiv:1112.1620].
- [31] B. D. Josephson, *Possible new effects in superconductive tunnelling*, *Phys. Lett.* **1** (1962) 251–253.
- [32] M. Tinkham, *Introduction to Superconductivity*. Dover Publications, second edition ed., 2004.
- [33] G. T. Horowitz, J. E. Santos, and B. Way, *A Holographic Josephson Junction*, *Phys. Rev. Lett.* **106** (2011) 221601, [arXiv:1101.3326].
- [34] P. Calabrese and J. L. Cardy, *Entanglement entropy and quantum field theory: A Non-technical introduction*, *Int. J. Quant. Inf.* **4** (2006) 429, [quant-ph/0505193].
- [35] L. Bombelli, R. K. Koul, J. Lee, and R. D. Sorkin, *Quantum source of entropy for black holes*, *Phys. Rev. D* **34** (Jul, 1986) 373–383.
- [36] M. Srednicki, *Entropy and area*, *Phys. Rev. Lett.* **71** (1993) 666–669, [hep-th/9303048].
- [37] R. Emparan, *Black hole entropy as entanglement entropy: A Holographic derivation*, *JHEP* **06** (2006) 012, [hep-th/0603081].
- [38] S. Ryu and T. Takayanagi, *Holographic derivation of entanglement entropy from AdS/CFT*, *Phys.Rev.Lett.* **96** (2006) 181602, [hep-th/0603001].

- [39] S. Ryu and T. Takayanagi, *Aspects of Holographic Entanglement Entropy*, *JHEP* **0608** (2006) 045, [[hep-th/0605073](#)].
- [40] R. Bousso, *A Covariant entropy conjecture*, *JHEP* **07** (1999) 004, [[hep-th/9905177](#)].
- [41] V. E. Hubeny, M. Rangamani, and T. Takayanagi, *A Covariant holographic entanglement entropy proposal*, *JHEP* **0707** (2007) 062, [[arXiv:0705.0016](#)].
- [42] E. Poisson, *A Relativist's Toolkit: The Mathematics of Black-Hole Mechanics*. Cambridge University Press, 2004.
- [43] A. Lewkowycz and J. Maldacena, *Generalized gravitational entropy*, *JHEP* **08** (2013) 090, [[arXiv:1304.4926](#)].
- [44] X. Dong, A. Lewkowycz, and M. Rangamani, *Deriving covariant holographic entanglement*, *JHEP* **11** (2016) 028, [[arXiv:1607.07506](#)].
- [45] M. Headrick, V. E. Hubeny, A. Lawrence, and M. Rangamani, *Causality & holographic entanglement entropy*, *JHEP* **1412** (2014) 162, [[arXiv:1408.6300](#)].
- [46] M. Headrick, *General properties of holographic entanglement entropy*, *JHEP* **03** (2014) 085, [[arXiv:1312.6717](#)].
- [47] H. Liu and S. J. Suh, *Entanglement Tsunami: Universal Scaling in Holographic Thermalization*, *Phys. Rev. Lett.* **112** (2014) 011601, [[arXiv:1305.7244](#)].
- [48] H. Ebrahim and M. Headrick, *Instantaneous Thermalization in Holographic Plasmas*, [arXiv:1010.5443](#).
- [49] T. Albash and C. V. Johnson, *Evolution of Holographic Entanglement Entropy after Thermal and Electromagnetic Quenches*, *New J.Phys.* **13** (2011) 045017, [[arXiv:1008.3027](#)].
- [50] J. Abajo-Arastia, J. Aparicio, and E. Lopez, *Holographic Evolution of Entanglement Entropy*, *JHEP* **1011** (2010) 149, [[arXiv:1006.4090](#)].
- [51] V. Balasubramanian, A. Bernamonti, J. de Boer, N. Copland, B. Craps, et al., *Thermalization of Strongly Coupled Field Theories*, *Phys.Rev.Lett.* **106** (2011) 191601, [[arXiv:1012.4753](#)].

- [52] V. Balasubramanian, A. Bernamonti, J. de Boer, N. Copland, B. Craps, et al., *Holographic Thermalization*, *Phys.Rev.* **D84** (2011) 026010, [arXiv:1103.2683].
- [53] V. Balasubramanian, A. Bernamonti, N. Copland, B. Craps, and F. Galli, *Thermalization of mutual and tripartite information in strongly coupled two dimensional conformal field theories*, *Phys.Rev.* **D84** (2011) 105017, [arXiv:1110.0488].
- [54] A. Allais and E. Tonni, *Holographic evolution of the mutual information*, *JHEP* **1201** (2012) 102, [arXiv:1110.1607].
- [55] J. Aparicio and E. Lopez, *Evolution of Two-Point Functions from Holography*, *JHEP* **1112** (2011) 082, [arXiv:1109.3571].
- [56] V. Keranen, E. Keski-Vakkuri, and L. Thorlacius, *Thermalization and entanglement following a non-relativistic holographic quench*, *Phys.Rev.* **D85** (2012) 026005, [arXiv:1110.5035].
- [57] E. Caceres and A. Kundu, *Holographic Thermalization with Chemical Potential*, *JHEP* **1209** (2012) 055, [arXiv:1205.2354].
- [58] D. Galante and M. Schvellinger, *Thermalization with a chemical potential from AdS spaces*, *JHEP* **1207** (2012) 096, [arXiv:1205.1548].
- [59] V. Balasubramanian, A. Bernamonti, J. de Boer, B. Craps, L. Franti, et al., *Inhomogeneous holographic thermalization*, *JHEP* **1310** (2013) 082, [arXiv:1307.7086].
- [60] P. Fonda, L. Franti, V. Keränen, E. Keski-Vakkuri, L. Thorlacius, et al., *Holographic thermalization with Lifshitz scaling and hyperscaling violation*, *JHEP* **1408** (2014) 051, [arXiv:1401.6088].
- [61] H. Liu and S. J. Suh, *Entanglement growth during thermalization in holographic systems*, *Phys. Rev.* **D89** (2014), no. 6 066012, [arXiv:1311.1200].
- [62] P. Calabrese and J. L. Cardy, *Evolution of entanglement entropy in one-dimensional systems*, *J.Stat.Mech.* **0504** (2005) P04010, [cond-mat/0503393].
- [63] H. Casini, H. Liu, and M. Mezei, *Spread of entanglement and causality*, arXiv:1509.05044.

- [64] R. Emparan, R. Suzuki, and K. Tanabe, *The large D limit of General Relativity*, *JHEP* **06** (2013) 009, [[arXiv:1302.6382](#)].
- [65] V. Asnin, D. Gorbonos, S. Hadar, B. Kol, M. Levi, and U. Miyamoto, *High and Low Dimensions in The Black Hole Negative Mode*, *Class. Quant. Grav.* **24** (2007) 5527–5540, [[arXiv:0706.1555](#)].
- [66] R. Gregory and R. Laflamme, *Black strings and p -branes are unstable*, *Phys. Rev. Lett.* **70** (1993) 2837–2840, [[hep-th/9301052](#)].
- [67] R. Gregory and R. Laflamme, *The Instability of charged black strings and p -branes*, *Nucl. Phys.* **B428** (1994) 399–434, [[hep-th/9404071](#)].
- [68] G. T. Horowitz and K. Maeda, *Fate of the black string instability*, *Phys. Rev. Lett.* **87** (2001) 131301, [[hep-th/0105111](#)].
- [69] L. Lehner and F. Pretorius, *Final State of Gregory-Laflamme Instability*, [arXiv:1106.5184](#).
- [70] E. Sorkin, *A Critical dimension in the black string phase transition*, *Phys. Rev. Lett.* **93** (2004) 031601, [[hep-th/0402216](#)].
- [71] R. Emparan, R. Suzuki, and K. Tanabe, *Evolution and End Point of the Black String Instability: Large D Solution*, *Phys. Rev. Lett.* **115** (2015), no. 9 091102, [[arXiv:1506.06772](#)].
- [72] R. Suzuki and K. Tanabe, *Non-uniform black strings and the critical dimension in the $1/D$ expansion*, *JHEP* **10** (2015) 107, [[arXiv:1506.01890](#)].
- [73] P. M. Chesler and L. G. Yaffe, *Numerical solution of gravitational dynamics in asymptotically anti-de Sitter spacetimes*, *JHEP* **1407** (2014) 086, [[arXiv:1309.1439](#)].
- [74] X.-L. Qi and S.-C. Zhang, *Topological insulators and superconductors*, *Rev. Mod. Phys.* **83** (Oct, 2011) 1057–1110.
- [75] M. Z. Hasan and C. L. Kane, *Colloquium*, *Rev. Mod. Phys.* **82** (Nov, 2010) 3045–3067.
- [76] J. Alicea, *New directions in the pursuit of Majorana fermions in solid state systems*, *Reports on Progress in Physics* **75** (July, 2012) 076501, [[arXiv:1202.1293](#)].

- [77] L. Fu and C. L. Kane, *Superconducting proximity effect and majorana fermions at the surface of a topological insulator*, *Phys. Rev. Lett.* **100** (Mar, 2008) 096407.
- [78] N. Read and D. Green, *Paired states of fermions in two-dimensions with breaking of parity and time reversal symmetries, and the fractional quantum Hall effect*, *Phys. Rev.* **B61** (2000) 10267, [[cond-mat/9906453](#)].
- [79] C. W. Hicks, J. R. Kirtley, T. M. Lippman, N. C. Koshnick, M. E. Huber, Y. Maeno, W. M. Yuhasz, M. B. Maple, and K. A. Moler, *Limits on superconductivity-related magnetization in Sr_2RuO_4 and $\text{PrOs}_4\text{Sb}_{12}$ from scanning squid microscopy*, *Phys. Rev. B* **81** (Jun, 2010) 214501.
- [80] M. Stone and R. Roy, *Edge modes, edge currents, and gauge invariance in p_x+ip_y superfluids and superconductors*, *Phys. Rev. B* **69** (May, 2004) 184511.
- [81] S. S. Gubser, *Colorful horizons with charge in anti-de Sitter space*, *Phys. Rev. Lett.* **101** (2008) 191601, [[arXiv:0803.3483](#)].
- [82] E. Kiritsis and V. Niarchos, *Josephson Junctions and AdS/CFT Networks*, *JHEP* **07** (2011) 112, [[arXiv:1105.6100](#)]. [Erratum: *JHEP*10,095(2011)].
- [83] Y.-Q. Wang, Y.-X. Liu, and Z.-H. Zhao, *Holographic p-wave Josephson junction*, [arXiv:1109.4426](#).
- [84] Y.-Q. Wang, Y.-X. Liu, R.-G. Cai, S. Takeuchi, and H.-Q. Zhang, *Holographic SIS Josephson Junction*, *JHEP* **09** (2012) 058, [[arXiv:1205.4406](#)].
- [85] J. R. Williams, A. J. Bestwick, P. Gallagher, S. S. Hong, Y. Cui, A. S. Bleich, J. G. Analytis, I. R. Fisher, and D. Goldhaber-Gordon, *Unconventional josephson effect in hybrid superconductor-topological insulator devices*, *Phys. Rev. Lett.* **109** (Jul, 2012) 056803.
- [86] I. Sochnikov, A. J. Bestwick, J. R. Williams, T. M. Lippman, I. R. Fisher, D. Goldhaber-Gordon, J. R. Kirtley, and K. A. Moler, *Direct measurement of current-phase relations in superconductor/topological insulator/superconductor junctions*, *Nano Letters* **13** (2013), no. 7 3086–3092, [<http://dx.doi.org/10.1021/nl400997k>]. PMID: 23795666.

- [87] A. Y. Kitaev, *Unpaired Majorana fermions in quantum wires*, *Phys. Usp.* **44** (2001), no. 10S 131–136.
- [88] Kwon, H.-J., Sengupta, K., and Yakovenko, V. M., *Fractional ac josephson effect in p- and d-wave superconductors*, *Eur. Phys. J. B* **37** (2004), no. 3 349–361.
- [89] L. Jiang, D. Pekker, J. Alicea, G. Refael, Y. Oreg, A. Brataas, and F. von Oppen, *Magneto-josephson effects in junctions with majorana bound states*, *Phys. Rev. B* **87** (Feb, 2013) 075438.
- [90] L. Fu and C. L. Kane, *Josephson current and noise at a superconductor/quantum-spin-hall-insulator/superconductor junction*, *Phys. Rev. B* **79** (Apr, 2009) 161408.
- [91] L. Jiang, D. Pekker, J. Alicea, G. Refael, Y. Oreg, and F. von Oppen, *Unconventional josephson signatures of majorana bound states*, *Phys. Rev. Lett.* **107** (Nov, 2011) 236401.
- [92] G. P. A. Barone, *Physics and Applications of the Josephson Effect*. John Wiley & Sons, New York, 1982.
- [93] P. Calabrese and J. L. Cardy, *Time-dependence of correlation functions following a quantum quench*, *Phys.Rev.Lett.* **96** (2006) 136801, [[cond-mat/0601225](#)].
- [94] P. Calabrese and J. Cardy, *Quantum Quenches in Extended Systems*, *J.Stat.Mech.* **0706** (2007) P06008, [[arXiv:0704.1880](#)].
- [95] P. M. Chesler and L. G. Yaffe, *Horizon formation and far-from-equilibrium isotropization in supersymmetric Yang-Mills plasma*, *Phys.Rev.Lett.* **102** (2009) 211601, [[arXiv:0812.2053](#)].
- [96] S. Bhattacharyya and S. Minwalla, *Weak Field Black Hole Formation in Asymptotically AdS Spacetimes*, *JHEP* **0909** (2009) 034, [[arXiv:0904.0464](#)].
- [97] S. R. Das, T. Nishioka, and T. Takayanagi, *Probe Branes, Time-dependent Couplings and Thermalization in AdS/CFT*, *JHEP* **1007** (2010) 071, [[arXiv:1005.3348](#)].
- [98] V. E. Hubeny and M. Rangamani, *A Holographic view on physics out of equilibrium*, *Adv.High Energy Phys.* **2010** (2010) 297916, [[arXiv:1006.3675](#)].

- [99] P. Basu and S. R. Das, *Quantum Quench across a Holographic Critical Point*, *JHEP* **1201** (2012) 103, [[arXiv:1109.3909](#)].
- [100] A. Buchel, L. Lehner, and R. C. Myers, *Thermal quenches in $N=2^*$ plasmas*, *JHEP* **1208** (2012) 049, [[arXiv:1206.6785](#)].
- [101] M. Bhaseen, J. P. Gauntlett, B. Simons, J. Sonner, and T. Wiseman, *Holographic Superfluids and the Dynamics of Symmetry Breaking*, *Phys.Rev.Lett.* **110** (2013) 015301, [[arXiv:1207.4194](#)].
- [102] P. Basu, D. Das, S. R. Das, and T. Nishioka, *Quantum Quench Across a Zero Temperature Holographic Superfluid Transition*, *JHEP* **1303** (2013) 146, [[arXiv:1211.7076](#)].
- [103] V. E. Hubeny, M. Rangamani, and E. Tonni, *Thermalization of Causal Holographic Information*, *JHEP* **1305** (2013) 136, [[arXiv:1302.0853](#)].
- [104] M. Nozaki, T. Numasawa, and T. Takayanagi, *Holographic Local Quenches and Entanglement Density*, *JHEP* **05** (2013) 080, [[arXiv:1302.5703](#)].
- [105] A. Buchel, L. Lehner, R. C. Myers, and A. van Niekerk, *Quantum quenches of holographic plasmas*, *JHEP* **1305** (2013) 067, [[arXiv:1302.2924](#)].
- [106] T. Hartman and J. Maldacena, *Time Evolution of Entanglement Entropy from Black Hole Interiors*, *JHEP* **1305** (2013) 014, [[arXiv:1303.1080](#)].
- [107] P. Basu, D. Das, S. R. Das, and K. Sengupta, *Quantum Quench and Double Trace Couplings*, *JHEP* **1312** (2013) 070, [[arXiv:1308.4061](#)].
- [108] A. Buchel, R. C. Myers, and A. van Niekerk, *Universality of Abrupt Holographic Quenches*, *Phys.Rev.Lett.* **111** (2013) 201602, [[arXiv:1307.4740](#)].
- [109] C. T. Asplund and A. Bernamonti, *Mutual information after a local quench in conformal field theory*, *Phys. Rev.* **D89** (2014), no. 6 066015, [[arXiv:1311.4173](#)].
- [110] J. Abajo-Arrastia, E. da Silva, E. Lopez, J. Mas, and A. Serantes, *Holographic Relaxation of Finite Size Isolated Quantum Systems*, *JHEP* **1405** (2014) 126, [[arXiv:1403.2632](#)].

- [111] A. F. Astaneh and A. E. Mosaffa, *Quantum Local Quench, AdS/BCFT and Yo-Yo String*, *JHEP* **05** (2015) 107, [arXiv:1405.5469].
- [112] A. Buchel, R. C. Myers, and A. van Niekerk, *Nonlocal probes of thermalization in holographic quenches with spectral methods*, arXiv:1410.6201.
- [113] S. R. Das, D. A. Galante, and R. C. Myers, *Universality in fast quantum quenches*, *JHEP* **02** (2015) 167, [arXiv:1411.7710].
- [114] X. Bai, B.-H. Lee, L. Li, J.-R. Sun, and H.-Q. Zhang, *Time Evolution of Entanglement Entropy in Quenched Holographic Superconductors*, *JHEP* **04** (2015) 066, [arXiv:1412.5500].
- [115] M. Rangamani, M. Rozali, and A. Wong, *Driven Holographic CFTs*, *JHEP* **04** (2015) 093, [arXiv:1502.05726].
- [116] S. Leichenauer and M. Moosa, *Entanglement Tsunami in (1+1)-Dimensions*, arXiv:1505.04225.
- [117] S. R. Das, D. A. Galante, and R. C. Myers, *Smooth and fast versus instantaneous quenches in quantum field theory*, *JHEP* **08** (2015) 073, [arXiv:1505.05224].
- [118] C. Ecker, D. Grumiller, and S. A. Stricker, *Evolution of holographic entanglement entropy in an anisotropic system*, *JHEP* **07** (2015) 146, [arXiv:1506.02658].
- [119] V. Ziogas, *Holographic mutual information in global Vaidya-BTZ spacetime*, *JHEP* **09** (2015) 114, [arXiv:1507.00306].
- [120] K. A. Sohrabi, *Inhomogeneous Thermal Quenches*, arXiv:1509.00245.
- [121] G. Camilo, B. Cuadros-Melgar, and E. Abdalla, *Holographic quenches towards a Lifshitz point*, arXiv:1511.08843.
- [122] U. H. Danielsson, E. Keski-Vakkuri, and M. Kruczenski, *Black hole formation in AdS and thermalization on the boundary*, *JHEP* **0002** (2000) 039, [hep-th/9912209].
- [123] H. Casini, *Geometric entropy, area, and strong subadditivity*, *Class. Quant. Grav.* **21** (2004) 2351–2378, [hep-th/0312238].

- [124] C. T. Asplund, A. Bernamonti, F. Galli, and T. Hartman, *Holographic Entanglement Entropy from 2d CFT: Heavy States and Local Quenches*, *JHEP* **02** (2015) 171, [[arXiv:1410.1392](#)].
- [125] C. T. Asplund, A. Bernamonti, F. Galli, and T. Hartman, *Entanglement Scrambling in 2d Conformal Field Theory*, *JHEP* **09** (2015) 110, [[arXiv:1506.03772](#)].
- [126] V. E. Hubeny and H. Maxfield, *Holographic probes of collapsing black holes*, *JHEP* **1403** (2014) 097, [[arXiv:1312.6887](#)].
- [127] J. P. Boyd, *Chebyshev and Fourier spectral methods*. Dover Publications, 2001.
- [128] S. Bhattacharyya, V. E. Hubeny, R. Loganayagam, G. Mandal, S. Minwalla, et al., *Local Fluid Dynamical Entropy from Gravity*, *JHEP* **0806** (2008) 055, [[arXiv:0803.2526](#)].
- [129] E. H. Lieb and D. W. Robinson, *The finite group velocity of quantum spin systems*, *Commun. Math. Phys.* **28** (1972) 251–257.
- [130] V. Eisler and I. Peschel, *Evolution of entanglement after a local quench*, *Journal of Statistical Mechanics: Theory and Experiment* **6** (June, 2007) 5, [[cond-mat/0703379](#)].
- [131] P. Hayden and J. Preskill, *Black holes as mirrors: Quantum information in random subsystems*, *JHEP* **09** (2007) 120, [[arXiv:0708.4025](#)].
- [132] Y. Sekino and L. Susskind, *Fast Scramblers*, *JHEP* **10** (2008) 065, [[arXiv:0808.2096](#)].
- [133] J. Cardy, *Quantum Quenches to a Critical Point in One Dimension: some further results*, [arXiv:1507.07266](#).
- [134] M. Rangamani, M. Rozali, and A. Vincart-Emard, *work in progress*, .
- [135] M. Mezei and D. Stanford, *On entanglement spreading in chaotic systems*, [arXiv:1608.05101](#).
- [136] M. Mezei, *On entanglement spreading from holography*, [arXiv:1612.00082](#).

- [137] M. Rangamani, M. Rozali, and A. Vincart-Emard, *Dynamics of Holographic Entanglement Entropy Following a Local Quench*, *JHEP* **04** (2016) 069, [[arXiv:1512.03478](#)].
- [138] A. Buchel, M. P. Heller, and R. C. Myers, *Equilibration rates in a strongly coupled nonconformal quark-gluon plasma*, *Phys. Rev. Lett.* **114** (2015), no. 25 251601, [[arXiv:1503.07114](#)].
- [139] J. F. Fuini and L. G. Yaffe, *Far-from-equilibrium dynamics of a strongly coupled non-Abelian plasma with non-zero charge density or external magnetic field*, *JHEP* **07** (2015) 116, [[arXiv:1503.07148](#)].
- [140] K. Balasubramanian and C. P. Herzog, *Losing Forward Momentum Holographically*, *Class.Quant.Grav.* **31** (2014) 125010, [[arXiv:1312.4953](#)].
- [141] V. Balasubramanian and P. Kraus, *A Stress tensor for Anti-de Sitter gravity*, *Commun. Math. Phys.* **208** (1999) 413–428, [[hep-th/9902121](#)].
- [142] D. A. Roberts, D. Stanford, and L. Susskind, *Localized shocks*, *JHEP* **03** (2015) 051, [[arXiv:1409.8180](#)].
- [143] S. H. Shenker and D. Stanford, *Stringy effects in scrambling*, *JHEP* **05** (2015) 132, [[arXiv:1412.6087](#)].
- [144] M. Alishahiha, A. Davody, A. Naseh, and S. F. Taghavi, *On Butterfly effect in Higher Derivative Gravities*, *JHEP* **11** (2016) 032, [[arXiv:1610.02890](#)].
- [145] M. Alishahiha, A. F. Astaneh, and M. R. Mohammadi Mozaffar, *Thermalization in backgrounds with hyperscaling violating factor*, *Phys. Rev.* **D90** (2014), no. 4 046004, [[arXiv:1401.2807](#)].
- [146] R. Baier, P. Romatschke, D. T. Son, A. O. Starinets, and M. A. Stephanov, *Relativistic viscous hydrodynamics, conformal invariance, and holography*, *JHEP* **04** (2008) 100, [[arXiv:0712.2451](#)].
- [147] S. Bhattacharyya, R. Loganayagam, I. Mandal, S. Minwalla, and A. Sharma, *Conformal Nonlinear Fluid Dynamics from Gravity in Arbitrary Dimensions*, *JHEP* **12** (2008) 116, [[arXiv:0809.4272](#)].
- [148] T. Harmark, V. Niarchos, and N. A. Obers, *Instabilities of black strings and branes*, *Class. Quant. Grav.* **24** (2007) R1–R90, [[hep-th/0701022](#)].

- [149] M. W. Choptuik, L. Lehner, I. Olabarrieta, R. Petryk, F. Pretorius, and H. Villegas, *Towards the final fate of an unstable black string*, *Phys. Rev.* **D68** (2003) 044001, [[gr-qc/0304085](#)].
- [150] R. Emparan, K. Izumi, R. Luna, R. Suzuki, and K. Tanabe, *Hydro-elastic Complementarity in Black Branes at large D*, [arXiv:1602.05752](#).
- [151] S. Bhattacharyya, M. Mandlik, S. Minwalla, and S. Thakur, *A Charged Membrane Paradigm at Large D*, [arXiv:1511.03432](#).
- [152] M. M. Caldarelli, R. Emparan, and B. Van Pol, *Higher-dimensional Rotating Charged Black Holes*, *JHEP* **04** (2011) 013, [[arXiv:1012.4517](#)].
- [153] J. Camps, R. Emparan, and N. Haddad, *Black Brane Viscosity and the Gregory-Laflamme Instability*, *JHEP* **05** (2010) 042, [[arXiv:1003.3636](#)].
- [154] J. Gath and A. V. Pedersen, *Viscous asymptotically flat Reissner-Nordstrom black branes*, *JHEP* **03** (2014) 059, [[arXiv:1302.5480](#)].
- [155] R. Emparan, R. Suzuki, and K. Tanabe, *Decoupling and non-decoupling dynamics of large D black holes*, *JHEP* **07** (2014) 113, [[arXiv:1406.1258](#)].
- [156] C. P. Herzog, M. Spillane, and A. Yarom, *The holographic dual of a Riemann problem in a large number of dimensions*, *JHEP* **08** (2016) 120, [[arXiv:1605.01404](#)].
- [157] A. Donos and J. P. Gauntlett, *On the thermodynamics of periodic AdS black branes*, *JHEP* **10** (2013) 038, [[arXiv:1306.4937](#)].
- [158] A. Donos and J. P. Gauntlett, *Minimally packed phases in holography*, *JHEP* **03** (2016) 148, [[arXiv:1512.06861](#)].
- [159] T. Faulkner, G. T. Horowitz, J. McGreevy, M. M. Roberts, and D. Vegh, *Photoemission 'experiments' on holographic superconductors*, *JHEP* **03** (2010) 121, [[arXiv:0911.3402](#)].
- [160] G. T. Horowitz, J. E. Santos, and D. Tong, *Optical Conductivity with Holographic Lattices*, *JHEP* **07** (2012) 168, [[arXiv:1204.0519](#)].

- [161] T. Andrade and S. A. Gentle, *Relaxed superconductors*, *JHEP* **06** (2015) 140, [[arXiv:1412.6521](#)].
- [162] W. Fischler, A. Kundu, and S. Kundu, *Holographic Mutual Information at Finite Temperature*, *Phys. Rev.* **D87** (2013), no. 12 126012, [[arXiv:1212.4764](#)].
- [163] A. Almheiri, X. Dong, and D. Harlow, *Bulk Locality and Quantum Error Correction in AdS/CFT*, *JHEP* **04** (2015) 163, [[arXiv:1411.7041](#)].
- [164] F. Pastawski, B. Yoshida, D. Harlow, and J. Preskill, *Holographic quantum error-correcting codes: Toy models for the bulk/boundary correspondence*, *JHEP* **06** (2015) 149, [[arXiv:1503.06237](#)].
- [165] N. Bao, C. Cao, S. M. Carroll, A. Chatwin-Davies, N. Hunter-Jones, J. Pollack, and G. N. Remmen, *Consistency conditions for an AdS multiscale entanglement renormalization ansatz correspondence*, *Phys. Rev.* **D91** (2015), no. 12 125036, [[arXiv:1504.06632](#)].
- [166] P. M. Chesler and W. van der Schee, *Early thermalization, hydrodynamics and energy loss in AdS/CFT*, *Int. J. Mod. Phys.* **E24** (2015), no. 10 1530011, [[arXiv:1501.04952](#)].
- [167] R. Emparan and K. Tanabe, *Holographic superconductivity in the large D expansion*, *JHEP* **01** (2014) 145, [[arXiv:1312.1108](#)].
- [168] J. Yopez, *Einstein's vierbein field theory of curved space*, [arXiv:1106.2037](#).

Appendix A

Apparent Horizons

In chapters 3 and 4 we used the residual radial reparametrization freedom of the metric to fix the coordinate location of the black hole's apparent horizon. Here we provide some details on the process we used.

The notion of apparent horizon depends on the existence of trapped surfaces, which in turn depends on the chosen foliation of spacetime. Given a spacelike surface \mathcal{S} , a trapped surface on \mathcal{S} corresponds to the region where both ingoing and outgoing future-directed null geodesic congruences orthogonal to \mathcal{S} have non-positive expansions. The apparent horizon is then defined as the boundary of this trapped region, on which the geodesic congruences have vanishing expansions.

In our case, a planar spacelike surface like the apparent horizon can be parametrized by the two orthogonal vector fields spanning the x and y directions:

$$e_x^M = (0, 0, 1, 0), \quad e_y^M = (0, 0, 0, 1). \quad (\text{A.1})$$

We now construct future-directed null geodesic congruences orthogonal to both e_x and e_y . Ingoing geodesic congruences can be parametrized by the tangent null vector field $k^M = (0, -1, 0, 0)$, whereas outgoing geodesic congruences have

$$N^M = e^{-2\chi} \left(1, A + e^{-2\chi} \frac{e^{-B} F_x^2}{2\Sigma^2}, \frac{e^{-B} F_x}{\Sigma^2}, 0 \right). \quad (\text{A.2})$$

The normalization is chosen such that $g_{MN} k^M N^N = -1$. Since we are interested in the rate of change of the cross-sectional area of null geodesic congruences along their transverse directions, we need to define the transverse metric

$$h_{MN} = g_{MN} + k_M N_N + N_M k_N. \quad (\text{A.3})$$

With this in hand, we can calculate the expansion¹ $\theta \equiv h^{MN} \nabla_M N_N$. Setting

¹The expansion for the ingoing geodesic congruences is always negative, so we need only worry about the congruences along N .

$\theta = 0$ yields a condition on the dynamics of the field Σ :

$$\left[d_+ \Sigma - \frac{e^{-B}}{2\Sigma} \left(F_x \partial_x B - \partial_x F_x - e^{-2\chi} F_x^2 \frac{\partial_r \Sigma}{\Sigma} \right) \right]_{r=r_h} = 0, \quad (\text{A.4})$$

where $d_+ \equiv \partial_t + A \partial_r$. In addition, taking a time derivative of this relation yields a stationarity condition that ensures that the horizon condition holds for all times. One can show that the resulting constraint can be expressed as a second order spatial ODE that determines the value of $A(r, t, x)$ at the (fixed) apparent horizon.

Appendix B

Numerical Implementation of Characteristic Formulation

The characteristic formulation of Einstein's equations in the presence of matter reorganizes all the fields into two categories: auxiliary fields obeying radial ODEs that can be solved sequentially, and dynamical fields which are used to evolve the geometry from one null slice to the next. This separation of fields can be achieved by expressing time derivatives in terms of the directional derivative along outgoing null geodesics, $d_+ = \partial_t + A \partial_r$, thereby completely eliminating the presence of A from the auxiliary equations. Changing to a compact variable $u = 1/r$, we rewrite the fields appearing in our equations as

$$\begin{aligned}
\Phi(u, t, x) &\equiv \phi(u, t, x)u, \\
E_r(u, t, x) &\equiv e_r(u, t, x)u^2, \\
\Sigma(u, t, x) &\equiv \frac{1 + \lambda(t, x)u}{u} - \frac{1}{4}\phi(u, t, x)^2u, \\
B(u, t, x) &\equiv b(u, t, x)u^2, \\
\chi(u, t, x) &\equiv c(u, t, x)u^2, \\
F_x(u, t, x) &\equiv -\partial_x \lambda(t, x) + f_x(u, t, x), \\
d_+ \Sigma(u, t, x) &\equiv \frac{(1 + \lambda(t, x)u)^2}{2u^2} + \tilde{\Sigma}(u, t, x), \\
d_+ \Phi(u, t, x) &\equiv -\frac{1}{2}\phi(u, t, x) + \left(\tilde{\Phi}(u, t, x) + \frac{1}{2}\partial_u \phi(u, t, x) \right), \\
d_+ B(u, t, x) &\equiv \tilde{B}(u, t, x)u^2, \\
A(u, t, x) &\equiv \frac{(1 + \lambda(t, x)u)^2}{2u^2} + a(u, t, x),
\end{aligned} \tag{B.1}$$

in order to subtract the divergent parts. The field $E_r(r, t, x)$ above is defined as

$$E_r = \partial_r V_0 + \frac{e^{-B}}{\Sigma^2} F_x \partial_r V_x \sim F^{tr} \tag{B.2}$$

in order to decouple the radial equations satisfied by V_0 and F_x . However we note that the equations for d_+B and d_+V_x form a linear system of radial ODEs that cannot be decoupled.

Given initial conditions specified by ϕ , λ , b and V_x all being 0, as well as the CFT data T_{00} and T_{tx} , we can solve the radial ODEs for the auxiliary fields c , e_r , f_x , V_0 , $\tilde{\Sigma}$, $\tilde{\Phi}$, and for the coupled system \tilde{B} and d_+V_x , in that order. These fields obey the boundary conditions

$$\partial_u c(u=0) = -\frac{1}{12}\lambda\phi_0^2 + \frac{1}{6}\phi_0\phi_1, \quad (\text{B.3})$$

$$e_r(u=0) = \rho, \quad (\text{B.4})$$

$$f_x(u=0) = 0 \quad \text{and} \quad \partial_u f_x(u=0) = f^{(3)} = \frac{2}{3}T_{tx} + \frac{1}{3}\phi_0\partial_x\phi_0, \quad (\text{B.5})$$

$$V_0(u=0) = \mu, \quad (\text{B.6})$$

$$\tilde{\Phi}(u=0) = -\phi_1 - \lambda\phi_0 + \partial_t\phi_0, \quad (\text{B.7})$$

$$\begin{aligned} \tilde{B}(u=0) = \frac{1}{6} \left((\partial_x\phi_0)^2 - \frac{1}{2}\phi_0\partial_x^2\phi_0 - \partial_x T_{tx} \right) \\ - \frac{1}{2}j_x \left(\partial_t\mu_x - \partial_x\mu - \frac{1}{2}j_x \right) - \frac{1}{2}\partial_u^2 b \Big|_{u=0}, \end{aligned} \quad (\text{B.8})$$

$$d_+V_x(u=0) = \partial_t\mu_x - \frac{1}{2}j_x. \quad (\text{B.9})$$

There are two options when treating with the field $\tilde{\Sigma}$, one of which is to impose the condition

$$\left[d_+\Sigma - \frac{e^{-B}}{2\Sigma} \left(F_x \partial_x B - \partial_x F_x - e^{-2\chi} F_x^2 \frac{\partial_r \Sigma}{\Sigma} \right) \right]_{r=r_h} = 0, \quad (\text{B.10})$$

which determines the location of the apparent horizon as the boundary of trapped surfaces, as derived in Appendix A. Our second option is to set

$$\partial_u \tilde{\Sigma}(u=0) = \frac{1}{2}T_{00} - \frac{1}{3}\phi_0\phi_1 - \frac{1}{12}\lambda\phi_0^2 \quad (\text{B.11})$$

on the boundary, as required by self-consistency of the equations of motion. Either conditions imply the other; imposing the latter should yield the former and vice-versa, and we can use this as a safety check for our numerics.

Now that we have solved for the necessary auxiliary fields, we have to propagate the solutions along null slices. In order to propagate λ , we re-

quire a horizon stationarity condition, obtained by differentiating (B.10) with respect to time, thus ensuring that the location of the apparent horizon remains fixed on all null slices. This procedure yields a boundary value problem in x for the field $A(u_h, t, x)$. We can then extract $\partial_t \lambda$ from the relation

$$d_+ \Sigma = \partial_t \lambda + A - d_+ \left(\frac{1}{4} \phi^2 \right) \quad (\text{B.12})$$

evaluated at the horizon. The same equation in turn enables us to solve for A everywhere in the bulk since λ does not depend on the radial coordinate. With A in hand, it now becomes straightforward to extract the time derivatives for b , ϕ and V_x from the solutions for $d_+ B$, $d_+ \Phi$ and $d_+ V_x$, and from the definition of $d_+ = \partial_t + A \partial_r$. At this point, all that is left to do is propagate these fields with a time-stepping algorithm, along with T_{00} , T_{tx} and ρ using the conservation equations (4.22), (4.23), and (4.24), and to repeat the process on new null time slices until satisfied with the evolution of the quench.

Appendix C

Dimensional Reduction

The framework of general relativity when the number of spacetime dimensions D is large is a novel way to investigate non-perturbative objects like black branes in a $1/D$ expansion that trivializes the gravitational dynamics away from their event horizons. For this expansion to take place, the dependence on D needs to be extracted explicitly from Einstein's equations. For a spherically symmetric spacetime described by

$$ds^2 = g_{\mu\nu}(x)dx^\mu dx^\nu + e^{\phi(x)}d\Omega_d^2, \quad (\text{C.1})$$

where $g_{\mu\nu}(x)$ is the metric of the object of interest and $d\Omega_d^2$ the one on the unit d -sphere, the dependence on d can be made explicit via dimensional reduction.

Cartan's formalism is particularly well-suited for the task at hand [168]. The first step is to reexpress the *coordinate* basis metric (C.1) in terms of a *vierbein* basis $\mathbf{e}^\alpha(x)$ by relating the basis vectors via $dx^\mu = e^\mu_\alpha \mathbf{e}^\alpha$, where e^μ_α denotes the (coordinate-dependent) transformation matrix between the two basis. This leads us to rewrite¹

$$g_{\mu\nu}(x)dx^\mu dx^\nu = \eta_{ab} \mathbf{e}^a(x)\mathbf{e}^b(x), \quad (\text{C.2})$$

and

$$e^{\phi(x)}d\Omega_d^2 = \delta_{ij} \mathbf{e}^i(x, \theta)\mathbf{e}^j(x, \theta), \quad (\text{C.3})$$

where we have used the inner-product constraint $g_{\mu\nu}(x)e^\mu_a(x)e^\nu_b(x) = \eta_{ab}$ (or equivalently $g_{\mu\nu}(x) = e_\mu^a(x)e_\nu^b(x)\eta_{ab}$) that defines the vierbein fields $e^\mu_a(x)$ as the square root of the metric. Also note that $\mathbf{e}^i(x, \theta) = e^{\phi(x)/2}\mathbf{e}_\gamma^i(\theta)$, with $\mathbf{e}_\gamma^i(\theta)$ our basis on S^d .

Another important element of this formalism is the spin connection ω ,

¹We use lowercase latin letters (a, b, \dots) at the start of the alphabet to denote the basis associated with the sector described by $g_{\mu\nu}$, and the letters in the middle (i, j, \dots) to identify that of the d -sphere. These latin indices are raised and lowered by the corresponding flat metric.

which plays the role of the affine connection in the vierbein basis

$$\nabla_{\mu,c} X^a = \partial_{\mu,c} X^a + (\omega_{\mu,c})^a_b X^b, \quad (\text{C.4})$$

$$\nabla_{\mu,c} X_a = \partial_{\mu,c} X_a - (\omega_{\mu,c})^b_a X_b. \quad (\text{C.5})$$

In non-coordinate form, $\omega^a_b = (\omega_\mu)^a_b dx^\mu = (\omega_c)^a_b \mathbf{e}^c$. Additionally, the spin connection is antisymmetric: $\omega_{ab} = -\omega_{ba}$.

We now have all the necessary elements to compute the Riemann tensor in the vierbein basis, which is more tractable analytically. Our first task is to find the spin connection for the metric (C.1) by making use of Cartan's first structure equation, which relates the exterior derivatives² of the vierbein basis $\mathbf{d}\mathbf{e}$ with the spin connection on the manifold via the antisymmetric wedge product

$$\mathbf{d}\mathbf{e}^\alpha = -\omega^\alpha_\beta \wedge \mathbf{e}^\beta. \quad (\text{C.6})$$

On the d -sphere, we expect the spin connection to act separately on both sectors because of the scale factor e^ϕ

$$\mathbf{d}\mathbf{e}^i = -\omega^i_a \wedge \mathbf{e}^a - \omega^i_j \wedge \mathbf{e}^j. \quad (\text{C.7})$$

Extracting the dependence on ϕ explicitly leads us to

$$\mathbf{d}\mathbf{e}^i = \mathbf{d}\left(e^{\phi(x)/2} \mathbf{e}_\gamma^i\right) = \mathbf{d}(e^{\phi/2}) \wedge \mathbf{e}_\gamma^i + e^{\phi/2} \mathbf{d}\mathbf{e}_\gamma^i \quad (\text{C.8})$$

$$= \frac{1}{2} \phi_{,a} \mathbf{e}^a \wedge \mathbf{e}^i - e^{\phi/2} (\omega_\gamma^i_j \wedge \mathbf{e}_\gamma^j) \quad (\text{C.9})$$

$$= -\frac{1}{2} \phi_{,a} \mathbf{e}^i \wedge \mathbf{e}^a - \omega_\gamma^i_j \wedge \mathbf{e}^j, \quad (\text{C.10})$$

from which we learn that $\omega^i_a = \frac{1}{2} \phi_{,a} \mathbf{e}^i$.

In contrast, the $g_{\mu\nu}$ sector is self-contained

$$\mathbf{d}\mathbf{e}^a = -\omega^a_b \wedge \mathbf{e}^b - \omega^a_i \wedge \mathbf{e}^i = -\omega^a_b \wedge \mathbf{e}^b, \quad (\text{C.11})$$

where we have used the fact that the wedge product is antisymmetric, $\mathbf{e}^i \wedge \mathbf{e}^i = 0$.

With the spin connection in hand, we can use Cartan's second structure equation to compute the Riemann tensor \underline{R}

$$\underline{R}^\alpha_\beta = \mathbf{d}\omega^\alpha_\beta + \omega^\alpha_\rho \wedge \omega^\rho_\beta. \quad (\text{C.12})$$

²The exterior derivative of a scalar function is simply $\mathbf{d}\phi = \phi_{,a} \mathbf{e}^a$.

Note that its components may be read from the vierbein basis

$$\underline{R}^\alpha_\beta = \frac{1}{2} R^\alpha_{\beta\rho\sigma} \mathbf{e}^\rho \wedge \mathbf{e}^\sigma. \quad (\text{C.13})$$

It is useful to separate the calculation in three:

- For the Riemann tensor pertaining to the metric $g_{\mu\nu}$ only,

$$\underline{R}^a_b = \underline{R}_g^a_b \quad (\text{C.14})$$

since this sector is self-contained. The corresponding Ricci scalar is then simply $R_1 = R_g$, the one computed from the metric $g_{\mu\nu}$ by usual means.

- For the Riemann tensor pertaining to the d -sphere only,

$$\underline{R}^i_j = \left(\mathbf{d}\omega^i_j + \omega^i_k \wedge \omega^k_j \right) + \omega^i_a \wedge \omega^a_j \quad (\text{C.15})$$

$$= \underline{R}_\gamma^i_j + \omega^i_a \wedge \left(-\eta^{ab} \omega^j_b \right) \quad (\text{C.16})$$

$$= \underline{R}_\gamma^i_j - \frac{1}{4} (\nabla\phi)^2 \mathbf{e}^i \wedge \mathbf{e}^j \quad (\text{C.17})$$

$$= \frac{1}{2} \left(\underline{R}_\gamma^i_{jmn} - \frac{1}{4} (\nabla\phi)^2 (\delta_{im}\delta_{jn} - \delta_{in}\delta_{jm}) \right) \mathbf{e}^m \wedge \mathbf{e}^n. \quad (\text{C.18})$$

Note that we have explicitly antisymmetrized the term proportional to $(\nabla\phi)^2$, in accordance to the Riemann tensor's definition.

To compute the Ricci scalar, we sum the Riemann tensor over its first and third indices and then take the trace

$$R_2 = R_\gamma + \delta^{ij} R^m_{imj} \quad (\text{C.19})$$

$$= R_\gamma - \frac{1}{4} (\nabla\phi)^2 (\delta_{mm}\delta_{ij} - \delta_{mj}\delta_{im}) \delta^{ij} \quad (\text{C.20})$$

$$= R_\gamma - \frac{d(d-1)}{4} (\nabla\phi)^2. \quad (\text{C.21})$$

For a sphere of radius e^ϕ , the Ricci scalar is simply $R_\gamma = d(d+1)e^{-\phi}$.

- For the mixed sector,

$$\underline{R}^i{}_a = \mathbf{d}\omega^i{}_a + \omega^i{}_b \wedge \omega^b{}_a + \omega^i{}_j \wedge \omega^j{}_a \quad (\text{C.22})$$

$$= \mathbf{d} \left(\frac{1}{2} \phi_{,a} \mathbf{e}^i \right) + \left(\frac{1}{2} \phi_{,b} \mathbf{e}^i \right) \wedge \omega_g{}^b{}_a + \omega_\gamma{}^i{}_j \wedge \left(\frac{1}{2} \phi_{,a} \mathbf{e}^j \right) \quad (\text{C.23})$$

$$= \frac{1}{2} \phi_{,ab} \mathbf{e}^b \wedge \mathbf{e}^i + \frac{1}{4} \phi_{,a} \phi_{,b} \mathbf{e}^b \wedge \mathbf{e}^i - \frac{1}{2} \phi_{,a} \omega_\gamma{}^i{}_j \wedge \mathbf{e}^j \quad (\text{C.24})$$

$$+ \frac{1}{2} \phi_{,b} \mathbf{e}^i \wedge (\omega_c) {}^b{}_a \mathbf{e}^c + \frac{1}{2} \phi_{,a} \omega_\gamma{}^i{}_j \wedge \mathbf{e}^j \quad (\text{C.25})$$

$$= \frac{1}{2} \nabla_a \nabla_b \phi \mathbf{e}^b \wedge \mathbf{e}^i + \frac{1}{4} \phi_{,a} \phi_{,b} \mathbf{e}^b \wedge \mathbf{e}^i \quad (\text{C.26})$$

$$= -\frac{1}{2} \left(\nabla_a \nabla_b \phi + \frac{1}{2} \phi_{,a} \phi_{,b} \right) \delta_{im} \mathbf{e}^m \wedge \mathbf{e}^b. \quad (\text{C.27})$$

The components of the Riemann tensor are already antisymmetric in m and b since $\nabla_m \phi = 0$.

The associated Ricci scalar is therefore

$$R_3 = \eta^{ab} R^i{}_{aib} = -d \left(\nabla^2 \phi + \frac{1}{2} (\nabla \phi)^2 \right). \quad (\text{C.28})$$

Not forgetting that $\sqrt{-G} = e^{d\phi/2} \sqrt{-g}$ for the total metric $G_{\mu\nu}$, the Einstein-Hilbert action S can be rewritten as

$$S = \int d^D x \sqrt{-G} (R_1 + R_2 + R_3) \quad (\text{C.29})$$

$$= \int d^D x \sqrt{-g} e^{d\phi/2} \left[R_g + d(d+1)e^{-\phi} - \frac{d(d-1)}{4} (\nabla \phi)^2 - d \left(\nabla^2 \phi + \frac{1}{2} (\nabla \phi)^2 \right) \right] \quad (\text{C.30})$$

$$= \int d^D x \sqrt{-g} e^{d\phi/2} \left[R_g + d(d+1)e^{-\phi} + \frac{d(d-1)}{4} (\nabla \phi)^2 \right], \quad (\text{C.31})$$

where we have used integration by parts in the last step.

With the dependence on d now explicit, the Einstein equations can be obtained straightforwardly by varying (C.31) with respect to both the metric and ϕ . In the presence of an Abelian gauge field A , the dimensionally-

reduced action instead reads [152]

$$S = \int d^D x \sqrt{-g} e^{d\phi/2} \left[R_g + d(d+1)e^{-\phi} + \frac{d(d-1)}{4}(\nabla\phi)^2 - \frac{1}{4}F^2 \right] \quad (\text{C.32})$$

with $F = dA$, and the Maxwell equations can be obtained in the usual way by varying the above with respect to A .